Department of Precision and Microsystems Engineering

Piezoelectric property characterization of GaN/AlN stacks by SAW devices

Yuxuan Liu

Report no : 2024.087
Coach : Tomás Manzaneque & Karen Dowling & Richard Norte
Professor : Tomás Manzaneque & Karen Dowling & Richard Norte & Sabina Canava
Specialisation : Dynamics of Micro and Nanosystems
Type of report : MSc Thesis

Acknowledgements

This thesis project holds great significance for me. I have learned a lot from this experience, which is interesting and meaningful. I would like to express my gratitude to many people who have accompanied me along the way.

First and foremost, I extend my sincerest thanks to my supervisors Tomas, Karen, and Richard. I am deeply grateful to Tomas and Karen for their guidance throughout the project and for all the assistance they provided to ensure my experiments ran smoothly. Your expertise has been invaluable, and your patience and kindness have touched me. Overall, I have had a very enjoyable year at EI with you. I am also thankful to Richard for being my supervisor at PME and for taking the time to help me with various tasks amidst your busy schedule. A special thanks to Sabina for taking the time to be part of my thesis committee.

I would like to express my heartfelt appreciation to Xiaoxi for the assistance provided in the cleanroom, as well as to my colleagues Jannik, Xinyi, Maodong, Lex, Qiuxuan, Jacopo, Yongqing, Zhengwei, and Sifeng for their support throughout the project. I am very happy to meet you all in Delft, and I wish you all the best in the future.

I am immensely grateful to Juan for helping me with the VNA and Probe station and to Ron and the other technicians at EI for their support. I would also like to thank Charles, Lodi, Eugene, Bas, and other technicians in Kavli nanolab for their assistance. I really enjoy the working environment at Kavli; it has been a wonderful adventure for me.

I would like to thank my girlfriend, Kanako, for her companionship over the past year, and I also want to express my gratitude to my friends Peiyu, Xinyi, Zeyao, and Ao for their encouragement and support during my thesis process.

Lastly, and most importantly, I want to thank my family for their unconditional support. All my wonderful memories in the Netherlands come from your love.

Delft, October 2024

Abstract

The performance and reliability of electronic devices in the harsh space environment are major concerns, particularly due to exposure to cosmic radiation and extreme temperatures. Wide bandgap semiconductors, such as gallium nitride (GaN) and silicon carbide (SiC), have emerged as promising materials for such environments due to their superior thermal stability and radiation resistance. An integrated chip combining MEMS sensors and GaN electronic components holds strong potential for space applications. This project aims to characterize the piezoelectric properties of a commercial GaN substrate using a surface acoustic wave (SAW) device while exploring its potential in MEMS sensor technology. The SAW devices, with varying operating wavelengths and surface conditions, were fabricated using processes including sputtering deposition, photolithography, and metal lift-off techniques. Wave velocity measurements were performed using a vector network analyzer, and the electromechanical coupling coefficients (k^2) were calculated. A comparison between the experimental results and simulations revealed that the piezoelectric performance of the GaN substrate was suboptimal. An analysis of the experimental error sources was conducted, and an optimization plan for the project was proposed.

Contents

1 Introduction

1.1. Motivation and Objective

Since the first artificial satellite was launched in 1957 [1], people started exploring space. This period has seen the utilization of advanced technologies in space projects. The harsh space environment, such as cosmic radiation and extreme temperature often impact the performance of the electric devices used in space exploration [2] [3] [4]. Common effects are ionization, displacement damage, and single-event effect(SEE)[5].

To reduce damage to instruments in the space environment, radiation shields are widely used in spacecraft devices. Aluminum is the more usual material in shields. In or to protect mostly sensitive components from radiation, increasing the Al shield thickness or adding some high-Z (high atomic number) material such as tantalum, tungsten, and lead are two main useful approaches. This will undoubtedly increase the size and mass of the whole instrument. If the thickness of the shield is increased, the interaction between radiation and shield material will generate more multiple secondary particles[6][5]. Electronics made from new materials less susceptible to damage from the harsh space environment offer new ideas for miniaturization. Wide band gap semiconductors such as GaN, SiC, etc attract significant attention. Due to their excellent properties, such as high-temperature stability, radiation resistance, and corrosion resistance, SiC and GaN both are ideal materials for harsh environments[7].

GaN is not only a wide band gap semiconductor but also a piezoelectric material[8]. Compared with other materials, GaN also possesses superior mechanical properties[8]. Leveraging these advantages, GaN can be used for making microelectromechanical systems (MEMS) devices[9]. Integrating GaN MEMS devices and GaN electronics on a single chip not only enriches the functionality of the chip but also reduces cost. If this kind of multifunctional chip is used in spacecraft, lighter and smaller spacecraft will be able to achieve. Additionally, this sensor system can be applied in fields such as agriculture, industrial factories, drilling, ocean exploration, and others.

To achieve spacecraft miniaturization and enhance electronic instrument performance in harsh environments, the development of GaN chips incorporating integrated MEMS devices and circuits is highly advantageous. Some advanced validation studies are necessary to avoid risk. So this project will mainly verify that GaN/AlN stacks have sufficient piezoelectric properties to develop MEMS devices. This project will characterize the piezoelectric properties of different GaN/AlN on Si stacks by surface acoustic wave (SAW) devices. Coupling coefficients(K^2) of SAW devices can be used as a reliable basis for characterization. Compared to conventional piezoelectric coefficient measurement methods, utilizing SAW devices is not only easy to fabricate but also protects the crystal structure from being damaged. Based on the research results, optimization methods and the possibility of making SAW sensors are discussed.

1.2. Thesis Overview

This report is structured as follows.

- Chapter 2 overviews the general background of SAW devices and fundamental theory. Additionally, it reviews the state of arts of GaN SAW, GaN sensor, and piezoelectric coefficients measurement method.
- Chapter 3 summarize the simulation results of SAW devices on different substrates.
- Chapter 4 present the detailed fabrication process and device parameters.
- Chapter 5 explain the data processing methods. Additionally, it presents and compares the measurement results, and conclusion are drawn.
- Chapter 6 analyzes the problem present in the experimental results, identifies the sources of error, and proposes optimization solutions of the project.

2

Background and State of Art

2.1. Background

2.1.1. Overview of AlN and GaN

Piezoelectric effect

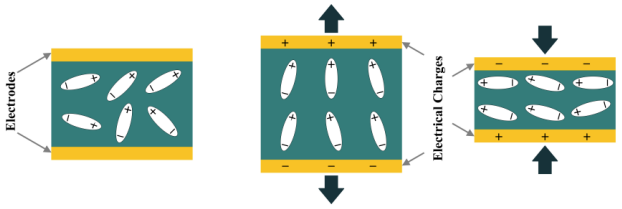

(a) direct piezoelectric effect

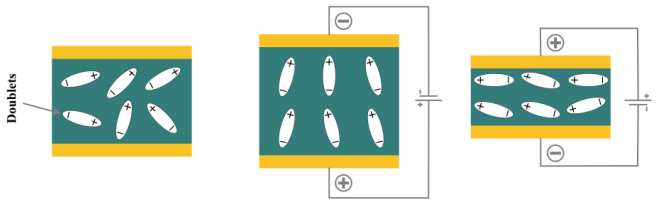

(b) converse piezoelectric effect

Figure 2.1: Piezoelectric Effect; (a) Direct Piezoelectric Effect; (b) Converse Piezoelectric Effect. [10]

The Piezoelectric effect can be categorized into two main types: the direct piezoelectric effect (as shown in Fig.2.1a) and the converse piezoelectric effect (as illustrated in Fig.2.1b). Piezoelectricity is always reciprocal, the direct and converse effect appears in all piezoelectric materials. Direct piezoelectric effect refers to certain materials that generate charge or voltage when pressure is applied. Common piezoelectric materials can be classified into three main categories: single crystal, piezoelectric ceramics, and piezoelectric polymers[11]. The piezoelectric properties of a crystal are significantly influenced by its no-central symmetry structure and material anisotropy, with the cutting orientation playing a pivotal role[12][13].

Generally, the piezoelectric coefficient is a crucial parameter for describing the piezoelectric property of material, which is denoted by d or e. Eq.2.1 and Eq.2.2 are strain-charge type piezoelectric equations, and Eq.2.3 and Eq.2.4 are stree-charge type piezoelectric equations. M. S. SHUR has more comprehensively organized the piezoelectric parameters of GaN and AlN[14], which is shown

in Fig.2.2.However, because of different measurement methods, the difference in measurements is relatively large. For this project, there is little literature about the piezoelectric parameters of GaN/AlN stacks.

e_{lm} (C/m^2)	e_{33}	e_{31}	e_{15}	e_{14}
GaN (electromechanical coefficients)	1	-0.36	-0.3	
GaN (mobility)	0.44	-0.22	-0.22	0.375
GaN (from optical phonons)	0.65	-0.33	-0.33	0.56
GaN (ab initio)	0.73	-0.49		
InN (from optical phonons)	0.43	-0.22	-0.22	0.37
InN (ab initio)	0.97	-0.57		
AlN (surface acoustic waves)	1.55	-0.58	-0.48	
AlN (ab initio)	1.46	-0.60		
SiC	0.2		0.08	
ZnO	1.32	-0.57	-0.48	
GaAs	-0.185	0.093	0.093	-0.16

Figure 2.2: Piezoelectric constants[14]

$$D = d \cdot T + \varepsilon_T \cdot E \tag{2.1}$$

$$S = s_E \cdot T + d^t \cdot E \tag{2.2}$$

$$D = e \cdot S + \varepsilon_S \cdot E \tag{2.3}$$

$$T = c_E \cdot S - e^t \cdot E \tag{2.4}$$

- D: electric displacement vector.
- T: stress vector.
- E: electric field vector.
- d or e: piezoelectric coupling matrix.
- ε_T or ε_S: dielectric constant matrix under constant stress or strain.
- s_E: compliance matrix under constant electric field.
- c_E: stiffness matrix under constant electric field.
- d^t: transpose of the piezoelectric coefficient matrix.

Crystal Structure

Aluminium (Al) and Gallium (Ga) both belong to the same main group (elements of the third group). That means they have similar electron arrangements; each has 3 outermost electrons, Fig.2.3 shows a detailed electron arrangement outside the nucleus. Because of the similar electron arrangement, AlN and GaN, also share the same crystal structure, called hexagonal wurtzite crystal structure. The hexagonal wurtzite crystal structure is shown in Fig.2.4. In this structure, applying force in the C-axis direction, the angle of the N-Al-N (N-Ga-N) bonds changes more easily compared to the Al-N (Ga-N) bonds. The internal charge is then displaced. This explains the intrinsic cause of the piezoelectric effect [15][16]. More detailed data on the structure can be obtained from AF.Wright's paper[17]. Eq.2.1 and Eq.2.2 can be written in the following matrix form in Eq.2.5 and Eq.2.6. The index numbers 1, 2, 3 respectively refer to the x, y, and z directions, while numbers 4, 5, and 6 refer to shear around x, y, and

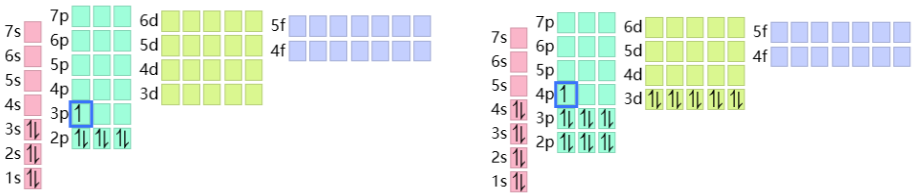

(a) AlN **(b)** GaN

Figure 2.3: arrangement of extranuclear electrons (a) AlN (b) GaN[18]

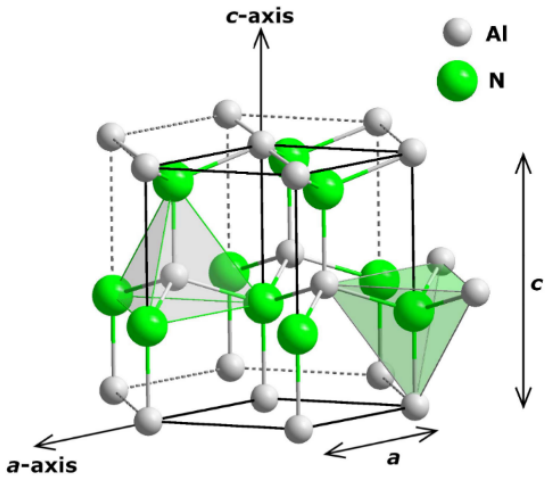

Figure 2.4: Hexagonal wurtzite crystal structure of AlN[19]

z. It's worth noting that AlN and GaN have the same form of the piezoelectric coefficient matrix, which is important to facilitate modeling stacks of layers with both materials.

$$\begin{bmatrix} D_1 \\ D_2 \\ D_3 \end{bmatrix} = \begin{bmatrix} 0 & 0 & 0 & 0 & d_{15} & 0 \\ 0 & 0 & 0 & d_{15} & 0 & 0 \\ d_{31} & d_{31} & d_{33} & 0 & 0 & 0 \end{bmatrix} \begin{bmatrix} T_1 \\ T_2 \\ T_3 \\ T_4 \\ T_5 \\ T_6 \end{bmatrix} + \begin{bmatrix} \varepsilon_{11} & 0 & 0 \\ 0 & \varepsilon_{11} & 0 \\ 0 & 0 & \varepsilon_{11} \end{bmatrix} \begin{bmatrix} E_1 \\ E_2 \\ E_3 \end{bmatrix} \tag{2.5}$$

$$\begin{bmatrix} S_1 \\ S_2 \\ S_3 \\ S_4 \\ S_5 \\ S_6 \end{bmatrix} = \begin{bmatrix} S_{11} & S_{12} & S_{13} & 0 & 0 & 0 \\ S_{21} & S_{22} & S_{23} & 0 & 0 & 0 \\ S_{31} & S_{32} & S_{33} & 0 & 0 & 0 \\ 0 & 0 & 0 & S_{44} & 0 & 0 \\ 0 & 0 & 0 & 0 & S_{55} & 0 \\ 0 & 0 & 0 & 0 & 0 & S_{66} \end{bmatrix} \begin{bmatrix} T_1 \\ T_2 \\ T_3 \\ T_4 \\ T_5 \\ T_6 \end{bmatrix} + \begin{bmatrix} 0 & 0 & d_{31} \\ 0 & 0 & d_{31} \\ 0 & 0 & d_{33} \\ 0 & d_{15} & 0 \\ d_{15} & 0 & 0 \\ 0 & 0 & 0 \end{bmatrix} \begin{bmatrix} E_1 \\ E_2 \\ E_3 \end{bmatrix} \tag{2.6}$$

High Band-Gap Semiconductors

GaN is a high-band gap semiconductor. The bands of a crystal can be divided into the valence band and conduction band shown in Fig.2.5. The valence band is the highest band fully occupied by electrons at $0K$. In the conduction band which is situated above the valence band, electrons can be excited by energy resulting in the jump from the valance band to the conduction band, which makes the crystal conductive. The energy gap between the valence band and conduction band is called band gap[20]. The band gap of GaN is $3.4eV$ which is higher than Si ($1.1eV$)[21]. That means the electrons in the valence band of GaN need more energy (higher temperature) to jump to the conduction band. That

is why GaN keeps semiconductor properties in harsh environments such as space. The bandgap for more materials is summarized in Tab.2.1.

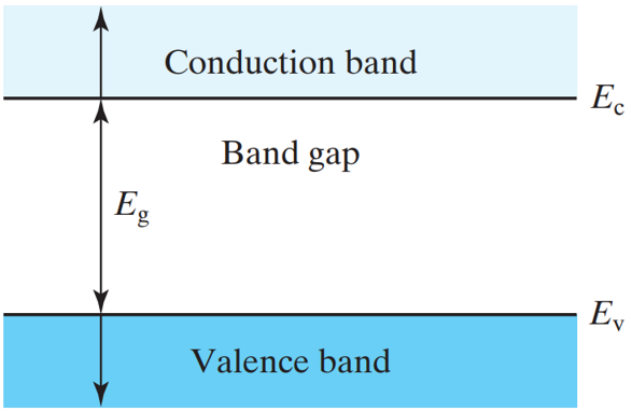

Figure 2.5: Energy band

Table 2.1: Bandgap of various materials(S is sphalerite structure and W is wurtzite structure)[22].

Material	Si	C(diamond)	$GaN(w)$	$GaP(S)$	$GaAs(S)$	$AlN(W)$	$ZnO(S)$
Bandgap(ev)	1.12	5.48	3.44	2.26	1.43	6.2	3.3

Mechanical Properties

The mechanical properties of GaN are well-suited for MEMS devices. GaN exhibits a higher Young's modulus than Si, which has a modulus of approximately $160GPa$.[23]. In the case of GaN on AlN/-GaN/AlN/Si structure, the hardness is $22.5GPa$ and the Young's modulus is around $270GPa$ [8] Higher Young's modulus provides reliability and stability to MEMS structures, which makes the microdevices less prone to deformation under the influence of external disturbance force. High Young's modulus material typically exhibits a low thermal expansion coefficient, which gives GaN good thermal-mechanical stability.

2.1.2. SAW Devices

Working Principle

Surface acoustic wave (SAW) devices utilize the acoustic wave on the surface of the solid for processing signals. Here we focus the Rayleigh wave generated on the AlN/GaN surface. The polarization direction of the Rayleigh wave is normal to the plane of the substrate surface. It comprises a superposition of longitudinal(P) and shear vertical (SV) waves, the amplitude of the Rayleigh wave decreases exponentially along the depth[24]. The waveform is shown in Fig.2.6. The interdigital transducer (IDT) is the most critical component of the SAW devices. The IDT consists of two comb-shaped electrode arrays, one of them is grounded and the other is connected to the input terminal or output terminal. The electric field can be generated on the surface of the piezoelectric substrate by applying an input voltage signal on the IDT. This results in strain and stress within the material due to the converse piezoelectric effect. At a specific frequency, the acoustic wave will be generated. On the contrary, IDTs can also transform the acoustic wave signal into an electric output signal via the direct piezoelectric effect. By varying design parameters such as electrode width, finger number, and spacing, SAW devices can be tuned to different working frequencies, bandwidths, and insertion loss[24].

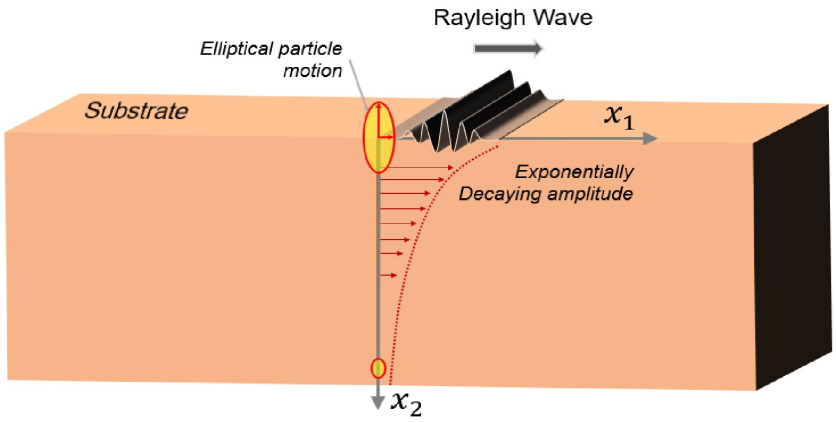

Figure 2.6: The Rayleigh waves propagating along a surface[24]

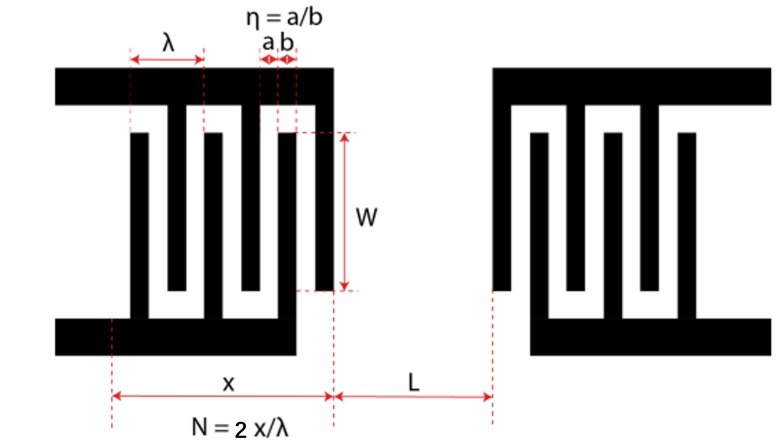

Figure 2.7: SAW delay line IDTs schematic diagram

SAW Delay Line Device Design

A schematic diagram of the SAW IDTs is shown in Fig.2.7. SAW delay line devices are widely used in radar, wireless, and signal processing. The relation between the acoustic velocity v, operating wavelength λ, and working frequency f is shown in Eq.2.7. The operating wavelength λ is twice the electrode period length$b$.

$$v = \lambda \times f \tag{2.7}$$

The metallization ratio is the ratio of the electrode width a to the period length b. The ratio should be 0.5, meaning the electrode width should equal the spacing. This design can reduce the generation of high harmonics wave and the reflection[25].

The number of electrode pairs N is relative to the SAW signal amplitude and the response bandwidth. N is inversely proportional to bandwidth[26]. A higher N device also generates more SAW signals. For this project, the larger the value of N, the greater the interference generated by the IDTs during the surface wave propagation, which is unfavorable for reducing the calculation error of the wave velocity. The selection will be determined through simulations and experimentation.

To gain more signal from the output terminal, the transducer aperture W is usually 50-100 times the wavelength[27]. By calculating the mathematical model, the frequency response of an ideal IDT is given by Eq.2.8 . The response is shown in Fig.2.8[28].

$$H(f) \approx N \left| \frac{sin(N_p\pi(f - f_0)/f_0)}{N_p\pi(f - f_0)/f_0)} \right| \tag{2.8}$$

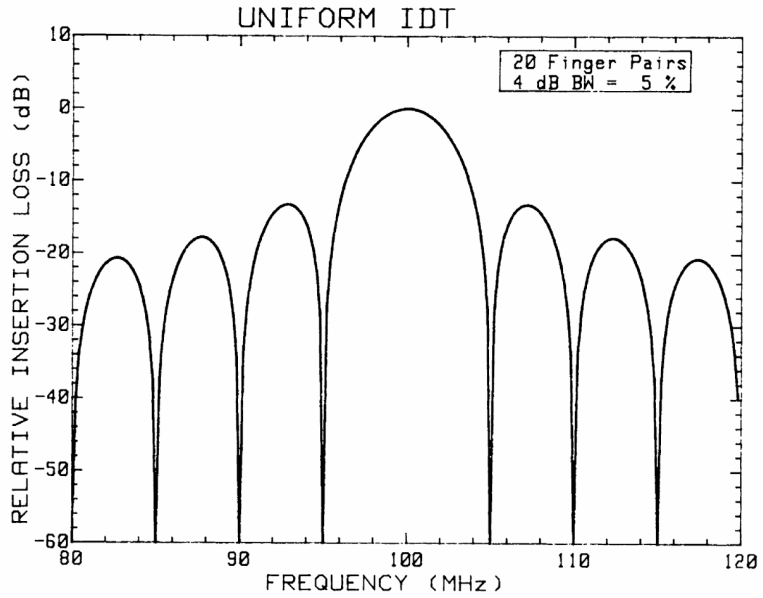

Figure 2.8: Calculated magnitude response of uniform IDTs [28]

Some second-order effects corrupt SAW device responses. The electromagnetic feedthrough is the direct coupling of input IDTs and output IDTs, the electromagnetic wave arrives at the output IDTs with light velocity to generate this coupling, and the interaction causes periodic ripples at ripple frequency $f_r = v/d$[28]. Another second-order effect is triple transit interference(TTI), the SAW power received by output IDTs is reflected to the input IDTs, then the reflected wave will lead to future regeneration of an SAW wave at input IDTs, these effect results ripple at $f_r = v/2d$. The metal film IDT fingers will also cause this reflection and induce a mass-loading effect [28]. Impedance matching is another important factor in obtaining a good response. Maximum signal transfer is obtained when the impedance of the SAW device is the same as the impedance of the signal measurement device.

The SAW delay line can be modeled as a two-port transmission network, as depicted in Fig.2.9. The input IDT serves as the input terminal, while the output IDT functions as the output terminal. An important parameter of two-port networks is the scattering parameter, which indicates the reflected and transmitted power of the network. The S-parameter matrix is shown in Eq.2.9. b_1 and b_2 represent the reflected waves at the two terminals, while a_1 and a_2 signify the incident waves. S_{11} and S_{22} refer to the reflection coefficient, S_{21} and S_{12} refer to the transmission coefficient. This project mainly focus on the S_{21} parameter of our device.

$$\begin{bmatrix} b_1 \\ b_2 \end{bmatrix} = \begin{bmatrix} S_{11} & S_{12} \\ S_{21} & S_{22} \end{bmatrix} \begin{bmatrix} a_1 \\ a_2 \end{bmatrix} \tag{2.9}$$

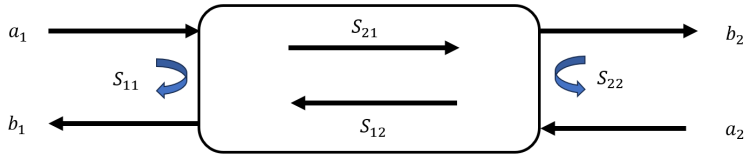

Figure 2.9: two-port network

(a) SAW delay line with free surface

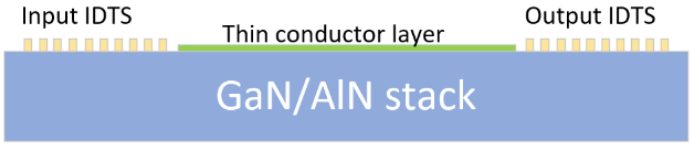

(b) SAW delay line with short-circuited surface

Figure 2.10: Two surface conditions for SAW delay line (a) free surface ; (b) short-circuit surface

The electromechanical coupling constant K^2 is another important parameter in this project. It is related to various constants of the substrate material[29]. This parameter can also characterize the piezoelectric effect of the material. Although the electromechanical coupling constant can be derived from the basic material mechanical parameters and electric parameters, it can be calculated by wave velocity in SAW devices to avoid complex calculations. In general, the K^2 can be calculated using Eq.2.10 [30]. V_f and V_m are the SAW velocities on the free and short-circuited surfaces which are shown in Fig.2.10a and Fig.2.10b. For more precision, another formula is detailed in Eq.2.10[29]. The terms $\varepsilon_{11}, \varepsilon_{33}, \varepsilon_{13}$ represent relative permittivity tensor. The K^2 of some devices made of different materials are summarized in Fig.2.11[31][32].

$$k^2 = 2\frac{V_f - V_m}{V_f} \tag{2.10}$$

$$k^2 = 2(1 + (\varepsilon_{11}\varepsilon_{33} - \varepsilon_{13}^2)^{-1/2})\frac{V_f - V_m}{V_f}. \tag{2.11}$$

	v_{T_1} (m/s)	v_{T_2} (m/s)	v_L (m/s)	v_R (m/s)	k^2_{eff} (in 10^{-3})
GaN	3826	4277	7757	3693	1.31
AlN	6095	6465	11267	5790	2.5
4H−SiC	7276	7882	12566	6832	0.112
sapphire				5703	
$LiNbO_3$				3488	23.2
GaAs				2867	0.593

Figure 2.11: Velocity of bulk($V_T and V_L$) and surface(V_R) acoustic waves and electromechanical coupling coefficients on c-oriented AlN GaN and SiC[32].

SAW propagation

The reason for the different wave speeds seen on the free and shortcircuit surfaces is explained in detail through theoretical derivations. Newton's second law shows that the divergence of the stress tensor is the product of the density and acceleration.

$$\nabla \cdot \mathbf{T} = \rho \frac{\partial^2 \mathbf{u}}{\partial t^2} \tag{2.12}$$

The **T** is the stress tensor, In linear elastic mechanics, due to its symmetry, the stress tensor in the form of a 3×3 matrix is often reduced to a 6×1 stress vector containing positive stresses in three directions and shear stresses in three directions. ρ is the density and u is the partical displacement vector. Under linear conditions, the strain is the gradient of the displacement.

$$\mathbf{S} = \nabla \mathbf{u} \tag{2.13}$$

the **S** is also a 6×1 vector, which contains three positive strains and three shear strains. The electric field**E** is a gradient in potentialϕ.

$$\mathbf{E} = -\nabla \phi \tag{2.14}$$

In SAW devices there are no free charges, so the gradient of electric displacement D should be zero.

$$\nabla \mathbf{D} = 0 \tag{2.15}$$

The above equations combined with the piezoelectric equations 2.3 and 2.4 can construct a system of equations for displacement and potential. The solution of the equation can be set in the form of a simple harmonic wave on a plane.

$$u_1 = A \cos(\alpha x_3) \sin(k x_1 - \omega t) \tag{2.16}$$

$$\phi = B \sin(\alpha x_3) \cos(k x_1 - \omega t) \tag{2.17}$$

here u_2 u_3 should be zero since SAW in delay line devices only propagate along one direction. A and B are the wave amplitude, α is the attenuation factor along z direction, k is wave number and ω is angle frequency. After calculation, eq.2.12 and eq.2.15 lead to three non-linear equations.

$$(c_{11}k^2 + c_{44}\alpha^2 - \rho\omega^2)A + (e_{31} + e15)\alpha k B = 0 \tag{2.18}$$

$$(c_{44} + c_{13})\alpha k A + (e_{15}k^2 + e_{33}\alpha^2)B = 0 \tag{2.19}$$

$$(e_{15} + e_{31})\alpha k A - (\epsilon_{11}k^2 + \epsilon_{33}\alpha^2)B = 0 \tag{2.20}$$

Clearly, solving this nonlinear system of equations is very difficult. For five unknowns, more boundary condition equations are needed to obtain a finite number of non-zero solutions. Ideally, the SAW transfer surface is stress-free so the boundary condition includes $T_{33} = T_{23} = T_{13} = 0$. On short-circuited

Substrate	K^2	Reference
GaN on 4H-SiC	0.131	[41]
GaN on Si	0.066	[42]
GaN on Sapphire	0.015	[43]
GaN on Sapphire	0.06-0.09	[44]
GaN on Sapphire	0.18-4.73	[45]
AlN on Sapphire	0.1-0.45	[43]
AlN on Si	0.01	[46]
AlN on 4H-SiC	0.015	[41]

Table 2.2: The coupling coefficients of different SAW devices

surfaces that are completely covered by a layer of conductor metal, the boundary condition can be $\phi = 0$. In practice, however, the boundary conditions are very complex, with inevitable stresses on the surface during epitaxial growth of the substrate and a mass-loading effect on the short-circuit surface of the deposited metal. Whether the short circuit surface is grounded or not also determines the magnitude of its potential. However, there is no doubt that the change in boundary conditions will largely determine the solution of the equation. Under different boundary conditions, the equations will be solved for different numbers of waves and angular frequencies that satisfy the conditions, and therefore different propagation speeds will be obtained.

2.2. State of Art

2.2.1. GaN Buffer

There are two main challenges for growing GaN on Si, one is avoiding the formation of Ga-Si alloy, and another is preventing the cracking and bowing of the wafer[33]. Using a buffer layer to grow GaN is the primary solution to address these issues.

The Ultra-thin AlN/GaN superlattice interlayer is a kind of buffer to grow crack-free high-quality GaN on Si substrate, which has the unique function of naturally generating microcracks (MCs) to compensate for the CTE-induced tensile strain. Consequently, the GaN epilayer can have good quality because of the influence of the ultra-thin AlN/GaN superlattice interlayer. By controlling the depth of the superlattice interlayer, the micro-crack size and GaN quality can be adjusted. The figures are shown in Fig.2.12a and Fig.2.12b [34].

Growing GaN epitaxial layer on Si substrate by introducing Step-Graded AlGaN intermediate layers to improve the crystal quality is another method. The composition of Al in the intermediate layer varies from $25 - 73\%$. These step-graded AlGaN layers improve the crystalline quality and decrease the surface crack density. By analyzing AlGaN buffer layers with different thicknesses, the best template shows $-0.01GPa$ mean stress and $119m$ radius of wafer bowing [35]. One single AlGaN layer can also be used to produce crack-free GaN epilayers, reducing fabrication costs and time. The compressive stress from growth and the tensile stress caused by cooling could be balanced by a single low Al component AlGaN buffer layer[35].

The schematic cross-sectional views of two different GaN buffer layers are shown in Fig.2.13[36].

2.2.2. GaN SAW Devices

GaN acoustic wave devices are used as resonators, sensors, filters, and other applications[37][38][39]. Two-dimensional electron gas (2DEG) has replaced metal electrodes for use in IDTs. The device and the comparison result are shown in Fig.2.14a and Fig.2.14b. They found that metal IDTs decreased the center frequency and reduced the SAW velocity due to mass loading. However, the 2DEG IDTS increased the insertion loss due to the ohmic loss[40].

Some GaN and AlN SAW devices' coupling coefficients are summarized in Tab.2.2.

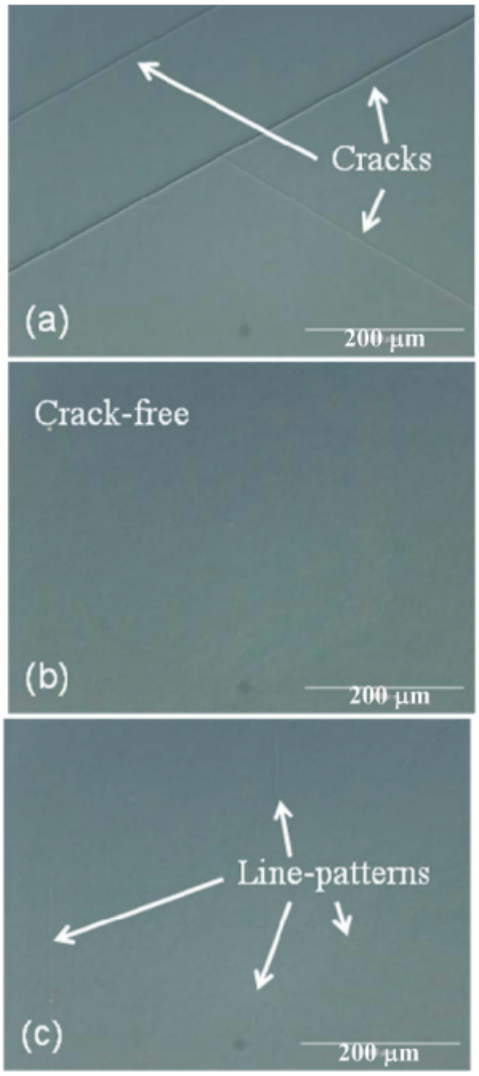

(a) GaN epilayers surface images measured by optical microscope. (a) 80 nm AlN/GaN layer (b) 160 nm AlN/GaN layer (c) 240 nm AlN/GaN layer

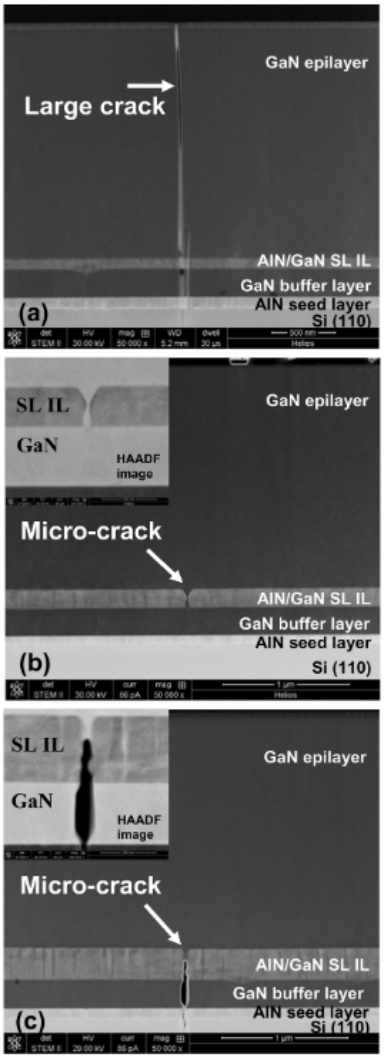

(b) Cross-sectional STEM images of three 2.0 µm thick GaN epilayers grown on Si(110) substrates with different AlN/GaN SL IL thicknesses (a) 80 nm AlN/GaN layer (b) 160 nm AlN/GaN layer (c) 240 nm AlN/GaN layer

Figure 2.12: The research results of Xu-Qiang Shen and his teammates [34]

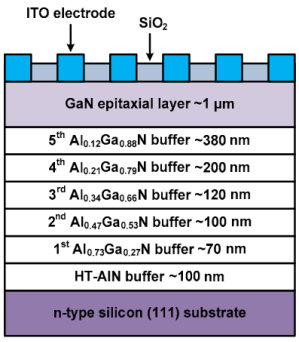

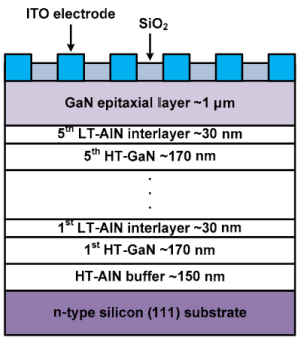

Figure 2.13: The schematic cross-sectional views of two different GaN MSM UV photodetectors (a) step-graded AlGaN buffer layer;(b) HT-GaN/LT-AlN buffer layer[36]

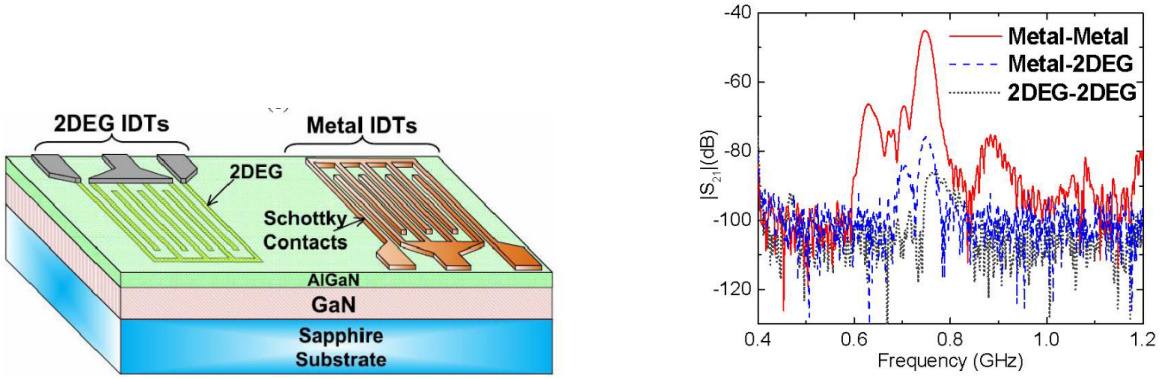

(a) 2DEG-metal IDTS SAW filter

(b) S parameters comparison result

Figure 2.14: King-Yuen Wong analysis on GaN SAW filters (a)2DEG-metal IDTS SAW filter device;(b)S parameters comparison result [40]

2.2.3. Piezoelectric Coefficient Measurement

The most common direct measurement method is the normal load method. This method is based on the piezoelectric response of the sample with top and bottom electrodes. For more accurate results, the periodic compressional force method and cantilever method are used[47]. Another approach is to combine the load measurement method with FEM simulation to fit the piezoelectric coefficient.[48]. A mini force Hammer is used to measure the d_{33} of zirconate titanate thin films employing the same normal load method, this method is low-cost and more accurate without damaging the films[49]. The device is shown in Fig.2.15. Measuring the piezoelectric coefficient using an optical interferometer is also common. High sensitivity interferometer can measure the tiny piezoelectric displacement of samples, thereby yielding more accurate results. Fig.2.16[50] shows a comprehensive system to measure the d_{31} and d_{33} of piezoelectric ceramic. The research using X-ray diffraction techniques to measure $BaTiO_3$ thin film underscores the potential of using laboratory diffraction techniques not only to determine the effective piezoelectric coefficients in thin films but also to ascertain their Curie temperatures.[51]. However, all of these measurement methods require bottom and top electrodes to drive the piezoelectric material, and for GaN stacks containing a buffer layer, it is more difficult to fabricate the electrodes under the buffer layer, while the introduced stresses can also damage the crystal structure of the GaN.

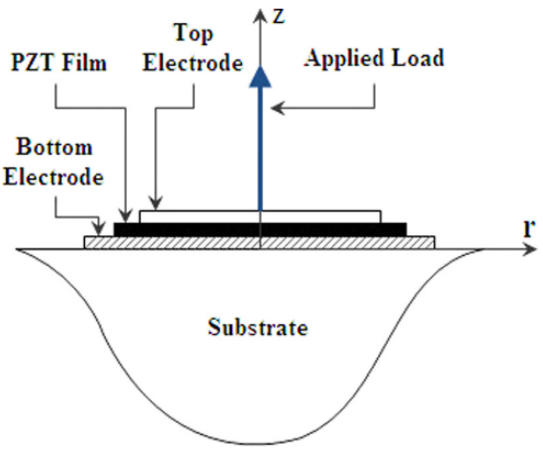

Figure 2.15: Measurements of Piezoelectric Coefficient d33 of Lead Zirconate Titanate Thin Films Using a Mini Force Hammer [49]

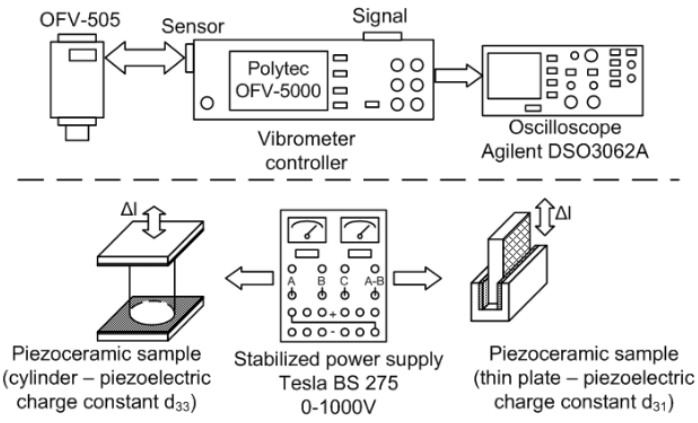

Figure 2.16: Polytee laser interferometer measurement system [50]

3

SAW devices Simulation

This chapter presents both eigenfrequency and frequency domain simulations. The simulations for this project were conducted using the finite element analysis software, COMSOL. Since GaN piezoelectric parameters are not available in the COMSOL library, the parameters used in this simulation were sourced from external references. The GaN piezoelectric parameters are detailed in Tab.3.1, Tab.3.2 and Tab.3.3[52][53].

C_{11}	C_{12}	C_{13}	C_{33}	C_{44}	C_{66}
359.4	129.2	92	389.9	98	$0.5(C_{11}-C_{12})$

Table 3.1: GaN Elasticity Matrix Parameters (Gpa)

e_{33}	e_{31}	e_{15}
1	-0.36	-0.3

Table 3.2: GaN Coupling Matrix (C/m^2)

ε_{11}	ε_{22}	ε_{33}
5.35	5.35	5.8

Table 3.3: GaN Relative permittivity

3.1. Eigenfrequency Simulation

This section mainly covers the simulation of AlN on silicon, GaN on silicon, and GaN stacks with two different buffer layers (Superlattice and Gradient). Eigenfrequency simulations are conducted to optimize the dimensions of the SAW devices for achieving the best coupling coefficients (K^2). The devices with different operating wavelengths will be simulated. For different operating wavelengths, both free surface and short circuit surface devices will be analyzed. Then the phase velocity will be calculated by Eq.2.7. The coupling coefficients will be calculated by Eq.2.10.

3.1.1. AlN and GaN on Silicon

The model shown in Fig.3.1 is part of a SAW device with a length of one wavelength, the corresponding parameters are listed in Tab.3.4. A perfectly matched layer (PML) is incorporated to simulate a non-reflecting domain. Both sides of the model are set as periodic boundaries in the mechanical and electrostatic domains to simulate the behavior of SAW in the IDTs. The electrode width is variable and adjusts to a quarter of the wavelength. During the simulation, the wavelength is varied between 8 μm

and 20 μm, consistent with the superlattice and gradient buffer simulations performed later. This simulation provides valuable insights for comparing the piezoelectric properties of different buffer layers.

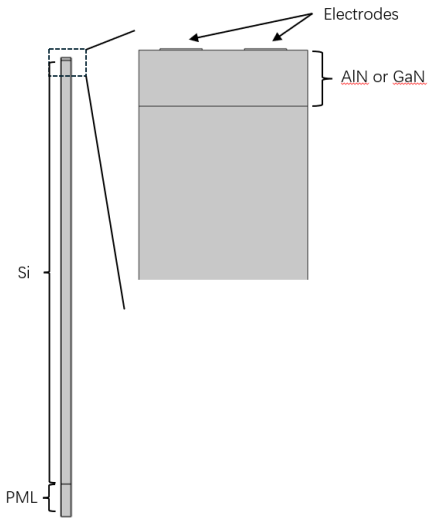

Figure 3.1: A section of AlN(GaN) on silicon model for eigenfrequency simulation

Layer Name	PML	Si	AlN (GaN)	electrodes thickness
Thickness	400 μm	625 μm	4 μm	100 nm

Table 3.4: The AlN(GaN) on silicon model each layer thickness

The following Fig.3.2a illustrates the surface acoustic wave modes and eigenfrequency of AlN on silicon at a 12 μm wavelength for both free and short-circuit surfaces. The coupling coefficient in this case is $K^2 = 0.632\%$. The following Fig.3.2b shows the surface acoustic wave modes and eigenfrequency of GaN on Silicon at 12μm wavelength for free surface and short circuit surface, respectively. The coupling coefficient in this case is $K^2 = 0.18\%$ Since the simulation focuses solely on this eigenmode, the eigenfrequencies and coupling coefficients for other operating wavelengths are summarized in Tab.3.5 and Tab.3.6.

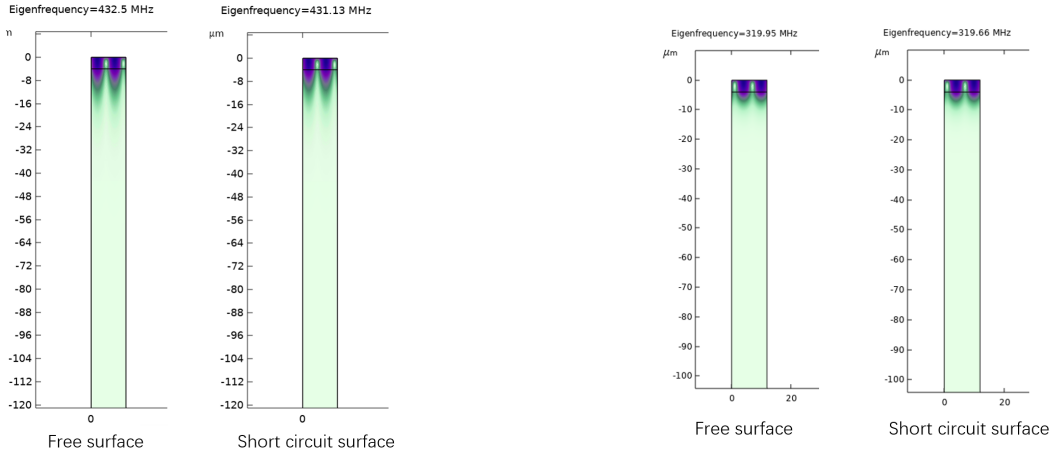

(a) AlN on silicon

(b) GaN on silicon

Figure 3.2: AlN (GaN) on silicon eigenfrequency simulation at 12μm working frequency

wavelength (μm)	eigenfrequency (MHz)		Vf (m/s)	Vm (m/s)	k^2 (%)
	freesuface	short circuit			
8.5	630.53	628.63	5359.54	5343.35	0.60
9	592.67	590.72	5334.03	5316.47	0.66
10	528.20	526.41	5282.03	5264.09	0.68
11	475.73	474.15	5233.00	5215.66	0.66
12	432.50	431.13	5189.94	5173.55	0.63
13	396.22	395.05	5150.91	5135.62	0.59
14	365.58	364.57	5118.18	5103.97	0.56
15	339.29	338.41	5089.31	5076.12	0.52
16	316.53	315.76	5064.54	5052.21	0.49
17	296.69	296.01	5043.66	5032.11	0.46
18	279.20	278.60	5025.52	5014.71	0.43

Table 3.5: The simulation results of AlN on silicon with different working wavelengths

Fig.3.3 shows the results graphically. The simulation demonstrates that the coupling coefficient of AlN on Si is larger, indicating better piezoelectric performance compared to GaN. As the wavelength changes, the coupling coefficients of both materials exhibit a similar trend. This occurs because the electric field generated by the IDT at different wavelength settings penetrates to varying depths within the piezoelectric materials. At smaller wavelengths, the electric field primarily affects the surface layer, failing to fully utilize the piezoelectric material, which results in a lower coupling coefficient. As the wavelength increases, the electric field reaches the non-piezoelectric silicon layer beneath, causing a decrease in the coupling coefficient.

wavelength (μm)	eigenfrequency (MHz)		Vf (m/s)	Vm (m/s)	k^2 (%)
	freesuface	short circuit			
4	963.62	962.49	3854.50	3849.97	0.23
5	769.47	768.52	3847.34	3842.60	0.25
6	639.92	639.11	3839.50	3834.66	0.25
7	547.80	547.11	3834.58	3829.78	0.25
8	478.89	478.31	3831.13	3826.50	0.24
9	425.55	425.07	3829.97	3825.60	0.23
10	383.10	382.69	3830.98	3826.92	0.21
11	348.53	348.18	3833.78	3830.02	0.20
12	319.95	319.66	3839.39	3835.93	0.18
13	295.87	295.63	3846.34	3843.16	0.17
14	275.44	275.23	3856.11	3853.19	0.15
15	257.81	257.63	3867.09	3864.41	0.14
16	242.47	242.32	3879.58	3877.08	0.13
17	229.03	228.89	3893.52	3891.18	0.12
18	217.12	217.00	3908.17	3905.97	0.11

Table 3.6: The simulation results of GaN on silicon with different working wavelengths

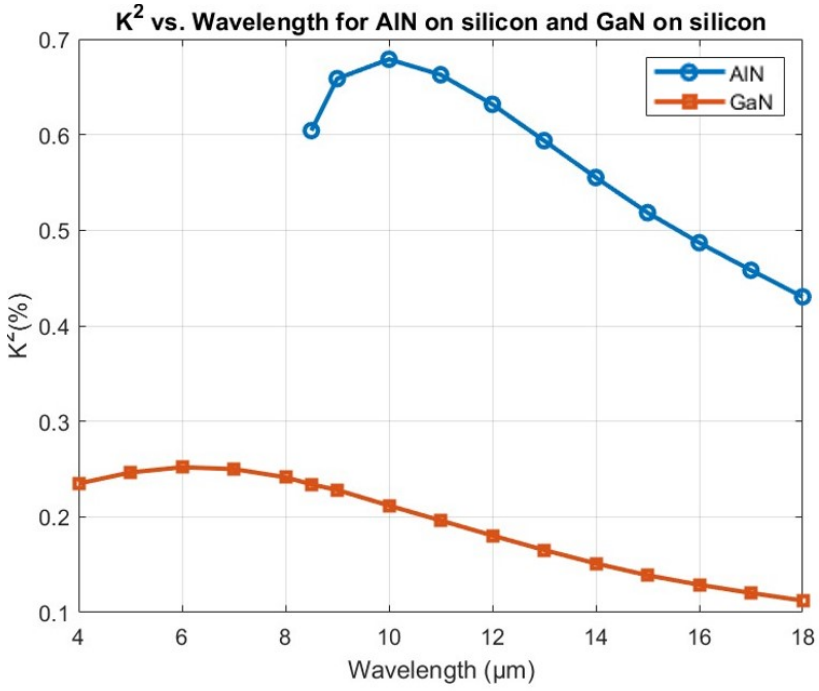

Figure 3.3: The simulation results of AlN(GaN) on silicon with different working wavelengths

Layer Name	Si	AlN in SL buffer	GaN in SL buffer	GaN cap layer
Thickness	625 μm	16 nm	80 nm	1.5 μm

Table 3.7: The GaN superlattice(SL) buffer stack model each layer thickness

wavelength (μm)	**eigenfrequency (MHz)**		**Vf (m/s)**	**Vm (m/s)**	**k^2 (%)**
	freesuface	**short circuit**			
4	984.38	983.34	3937.53	3933.36	0.21
5	787.95	787.07	3939.74	3935.35	0.22
6	656.18	655.42	3937.06	3932.53	0.23
7	561.84	561.19	3932.86	3928.33	0.23
8	491.13	490.58	3929.06	3924.68	0.22
9	436.30	435.84	3926.69	3922.55	0.21
10	392.63	392.25	3926.33	3922.48	0.20
11	357.10	356.78	3928.08	3924.54	0.18
12	327.67	327.40	3932.07	3928.83	0.17
13	302.94	302.71	3938.18	3935.21	0.15
14	281.88	281.68	3946.30	3943.57	0.14
16	247.96	247.81	3967.30	3964.98	0.12
18	221.84	221.72	3993.03	3991.00	0.10
20	201.15	201.06	4023.00	4021.17	0.09

Table 3.8: The simulation results of GaN SL buffer stack with different working wavelengths

3.1.2. GaN superlattice buffer and gradient buffer

The section of GaN superlattice(SL) buffer model is shown in Fig.3.4. Since the silicon layer and PML are identical to those in the AlN and GaN on silicon models, Fig.3.4 does not include these components. The superlattice layer should have 25 pairs and the AlN should have 16% to avoid surface stress[54]. The detailed parameters are shown in Tab.3.7. The wavelength is varied between 8 μm and 20 μm during the simulation. The modes excited by this substrate are the same as those in Fig.3.2a Fig.3.2b, with differences only in the frequencies. The results of the simulation are concluded in Tab.3.8.

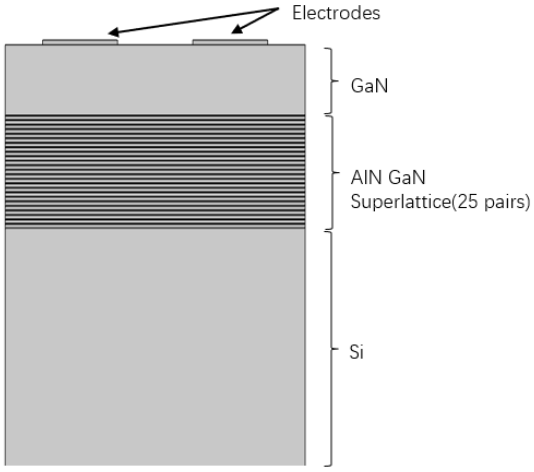

Figure 3.4: The section of GaN superlattice(SL) buffer stack model for eigenfrequency simulation

The section of GaN gradient buffer stack 2D model is shown in Fig.3.5. The buffer structure was provided by Atecon Technology Co., Ltd., and the detailed parameters are listed in Tab.3.9. The simulation results are shown in Tab.3.10.

Both super lattice and gradient buffer simulation results are shown graphically in Fig.3.6. The simu-

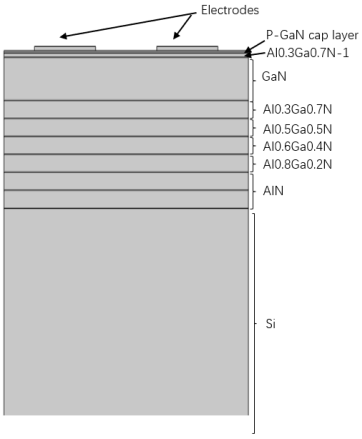

Figure 3.5: The section of GaN gradient buffer stack model for Eigenfrequency simulation

Layer Name	Si	AlN	AlGaN(0.8-0.3)	GaN	Al0.3GaN-1	p-GaN cap
Thickness	960 μm	0.83 μm	0.42μm	1 μm	100nm	50nm

Table 3.9: The GaN gradient buffer stack model each layer thickness

lation results show that the coupling coefficient of gradient buffer is larger and the piezoelectric performance is better than super lattice buffer, this is because in this stack, AlN in the buffer plays a significant role in the transduction. Since AlN, has higher piezo coefficients than GaN, the electromechanical coupling is higher. Simulation results show that for gradient buffer, 13μm wavelength SAW can excite the best piezoelectric performance of the substrate, and for super lattice buffer, 6um wavelength can excite the best piezoelectric performance. As with the previous simulation, the depth of electric field action changes as the wavelength changes, resulting in the coupling coefficient increasing and then decreasing.

Comparing Fig.3.3 and Fig.3.6, The GaN stacked piezoelectric performance with a gradient buffer layer($K^2 = 0.21 - 0.46$%) is better than super lattice buffer GaN ($K^2 = 0.09 - 0.23$%). At the operating wavelength of 13 μm, the coupling coefficient of the GaN gradient stack is 0.458%, which is the maximum. For AlN on Si SAW devices, the 10μm operating wavelength exhibits the largest piezoelectric coupling coefficient of 0.68% being 0.222% larger than the GaN gradient buffer maximum, and the coupling coefficient for devices with 13μm operating wavelength is 0.59% being 0.132% larger than the GaN gradient buffer maximum. However, the coupling coefficient of the AlN device with greater than 17μm operating wavelength is smaller than that of the GaN gradient buffer SAW devices. This is enough to prove that gradient GaN has a strong piezoelectric MEMS potential.

wavelength (μm)	eigenfrequency (MHz)		Vf (m/s)	Vm (m/s)	k^2 (%)
	freesuface	short circuit			
6	728.01	727.23	4368.03	4363.41	0.21
7	626.20	625.37	4383.43	4377.58	0.27
8	548.11	547.23	4384.91	4377.84	0.32
9	486.63	485.73	4379.68	4371.54	0.37
10	437.20	436.31	4372.02	4363.07	0.41
11	396.76	395.90	4364.38	4354.86	0.44
12	363.17	362.35	4358.05	4348.20	0.45
13	334.90	334.13	4353.66	4343.68	0.46
14	310.82	310.11	4351.43	4341.49	0.46
15	290.09	289.44	4351.36	4341.59	0.45
16	272.08	271.49	4353.33	4343.81	0.44
18	242.36	241.87	4362.49	4353.67	0.40
20	218.86	218.46	4377.16	4369.14	0.37

Table 3.10: The simulation results of GaN gradient buffer stack with different working wavelengths

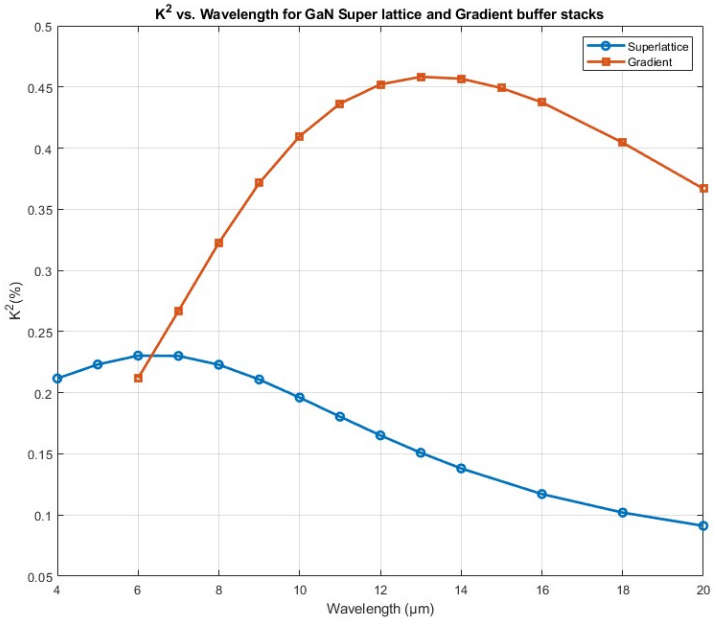

Figure 3.6: The simulation results of GaN SL and gradient buffer stacks with different working wavelengths

3.2. Reflection Simulation

Due to the triple transit interference(TTI), the output IDTs will receive the superimposed signal of the incident and reflected waves. This reflected wave will cause fluctuations and distortion in the frequency response. We used a 100Hz sinusoidal pulse signal to simulate the input SAW signal, and the same signal with amplitude attenuation to simulate the reflected SAW signal. There is a time delay between these two signals. Their frequency response is compared after using Fourier transforms. The simulation results are shown in Fig.3.7. Compare Fig.3.7b and Fig.3.7b, the more severe the reflection, the greater the distortion in the frequency response. Additionally, if the primary signal is weaker, the main peak in the frequency response is more susceptible to disturbance. Compare Fig.3.7b and Fig.3.7b, the ripple frequency is related to the delay time. These simulations were done in Matlab and they will provide a reference for Chapter 5 to distinguish the reflected signals.

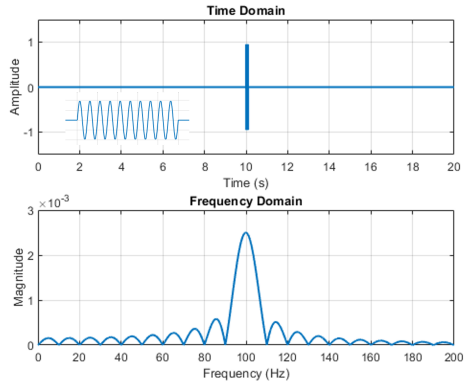

(a) No reflection

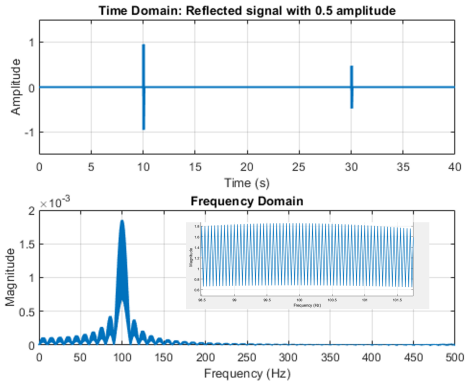

(b) Reflection signal with 0.5 amplitude and 20s delay

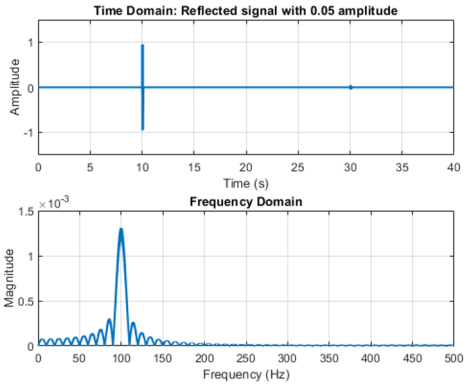

(c) Reflection signal with 0.05 amplitude and 20s delay

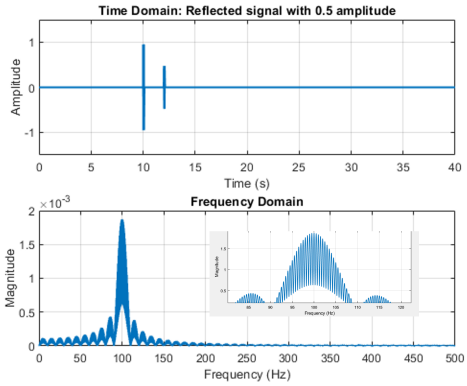

(d) Reflection signal with 0.5 amplitude and 2s delay

Figure 3.7: The time-domain and frequency-domain responses of different reflected signals

IDT pairs	S11MIN(dB)	S12MAX(dB)
15	-0.0004	-85.9
30	-0.0010	-76.7
50	-0.0046	-61.2
60	-0.0031	-64.9

Table 3.11: IDT pairs simulation results

3.3. Frequency domain simulation

Supporting simulations on the number of IDT pairs and delay line lengths confirm that the final SAW device design achieves sufficient signal amplitude with minimal reflections. The final design must meet the following requirements:

- Achieve sufficient signal amplitude at the resonant operating frequency.
- Minimize reflected signals at the input and output to reduce uncertainties in velocity fitting.
- Increase delay line length to reduce the effect of the length of the IDTs itself on the distance travelled by the wave.

3.3.1. IDT pairs and Delay line lengths

To achieve a large transmission, a short delay distance and a large number of IDT pairs are required. Conversely, to reduce reflection and fitting uncertainties, a long delay distance is also beneficial. This simulation uses the 2D model in Fig.3.8 to analyze the effect of the number of IDTs and delay line length on amplitude and reflection. The working wavelength is 14μm(3.5μm electrode width). The substrate used in this simulation is AlN on Si, and all other parameters remain consistent with the previous AlN on silicon simulation.

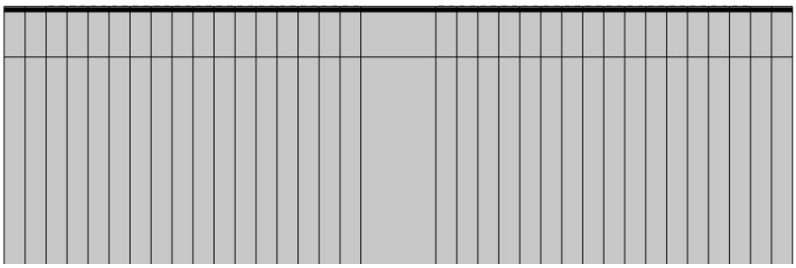

Figure 3.8: 2D simulation model for delay line length and IDT pairs

Fig.3.9 presents the simulation results for varying the number of IDT pairs N, with a delay line distance L of 50 μm. Tab.3.11 summarises the maximum magnitude of the frequency response corresponding to different numbers of IDT pairs. The simulation results show that increasing the number of IDTs increases the amplitude of the signal. Additionally, as the number of IDTs increases, the delay length changes, which increases transmission paths for the mechanical wave signals and increases losses during transmission, causing a drop in S12 amplitude at 60 pairs. Since Comsol simulation is too slow, Section5.3.2 continues to find the most optimal design through an experimental approach.

Fig.3.10a and Fig3.10b compare the frequency response of the 50 pairs IDT for 50μm and 1000μm delay distance cases, and it can be seen that 1000μm delay distance has smaller reflections, but their amplitude does not change much. In practice, SAW energy decreases as the propagation distance increases, leading to a reduction in response amplitude. However, since COMSOL does not provide damping values for the materials used, related simulations could not account for this effect. Therefore, this aspect will be investigated experimentally, with the results presented in Chapter 5.

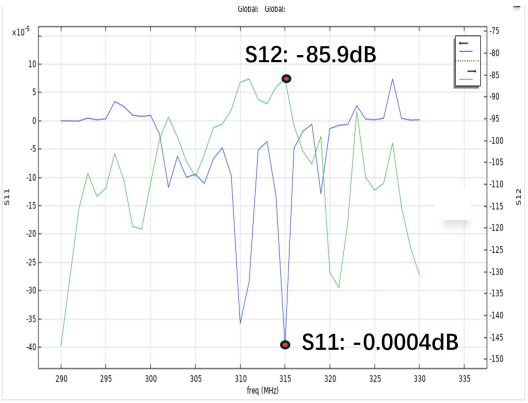

(a) 15 pairs of IDTs

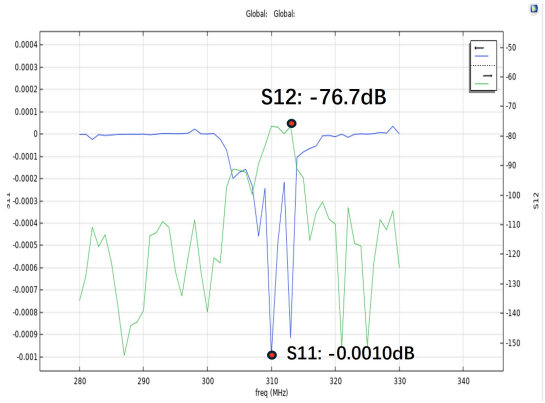

(b) 30 pairs of IDTs

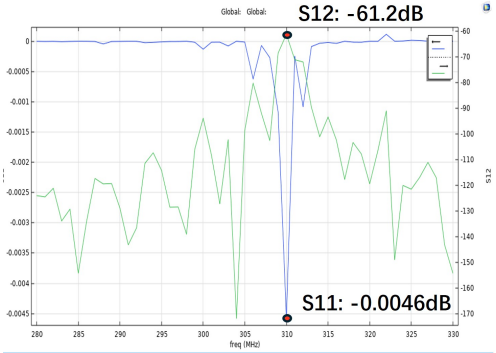

(c) 50 pairs of IDTs

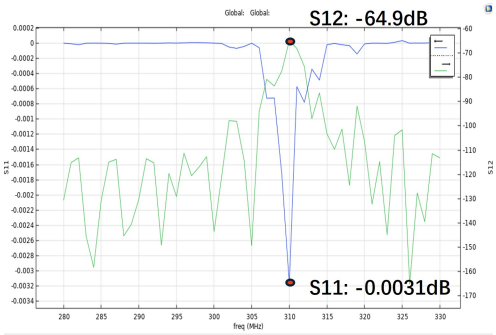

(d) 60 pairs of IDTs

Figure 3.9: IDT pairs simulation results

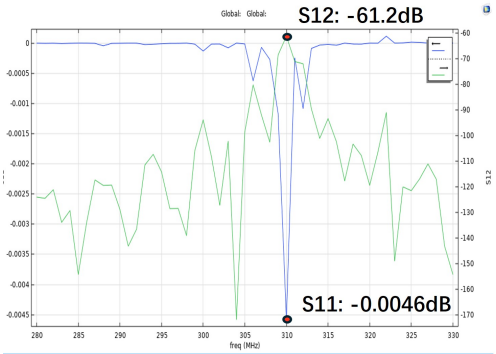

(a) 50 pairs of IDTs with 50μm delay distance

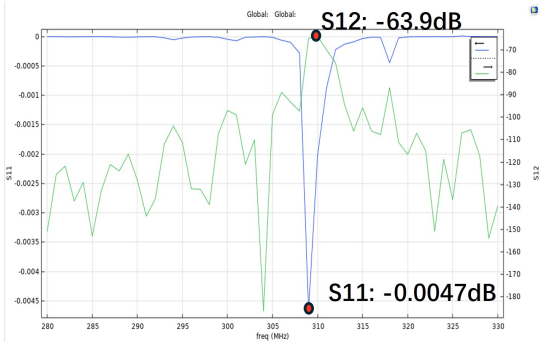

(b) 50 pairs of IDTs with 1000μm delay distance

Figure 3.10: Delayline length simulation

4

Fabrication of III-V SAW devices

This chapter focuses on the fabrication process. This project has required the fabrication of several SAW devices with AlN/Si and GaN/Si substrates. The first part of this chapter describes the AlN and GaN substrates and the second part is detailed information on the process flow. The last part shows the results of manufacturing the experimental and final samples.

4.1. Substrates Overview

4.1.1. Aluminum nitride on silicon substrate

The purpose of fabricating SAW devices on AlN substrates is to verify the feasibility of the manufacturing process while providing a comparison with GaN devices. The AlN film was deposited in the Else Kooi Laboratory (EKL). The Si substrate was provided by EKL, Tab.4.1 shows detailed information.

Standard cleaning steps include wet etching with 99% HNO_3 to dissolve organics and 69.5% HNO_3 at $110°C$ to dissolve metals (omitted after aluminum deposition). AlN (1 μm) was deposited by sputtering in the TRIKON SIGMA 204 (reactive pulsed DC, 250 kHz frequency, 1616 ns pulse width). This energy provides high pressure to the magnetron system, which ionizes the argon and nitrogen gases through high-energy electromagnetic waves. Argon ions bombard the target Al material, and the resulting Al atoms combine with nitrogen ions to deposit an AlN film on the Si surface.

4.1.2. Gallium nitride on silicon substrate

The GaN/Si wafer was acquired from DOWA Ltd, which is grown via Metal Organic Chemical Vapor Deposition (MOCVD). There is a superlattice buffer that interfaces between the Si substrate and the GaN film, but the specific details of the buffer are unavailable due to manufacturer confidentiality. Additional information regarding the GaN wafer can be found in the AppendixA.1.1.

4.2. Flowchart Detials

The flowchart sketch is shown in Fig.4.2, which starts with the AlN stack or GaN stack, and all the fabrication is done in Kavli Nanolab Delft. The complete fabrication process is detailed in the AppendixA.1.2.

Firstly, the 4-inch wafer was diced into $16cm \times 16cm$ square samples, as shown in the dicing map

Type	Resistivity	Thickness	Diameter
P-Type $< 111 >$Si	$1000\Omega.cm$	$500\ \mu m\ \pm\ 10\ \mu m$	$100mm\ \pm\ 0.5mm$

Table 4.1: Basic information about the silicon substrate

in the AppendixA.1.3.

The second step involved cleaning the samples to remove the photoresist and other impurities from the previous steps using DMSO at $80°$C, followed by acetone, isopropanol, and deionized water cleaning, assisted by ultrasonic vibration.

In the third step, an adhesion layer was applied, followed by spin-coating the photoresist. Hexamethyldisilazane (HMDS) was used to improve adhesion, and the photoresist $AR-P5350$ was coated at 4000 rpm, followed by a soft bake.

The fourth step was exposure and development, performed using maskless photolithography. The development process used a specific developer solution, as described in the flowchart.

Metal deposition was carried out in the fifth step, with titanium and aluminum layers deposited using E-beam physical vapor deposition. The photoresist descum step was performed before deposition to ensure smooth structures.

Finally, the lift-off process removed the excess metal, leaving the desired electrode structure on the sample surface. A cleaning step was performed afterward.

Fig.4.1 presents the IDTs images of a 12 μm wavelength device after exposure and liftoff.

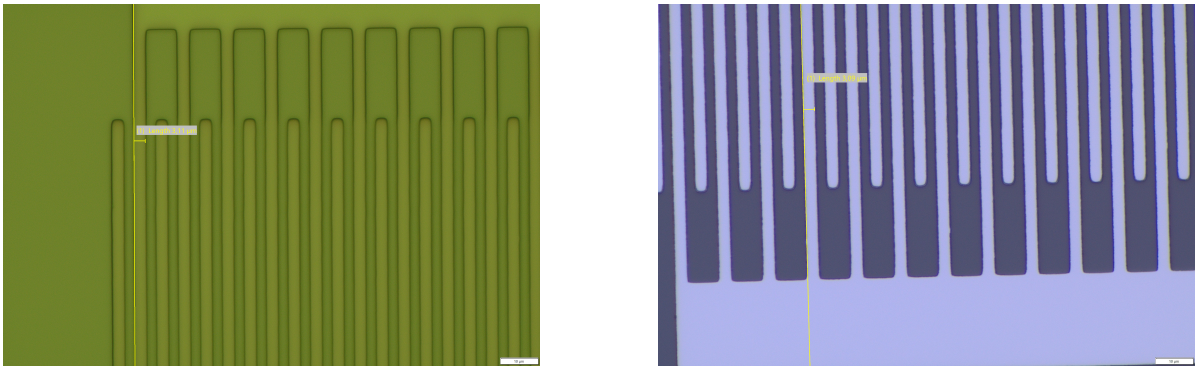

(a) The image after exposure

(b) The image after lift off

Figure 4.1: Images of the device after exposure and liftoff under a 50x microscope

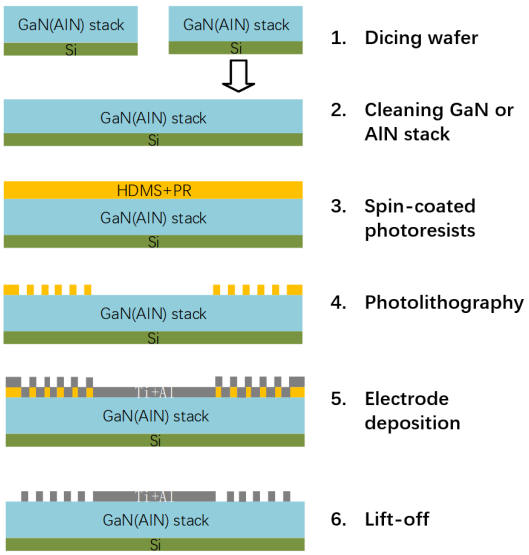

Figure 4.2: Flowchart sketch

4.3. Devices Overview

Based on the conclusion of the simulations in Chapter 3. There will be two designs in this project, the first is a verification design that varies the length of the delay line and the number of IDT pairs, and the second is a design that explores the coupling coefficients at different wavelengths.

4.3.1. Delay line length and IDT Pairs design

This design is used to investigate the effect of different IDT pairs and different delay line lengths on the device's operating frequency, signal peak amplitude, and reflections. The design compensates for the lack of stimulation and also provides a reference for subsequent studies on changing wavelengths. The detailed parameters of these designs are shown in Tab.4.2. All these designs are fabricated on AlN substrates and the working wavelength should be 12um. The electrodes will use Au and Al. The masks are shown in the Appendix. Some of the images are shown in Fig4.3.

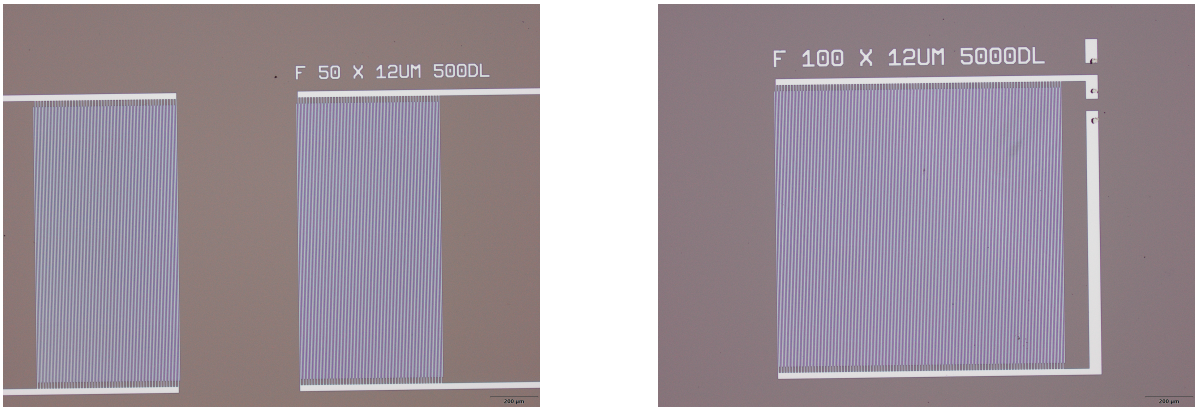

(a) The device with 500μm delay length

(b) The device with 100 finger IDTs

Figure 4.3: Images some of the delay line length and IDT Pairs design devices

Degien	Change the N	Change the L
b (μm)	3	3
a (μm)	3	3
w(μm)	1150	1150
N(single side)	$30-100$,step 10	50
L (μm)	5000	$500; 1000-10000$,step 1000
pad size (μm)	50X100	50X100
pad distance (μm)	50	50

Table 4.2: Detail parameters of IDT pairs design(change N) and delay line length design(change L) (the sketch is shown in Fig.2.7. a: electrode width;b electrode pitch;L: delay line length;w electrode overlap;N: the number of IDT pairs.)

4.3.2. Wavelength design

This design will analyze the effect of different wavelengths on the coupling coefficients of the SAW device and is an indirect characterization of the piezoelectric properties. The working wavelength changes from 6um to 18um with 2 step and every different wavelength device have one free surface delay line, one short circuit surface delay line and one zero distance delay line which aims to eliminate the errors at the data processing step. This design will be fabricated on both AlN and GaN substrates. The detailed parameters are shown in Tab.4.3. The masks are shown in the AppendixA.1.4. Some images of AlN and GaN devices are shown in Fig.4.4.

b (μm)	$1.5-4.5$,step1.5
a (μm)	$1.5-4.5$,step1.5
w(μm)	1150
N(single side)	50
L(μm)	10000
pad size (μm)	50X100
pad distance (μm)	50

Table 4.3: Detail parameters of changign the wavelength design (the sketch is shown in Fig.2.7. a: electrode width;b electrode pitch;L: delay line length;w electrode overlap;N: the number of IDT pairs.)

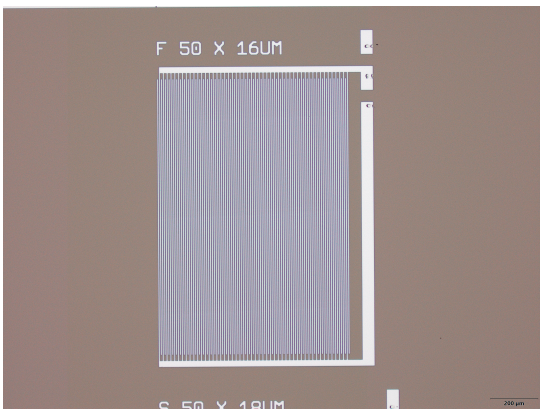

(a) AlN free surface device with 16μm operation wavelength

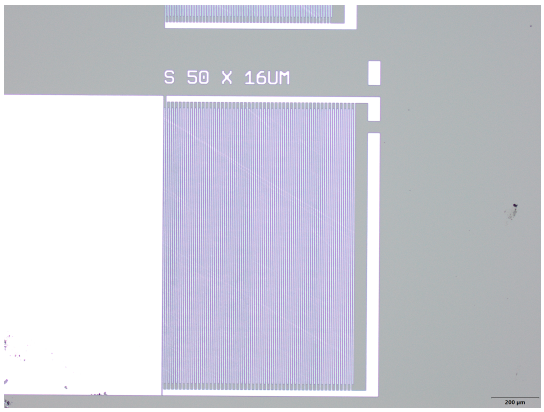

(b) AlN short circuit surface device with 16μm operation wavelength

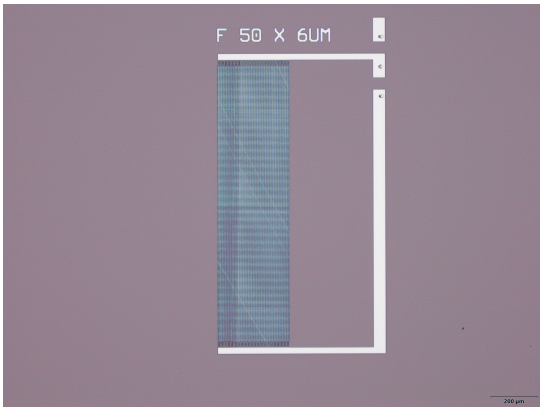

(c) GaN free surface device with 6μm operation wavelength

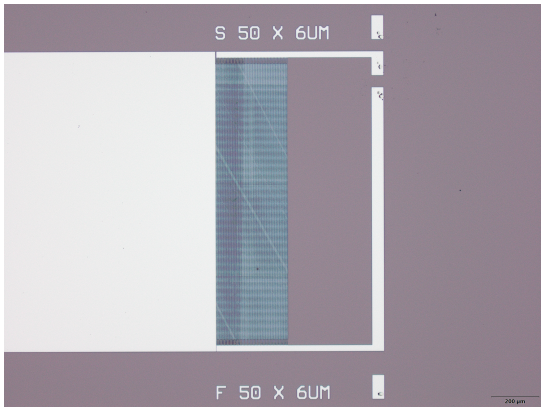

(d) GaN short circuit surface device with 6μm operation wavelength

Figure 4.4: Images of AlN and GaN devices

5

Measurement and results

In this chapter, the measurement setup, and data processing method are explained. The results for AlN and GaN SAW devices are compared and conclusions are given.

5.1. Measurement Setup

The measurement setup is displayed in Fig.5.1. The probe consists of three needles with 150 μm pitch which is Ground-Signal-Ground(GSG). The probes are connected to a Keysight P9370A Vector Network Analyzer (VNA) via 1.5-meter-long blue SMA cables. Red cables are used to ground the probe station. The VNA is interfaced with a computer running software that displays and stores the S-parameters. Measurements are performed over a frequency range of 1 MHz to 11 MHz, sampled at 10,003 discrete points.

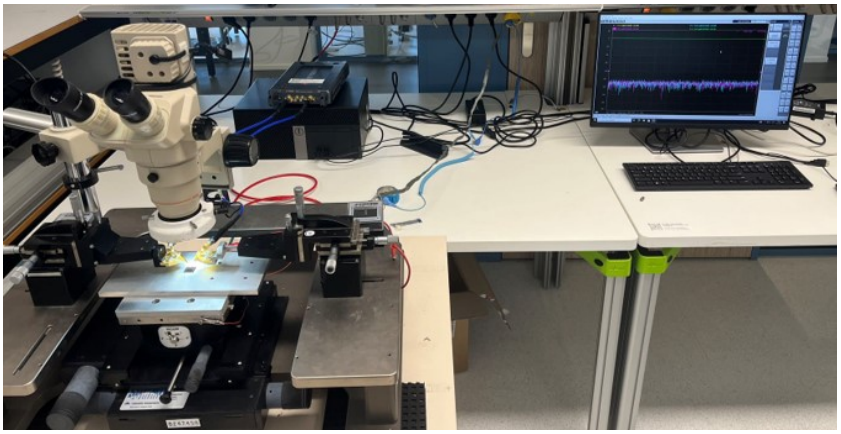

Figure 5.1: Probe station measurement set up

5.2. Data Processing

The S21 parameter is stored in .csv files and the frequency response is analyzed using Matlab. Based on the harmonic wave propagation function Eq.2.17. The slope of the change in phase with frequency is the transmission time of the acoustic wave between the two IDTs, which is calculated by linear fitting. The frequency response of the 10000μm delay length, 12μm operation frequency AlN SAW devices, and its liner fitting result are shown in Fig.5.2. The slope is -2.1102×10^{-6}. So the delay time is 2.1102 μs. The propagation distance is from IDTs' center to center which is 0.0106m. So the velocity is 5023.1395m/s.

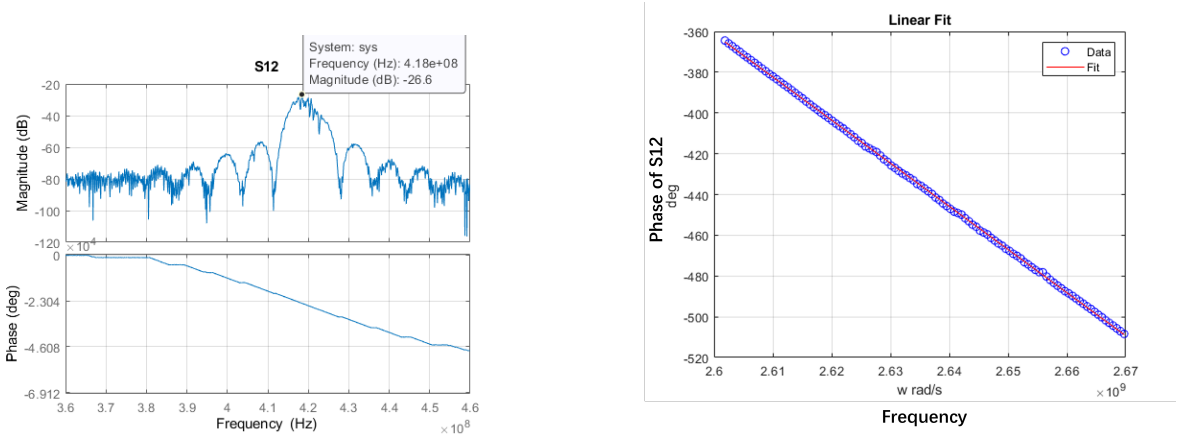

(a) Frequency response

(b) The liner fitting

Figure 5.2: AlN SAW device frequency response(10000μm delay length, 12μm operation wavelength,50 pairs IDTs)

5.3. Delay line length and IDT Pairs design results

5.3.1. Au and Al electrodes

Fig.5.3a shows the spectra of the SAW device with Au electrodes. The working frequency is 395.53MHz with 43.178dB insertion loss. The bode plot of this device is shown in Fig.5.3b. Significant phase fluctuations across the frequency range make it challenging to accurately fit the wave velocity. The frequency response is very different from the ideal case and the signal reflection is very severe, other devices with Au electrodes exhibit similar waveforms. Due to the suboptimal performance of the Au electrode devices, further measurement results will not be presented. In contrast, Fig.5.3c shows the spectra of the SAW device which have the same design as the device shown in Fig.5.3a except using Al electrodes. The working frequency is 419.2MHz with 30.35dB insertion loss. The corresponding bode plot is shown in Fig.5.3d. A comparison of the spectra between devices with Au and Al electrodes reveals that Au electrodes result in greater reflections and larger phase fluctuations, which are not favorable for fitting the phase delay time. So other design will use Al as electrodes.

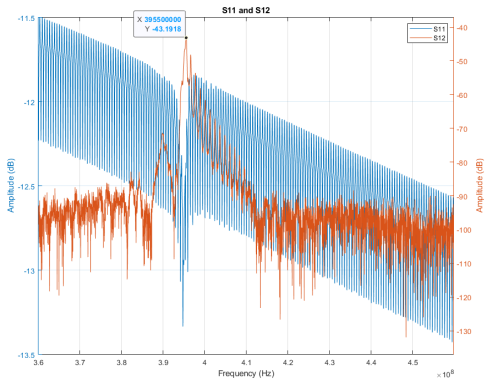

(a) The Au electrodes SAW spectra

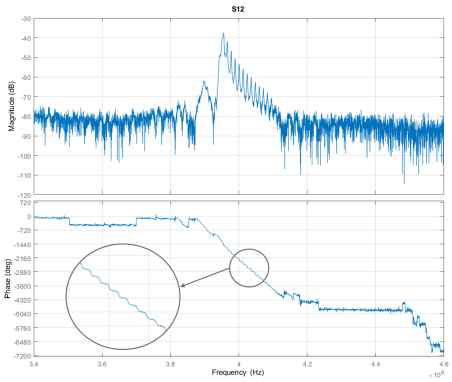

(b) The Au electrodes SAW S12 Bode plot

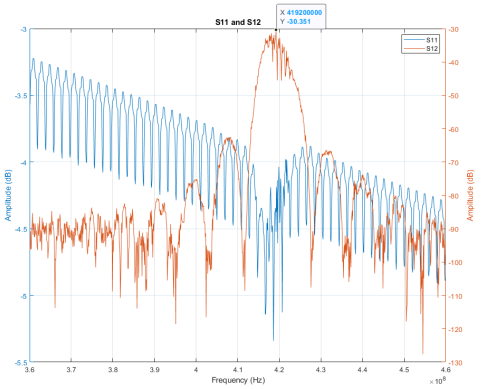

(c) The Al electrodes SAW spectra

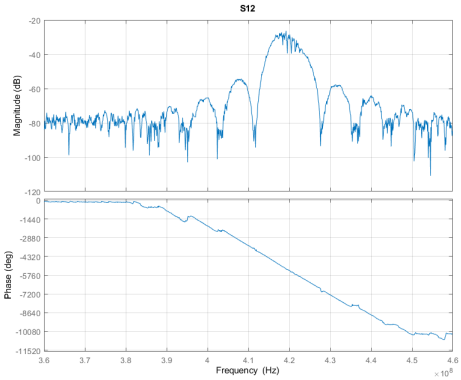

(d) The Al electrodes SAW S12 Bode plot

Figure 5.3: Al and Au electrodes SAW devices with 50pairs IDTs; 2000μm delay line length and 12μm operating wavelength

5.3.2. Varying the number of IDT pairs

Tab.5.1 summarizes the insertion loss, and wave velocity of different numbers of IDT pairs SAW devices. All devices have 5000μm delay line length and 12μm operating wavelength. The results are illustrated in Fig.5.4. The measurements indicate that the insertion loss generally decreases as the number of IDT pairs increases, except for the device with 90 pairs of IDTs. This anomaly is attributed to a scratch incurred during fabrication, which significantly affected signal transmission and increased the insertion loss, as shown in Fig.5.5a. The wave velocity remains consistent across all devices. The S12 responses of the SAW devices with 30, 50, 90, and 100 IDT pairs are depicted in Fig.5.6. A comparison of these responses is shown in Fig5.7. Based on these waveforms, it is evident that increasing the number of IDT pairs results in a narrower bandwidth, which aligns with the theory. Other measurement results are shown in the AppendixA.2.1.

IDT pairs	S12(dB)	Phase velocity(m/s)
30	-31.3	5032.60
40	-28.6	5053.51
50	-26.6	5062.75
60	-26.1	5071.09
70	-24.6	5018.27
80	-23.9	5027.28
90	-43.2	5002.23
100	-25	5061.86

Table 5.1: IDT pairs design measurement results(12μm operating wavelength; 5000μm delay line length)

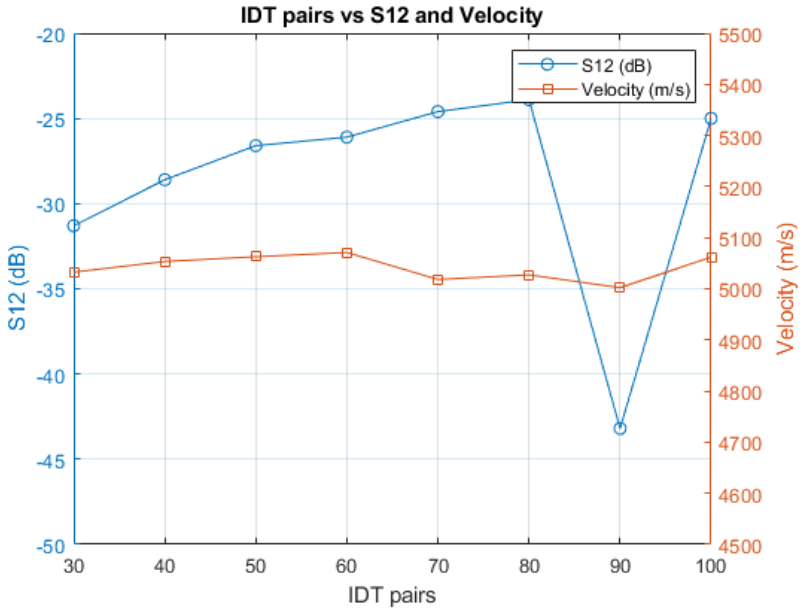

Figure 5.4: Measurement results of different numbers of IDT pairs SAW (12μm operating wavelength; 5000μm delay line length)

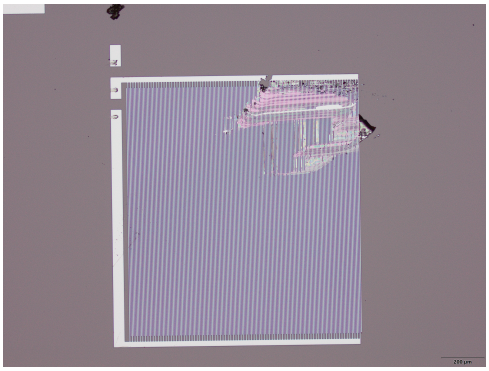

(a) The defect of 90 pairs of IDTs AlN SAW device

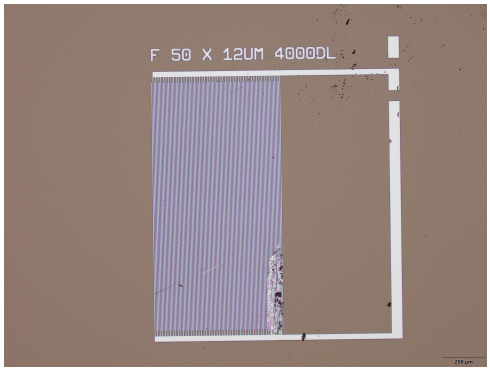

(b) The defect of 4000μm delay length AlN SAW device

Figure 5.5: AlN SAW devices defects(12μm operating wavelength; 5000μm delay line length)

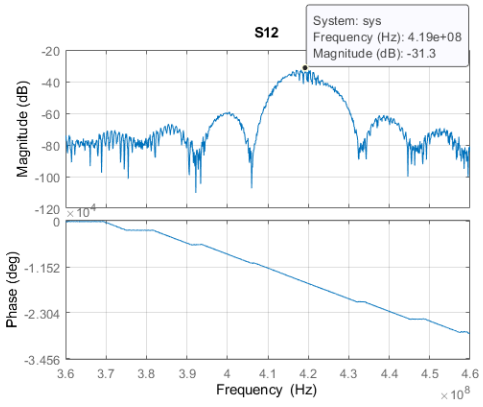

(a) 30 pairs of IDT

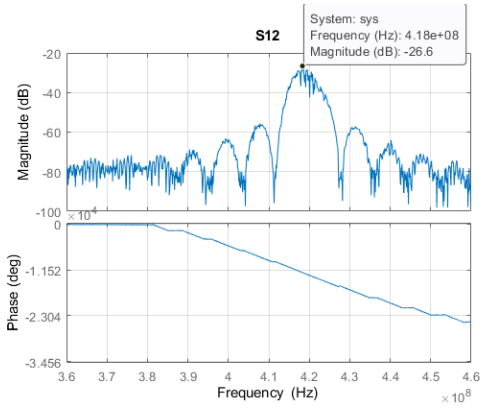

(b) 50 pairs of IDT

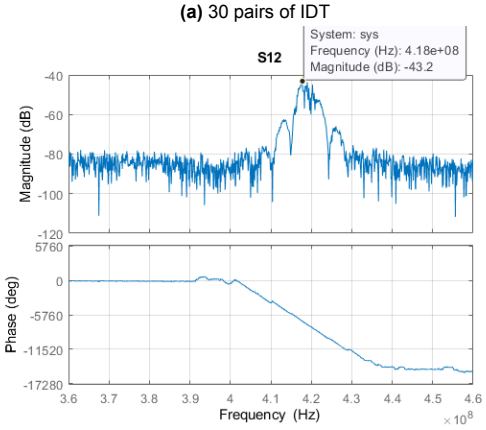

(c) 90 pairs of IDT

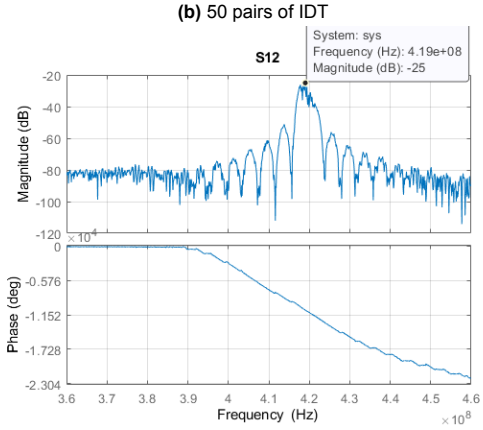

(d) 100 pairs of IDT

Figure 5.6: Different number of IDT pairs AlN SAW devices S12 frequency response(12μm operating wavelength; 5000μm delay line length)

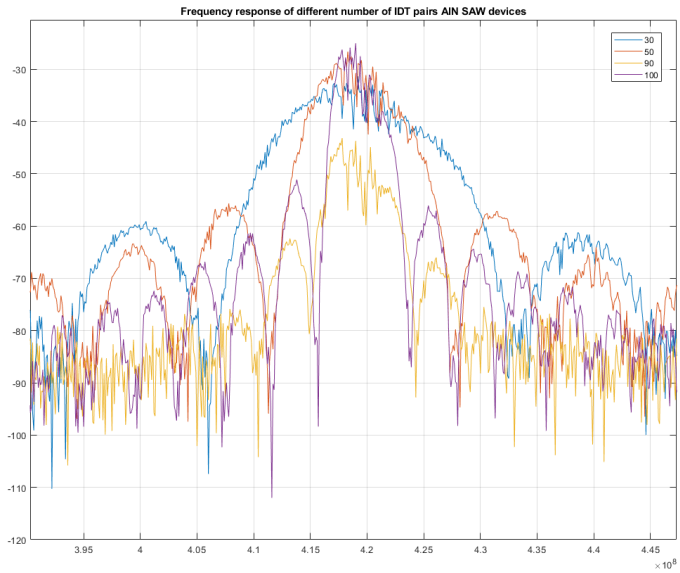

Figure 5.7: Comparison of AlN SAW devices measurement results (IDTs pairs: 30,50,90,100)

5.3.3. Varying the Delay line length

Fig.5.8 summarizes the measured insertion loss and wave velocity for SAW devices with varying delay line lengths. The wave velocities are nearly identical, within the margin of error, and the variation in insertion loss is minimal, except for the device with a 4000 μm delay length, which exhibits increased insertion loss due to electrode scratching. This device is shown in Fig.5.5b. The S12 response of the SAW devices with 500μm, 4000μm, 5000μm, and 10000μm delay length are shown in Fig.5.9. A comparison of these responses is shown in Fig5.10. According to the waveform, it is apparent that the 500μm device exhibits significant phase fluctuations with frequency and high levels of signal reflection, while the 4000μm device suffers from high insertion loss and unsatisfactory waveform quality. Other measurement results are shown in the Appendix.A.2.2.

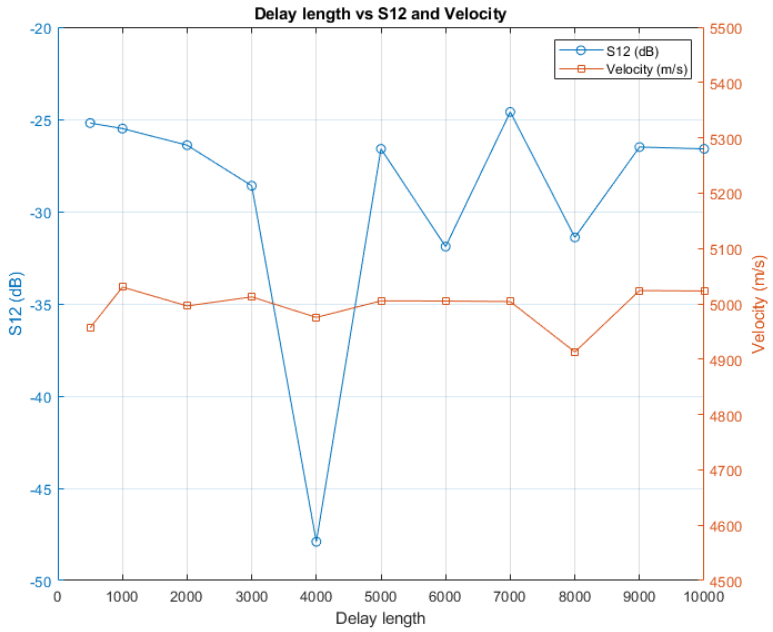

Figure 5.8: Measurement results of different delay length SAW (50 pairs of IDT; 12μm operating wavelength)

5.3.4. Conclusion

By comparing the SAW spectra of Au and Al electrodes SAW devices, it can be concluded that the low density of Al electrodes reduces SAW reflections, reduces phase fluctuations, and optimizes the frequency response. As the number of IDT pairs increases, the insertion loss decreases slightly and the bandwidth of the system decreases. Extending the delay line length does not show a clear correlation with insertion loss, though it effectively reduces reflections. Based on the above conclusions and the design requirements mentioned in Section 3.3, the devices will have a 10000μm delay length and 50 pairs of IDTs in the varying wavelength design.

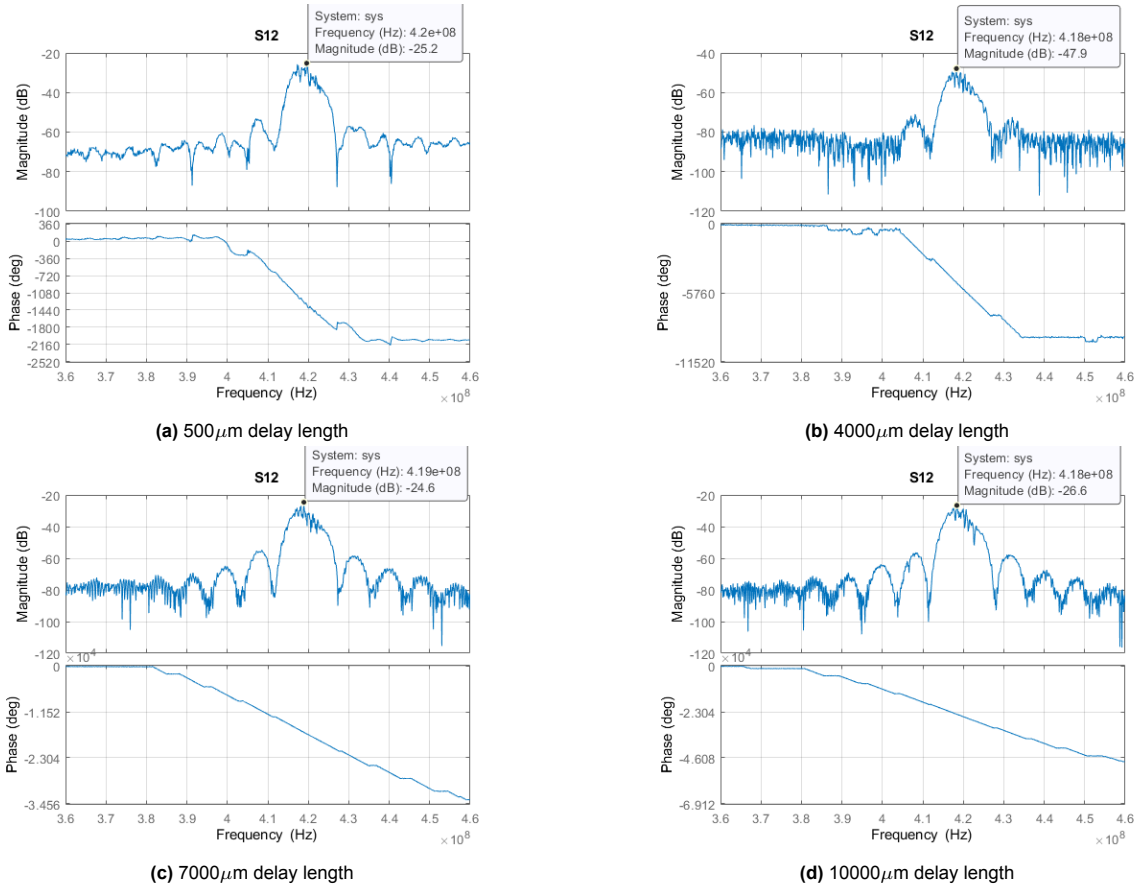

(a) 500μm delay length

(b) 4000μm delay length

(c) 7000μm delay length

(d) 10000μm delay length

Figure 5.9: Different delay length AlN SAW devices S12 frequency response(50 pairs of IDT; 12μm operating wavelength)

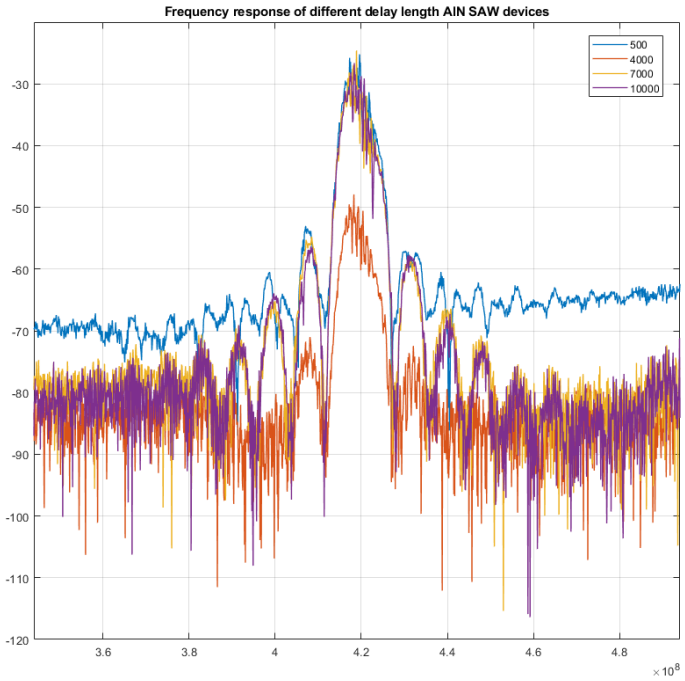

Figure 5.10: Comparison of AlN SAW devices measurement results (Delay line length: 500,4000,7000,10000)

wavelength(μm)	V_f(m/s)	V_m(m/s)	K^2(%)
8	4835.82	4677.71	6.54
10	4939.41	4661.86	11.24
12	4882.97	4572.06	12.73
14	4888.27	4636.82	10.29
16	4860.29	4653.54	8.51
18	4841.14	4651.62	7.83

Table 5.2: Varying wavelength design AlN SAW devices measurement results(V_f: the phase velocity in free surface SAW devices;V_m: the phase velocity in short circuit surface SAW devices. For the sketch, please refer to Fig.2.10)

wavelength(μm)	V_f(m/s)	V_m(m/s)	K^2(%)
6	3949.34	3901.11	2.44
8	3988.74	3929.45	2.97
12	3896.84	3845.71	2.62

Table 5.3: Varying wavelength design GaN SAW devices measurement results(V_f: the phase velocity in free surface SAW devices;V_m: the phase velocity in short circuit surface SAW devices. For the sketch, please refer to Fig.2.10)

5.4. K^2 for devices of different wavelengths

The phase velocity for both free surface and short circuit surface devices are calculated based on the method in section5.2. And the K^2 is calculated by Eq.2.10

Tab.5.2 summarizes the velocities and coupling coefficients for SAW devices with various wavelengths on AlN substrates. And Tab.5.3presents the corresponding results for GaN SAW devices. For GaN SAW devices, only devices with 8μm, 10μm, and 12μm have significant Rayleigh wave modes and wave velocity can be calculated. Fig.5.11 illustrates the relationship between the coupling coefficient K^2 and wavelength. Fig.5.12 shows the S12 response of 8 μm, and 12μm operating frequency free surface and short circuit devices on AlN substrate. Fig.5.13 shows the S12 response of 6μm, and 12μm GaN SAW devices. Other device's responses are shown in the AppendixA.2.3.

When comparing these coupling coefficients, the K^2 of AlN SAW devices are about three times larger than GaN SAW devices. This result aligns with the simulation data, indicating that the piezoelectric properties of GaN superlattice substrates are suboptimal. However, several experimental issues remain. The coupling coefficients obtained experimentally are about 10 times larger than the simulations Fig.3.3 and Fig.3.6, and neither AlN nor GaN SAW devices show good frequency response, while no Rayleigh wave modes are measured on many GaN substrate SAW devices. These problems will be analysed and discussed in Chapter 6.

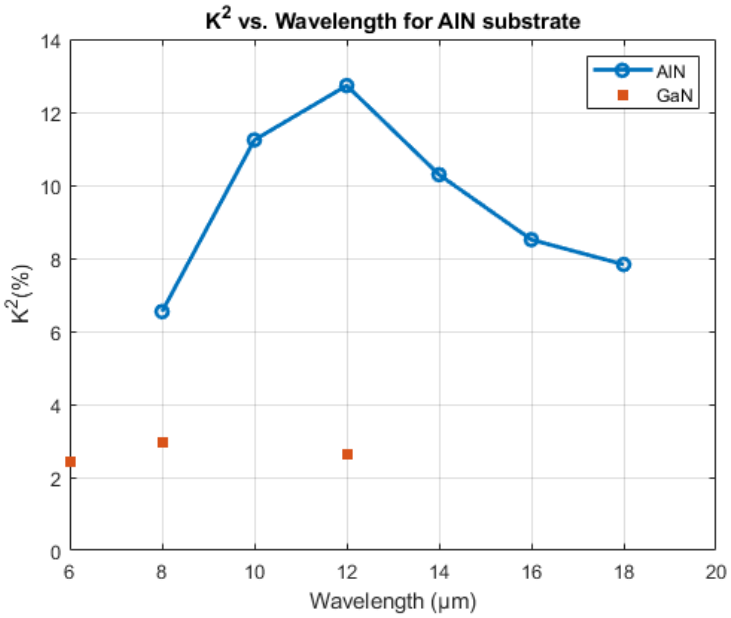

Figure 5.11: Measurement results of different operating wavelength SAW devices on AlN and GaN substrate (50 pairs of IDT; 10000μm delay length)

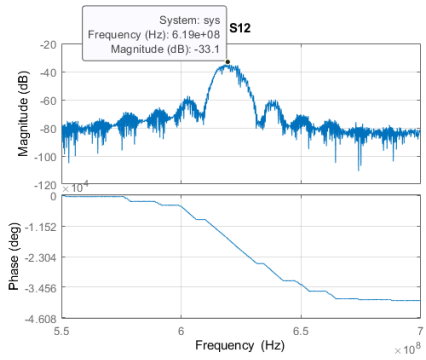

(a) 8μm free surface

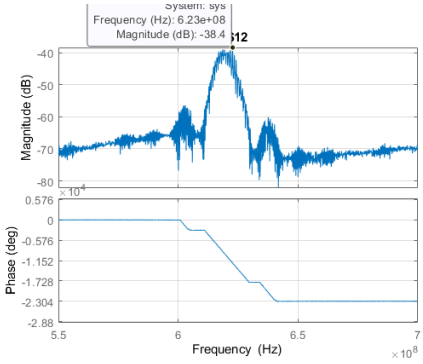

(b) 8μm short circuit surface

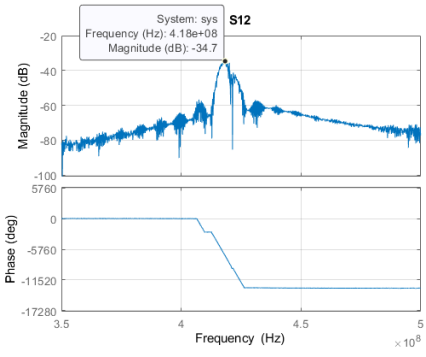

(c) 12μm free surface

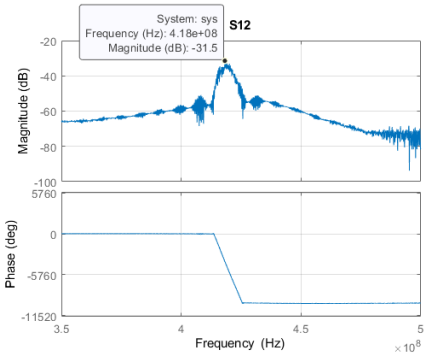

(d) 12μm short circuit surface

Figure 5.12: 8μm and 12μm operating wavelength AlN SAW S12 frequency response(50 pairs of IDTs; 10000μm delay length)

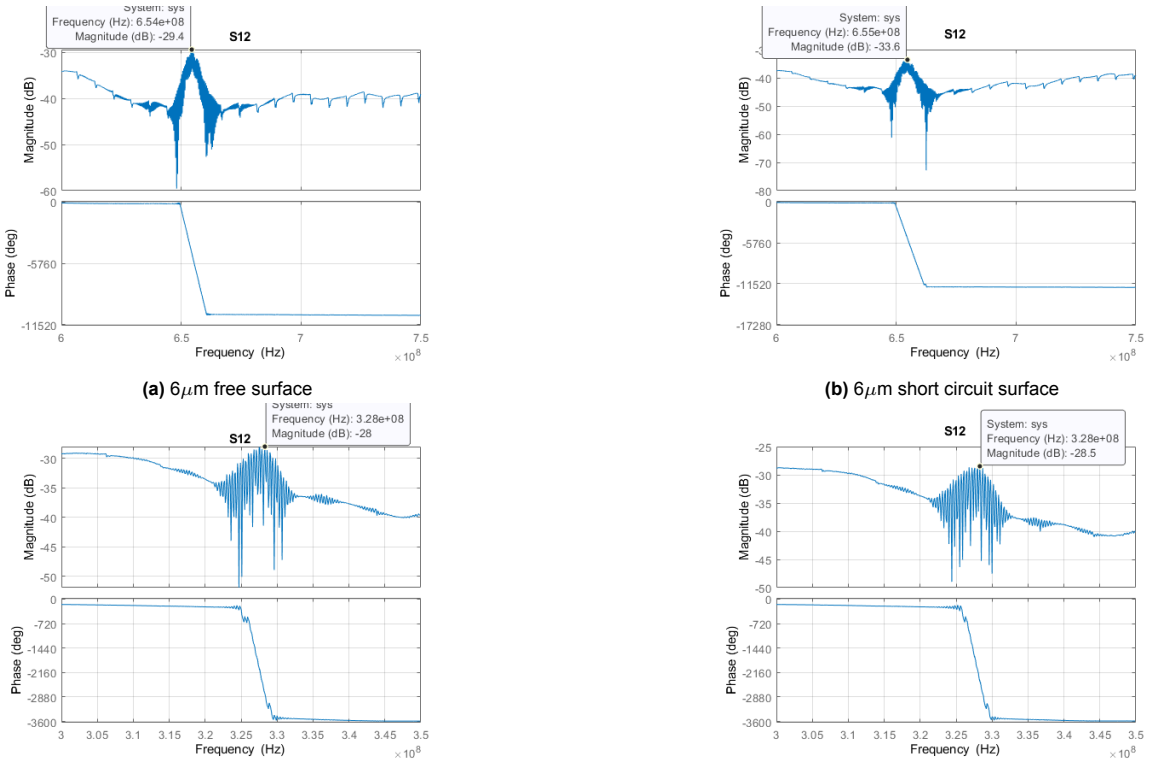

(a) 6μm free surface

(b) 6μm short circuit surface

(c) 12μm free surface

(d) 12μm short circuit surface

Figure 5.13: 6μm and 12μm operating wavelength GaN SAW S12 frequency response(50 pairs of IDTs; 10000μm delay length)

6

Discussions

This chapter focuses on a detailed analysis of the experimental results and related problems. These problems include experimentally obtained coupling coefficients that are significantly larger than the simulation, suboptimal device responses, and the absence of Rayleigh wave modes in certain GaN SAW devices. This Chapter also presents some optimization options and improvements for this project.

6.1. Problems analysis

6.1.1. Large coupling coefficient

Comparing the experimental results in section 5.4 and the simulation results in section 3.1.2, the former have very large coupling coefficients, the experimental results show significantly larger coupling coefficients, which deviate considerably from the reference and indicate potential issues. It is due to the surface metallization to implement a short circuit boundary condition. The mass loading effect[55][56] induces a decrease of the V_m beyond the decrease expected by the short circuit condition. These papers [55][56] show the changes in operation frequency(phase velocity) of SAW delay line devices with increasing mass. For acoustic wave propagation in the normal medium, the velocity is inversely proportional to the density and directly proportional to the modulus. In these short circuit SAW devices in which the surface is covered with a conductive Al film, the unit density increases, reducing the wave velocity, this in turn, causes all calculated K^2 to be larger. Young's modulus and shear modulus are 330 Gpa and 140 Gpa for AlN and 69 Gpa and 26 Gpa respectively for Al[57].In contrast, the propagation speed of acoustic waves on the surface of Al is lower because the material is more susceptible to deformation.

To validate this analysis, several simulations were performed. The model used for simulating the short-circuit devices is depicted in Fig.6.1. The thin metal layer is 200nm Al and 10nm Ti. These layers were excluded from the electrostatic field, but the bottom part was set to a floating potential to simulate the short-circuit surface. All other boundary conditions remain consistent with the model in Section 3.1. The AlN SAW devices with 50nm thickness electrodes and metal film were fabricated and measured. The responses of the 8μm and 11μm devices are shown in Fig.6.3, and other devices' responses are shown in the AppendixA.2.3. All the simulation and measurement results are summarized in Fig.6.4.

The time domain simulation results are shown in Fig.6.2, the electromagnetic wave signal transmitted from input to output within 1ns. The mechanical SAW on the free surface and short-circuit reach the output at 11.82ns and 12.04ns, respectively. The corresponding wave speeds are $V_f = 4737.17m/s$ and $V_m = 4651.67m/s$. And the $K^2 = 3.6$%, which aligns with the eigenfrequency simulation results. These simulations and experimental data confirm that the mass loading effect significantly influences the coupling coefficient."

Another factor contributing to the observed effects is the stress in the metal film[58][59]. By comparing the thermal expansion coefficient of AlN($4.2 \times 10^{-6}\ K^{-1}$), GaN ($6.2 \times 10^{-6}\ K^{-1}$)and Al($23 \times 10^{-6}$

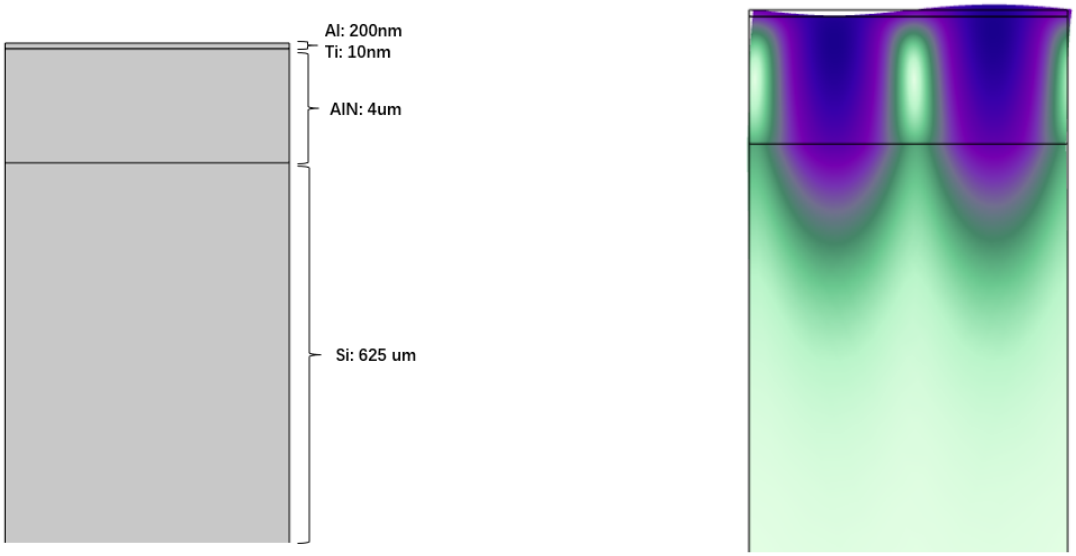

(a) The model for mass loading effect simulation

(b) The Rayleigh wave mode

Figure 6.1: The mass loading simulation model and modes

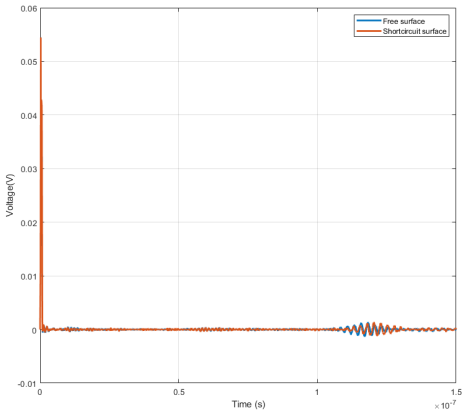

(a) output terminal voltage-time on free surface and short circuit surface SAW devices

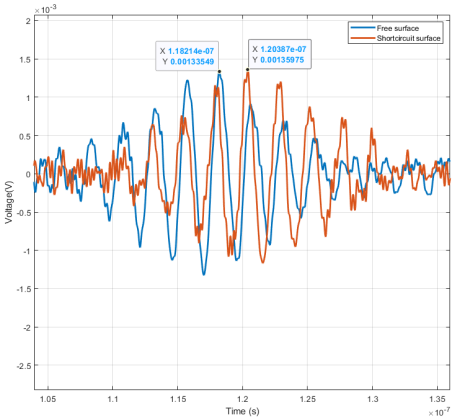

(b) Magnified plot of voltage signal

Figure 6.2: Time domain simulation results (500μm delay length, 5 pairs of IDTs, 12μm operation wavelength, AlN substrate)

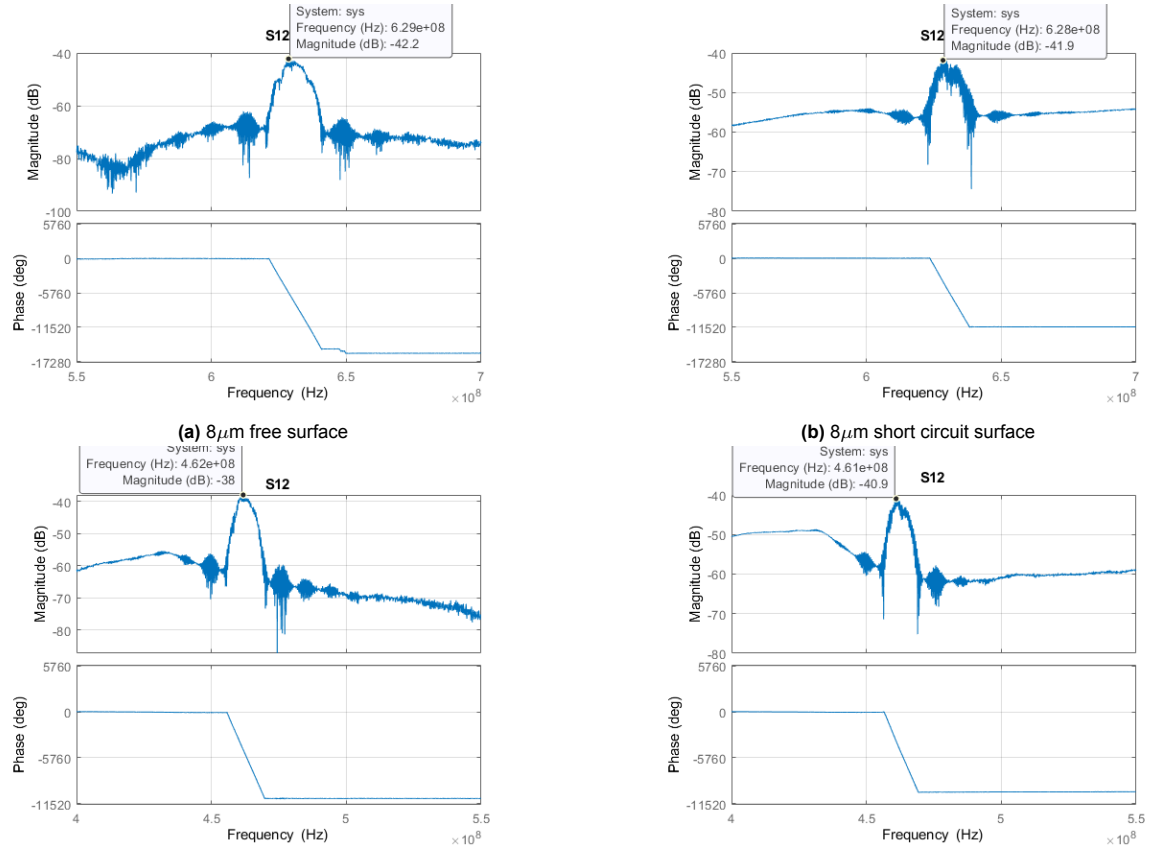

(a) 8μm free surface

(b) 8μm short circuit surface

(c) 11μm free surface

(d) 11μm short circuit surface

Figure 6.3: 8μm and 11μm operating frequency AlN SAW S12 frequency response with 50nm thickness electrodes and metal film (50 pairs of IDTs; 10000μm delay length)

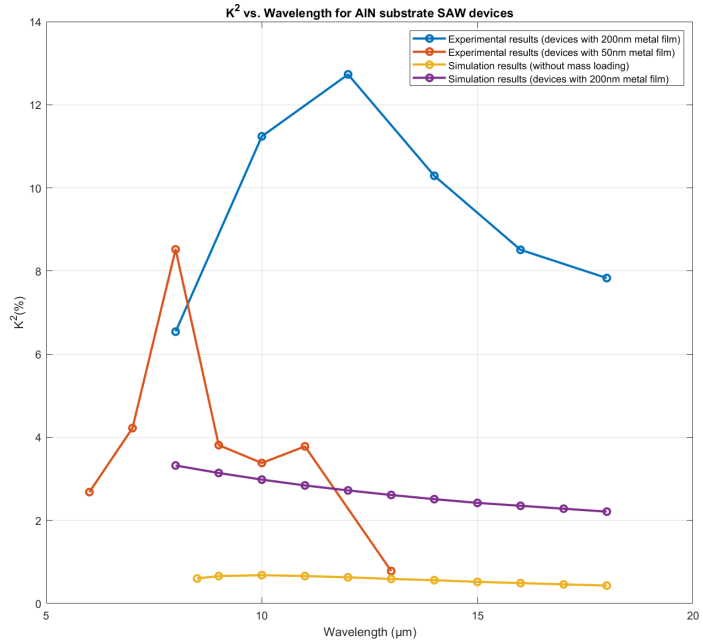

Figure 6.4: Measurement and Simulation results of AlN SAW devices including the mass loading effect

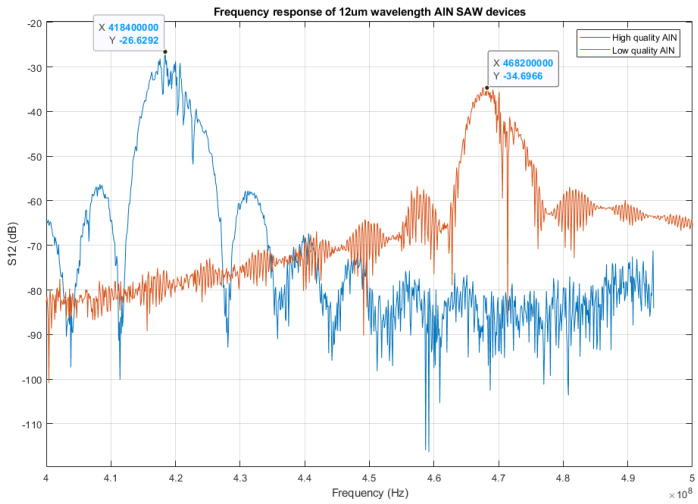

Figure 6.5: SAW devices with different quality AlN substrate responses, the comparison of Fig.5.9d and Fig.5.12c

K^{-1})[60], it is evident that the Al layer experiences compressive stress after deposition, which, in turn, exerts compressive stress on the substrate. In practice, the situation is more complex, influenced by factors such as deposition rate, method, non-uniformity in layer deposition, and the presence of defects. Further measurement is required to determine the precise direction and magnitude of the internal stress. A study by Liu et al. [61] analyzed the effect of internal stress on Love waves on quartz substrates, showing that wave speed decreases as the absolute value of internal stress increases. Since Love waves is an S wave, this conclusion can be used as a reference for understanding the impact of internal stress on Rayleigh waves.

6.1.2. Frequency response

Despite the presence of reflections, the frequency responses of the AlN SAW devices shown in Section 5.3 are relatively close to ideal, however, the responses shown in Section 5.4 are less satisfactory. When comparing the device responses in Fig.5.9d and Fig.5.12c as shown in Fig.6.5, the latter exhibits higher insertion loss and increased noise. Although the design of the devices is the same, they use different AlN substrates. The 4-inch substrate for the wavelength design is shown in Fig.6.6, revealing that the crystal quality in this batch is poor. This degradation in crystal quality increases the insertion loss of the SAW device and adversely impacts the frequency response.

The GaN SAW device's responses shown in Fig.5.13 are also suboptimal. While the variation of phase with frequency indicates the presence of surface acoustic waves, the amplitude is significantly affected by noise, primarily due to the poor piezoelectric properties of the GaN stack. The 6μm GaN SAW simulation result is shown in Fig.6.7. The operating frequency is around 650MHz which matches the measurement result in Fig.5.13a. However, the simulated waveforms are similarly less than ideal, consistent with the experimental measurements.

Fig.6.8 shows the 1MHz to 1GHz S12 response of 8μm, 10μm, 12μm and 14μm GaN SAW devices. The Rayleigh wave modes and phase delays are obvious in the 8μm Fig.6.8a and 12μm 6.8c devices. However, phase delays are not apparent in the other devices, and the amplitude is difficult to discern. Additionally, two unknown modes appear around 2 MHz and 4 MHz, potentially corresponding to electrical or mechanical signals being transmitted to the output IDTs. It is reasonable to assume that these two unknown modes influence the Rayleigh wave transmission. The phases of these two modes also vary with frequency. Due to the electric field applied in the Z-direction, the superlattice buffer layer exhibits a periodic structure. They could potentially correspond to surface waves or bulk waves propagating in the vertical direction. Due to the lack of specific data on the buffer structure, further validation cannot be performed.

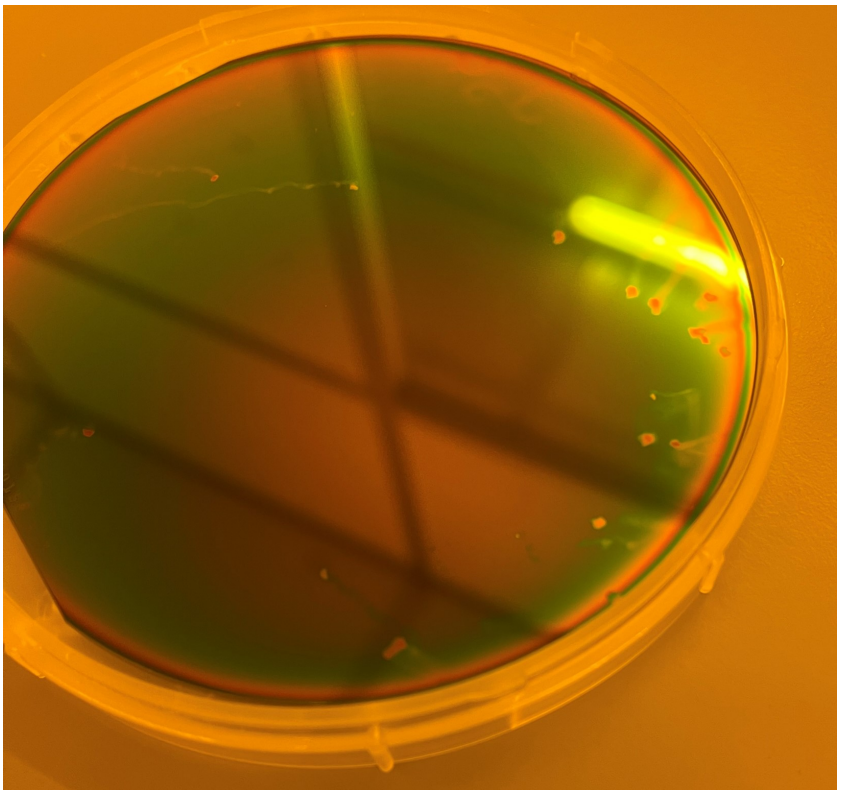

Figure 6.6: 4inch defective AlN wafer

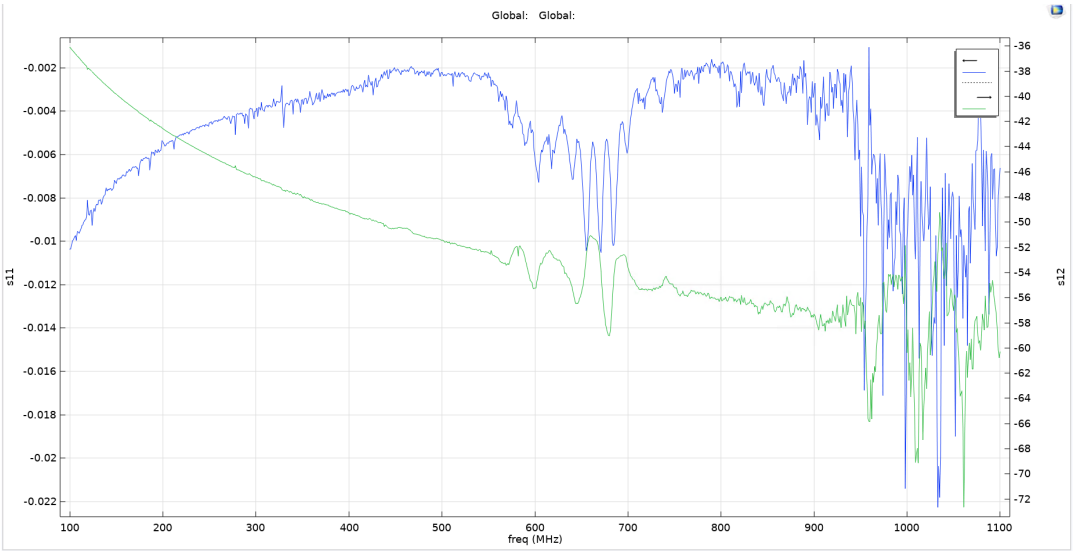

Figure 6.7: 6μm operating wavelength GaN super lattice stack SAW device frequency response

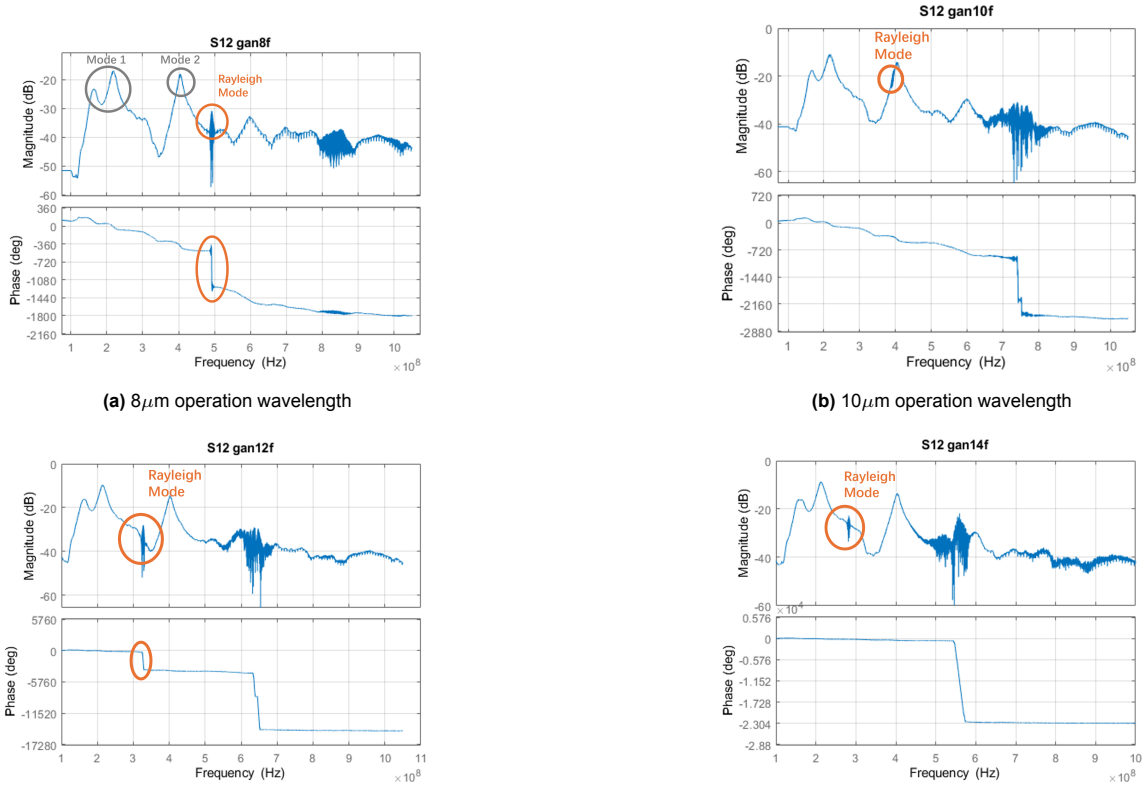

(a) 8μm operation wavelength

(b) 10μm operation wavelength

(c) 12μm operation wavelength

(d) 14μm operation wavelength

Figure 6.8: GaN devices frequency response from 1MHz to 1GHz

6.1.3. Experimental Error

Measurement errors are observed, originating from the probe station, with a particularly high noise level when measuring the S11 parameter. The S11 response is illustrated in Fig.6.9. The noise may be attributed to poor grounding, defects in the calibration samples, electromagnetic interference, platform vibrations, and other external noise sources.

Inaccuracies also arise from delay time fitting during data analysis. Another contributing factor is fabrication errors, such as uneven electrode width and spacing, which can alter the metal coverage ratio of the IDTs and subsequently affect wave velocity, as shown in Fig.6.10. There are several reasons for this fabrication error, including laser writer lithography error, error from photoresist processing, development error, and others.

6.2. Optimization options

Simulations and experiments have demonstrated that the piezoelectric performance of the superlattice GaN stack is suboptimal. A gradient GaN stack may give better results. Firstly with more AlN in the gradient buffer, the piezoelectric property is better, and secondly, by gradually changing the Al content, the discontinuity in the energy bands between AlN and GaN becomes smoother, which suppresses the generation of the 2-DEG, and potentially avoids other modes affecting the SAW mode measurement. Increasing the resistivity of the substrate also can improve the response of the SAW devices[62]. Both AlN and GaN used in this project were expitaxially grown along the (0001) direction, with the SAW propagation in the X direction, SAW devices (z-direction propagation) on AlN and GaN grown along the $(11\bar{2}0)$ direction exhibit larger piezoelectric coupling coefficients [63]. Considering only piezoelectric properties, GaN grown in this $(11\bar{2}0)$ direction may have good application prospects. Due to the potential alteration of its polarization properties, the application of GaN epitaxially grown in this direction in electronic devices requires further investigation.

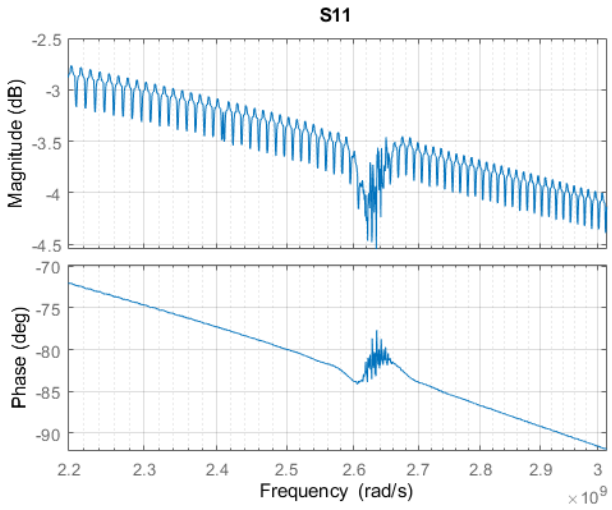

Figure 6.9: S11 response of 12μm operation wavelength AlN SAW device

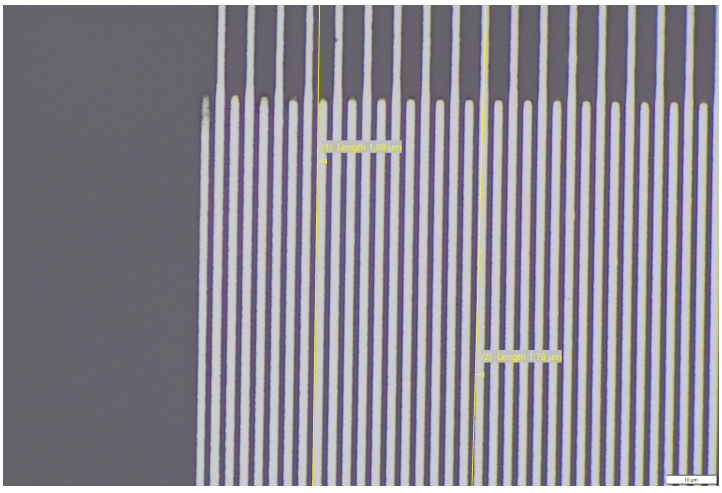

Figure 6.10: The SAW devices with electrode width designed at 1.5μm

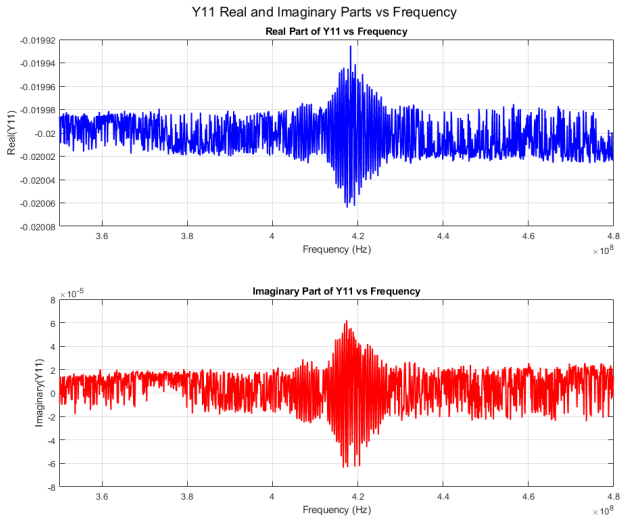

Figure 6.11: The measured Y11 value of the 12μm operation wavelength AlN SAW device

The experimental method based on Eq.2.10 has a large error due to the mass loading effect. Numerical computation of the SAW velocity can solve the errors caused by massloading[64]. Another equation can also calculate the coupling coefficient[65][66][62], which is shown in Eq.6.1[67]. Where f_0 is the center frequency, G is the conductance of the IDT at the center frequency, C_0 is the static capacitance and N is the number of finger pairs in the IDT. In contrast with Eq.2.10, this equation is more accurate[68]. G and f_0 can be obtained from Y11 by the VNA, and C_0 can be calculated[69]. Due to the high noise level from the probe station, the measured Y11 can not be used for further calculations in this method, as shown in Fig.6.11. So, this approach requires a more capable VNA and probe station. while the number of IDTs of the SAW can be increased to reduce the bandwidth, the use of low-density Al electrodes should be continued to reduce reflections.

$$k^2 = \frac{G}{8 f_0 C_0 N} \tag{6.1}$$

7

Conclusion

The main works of this thesis are summarized as follows:

- The eigenfrequency simulations of both gradient GaN buffer stack and superlattice GaN stack were presented, and the K^2 were calculated. The optimal oprating wavelength of GaN stacks are found. The simulation results indicate that the gradient buffer layer exhibits superior piezoelectric performance.

- Simulations analyzed the effect of reflected signals on the frequency response of the SAW device, investigating the relationship between signal distortion, reflected signal amplitude, and delay. The impact of Au and Al electrodes on SAW reflection was analyzed experimentally. The results show that low-density Al electrodes have smaller reflections and are more suitable for manufacturing SAW delay line devices.

- The effects of delay line length and the number of IDT finger pairs on frequency response were analyzed by experiments and simulations, leading to the design of an optimized SAW device for this project.

- SAW devices were successfully fabricated and measured on both AlN and GaN substrates, and the K^2 were calculated, which were 6.54% - 12.73% for the AlN devices and 2.44% - 2.97% for the GaN devices. It was concluded that the superlattice buffer GaN stack has poor piezoelectric properties.

- The discrepancy between experimentally obtained K^2 values and simulation results was further investigated. The effect of mass loading effect on the K^2 values is demonstrated experimentally and through simulation, and the potential influence of internal stresses is also analyzed. Other sources of error are present and relevant explanations of the GaN device measurement results are given.

- Some optimizations for this project are proposed. The gradient buffer layer is suggested for better piezoelectric performance. Additionally, using a new method to analyze Y11 can reduce errors and yield more accurate results.

References

[1] Roger D Launius. “The historical dimension of space exploration: reflections and possibilities”. In: *Space Policy* 16.1 (2000), pp. 23–38. ISSN: 0265-9646. DOI: https://doi.org/10.1016/S0265-9646(99)00055-7. URL: https://www.sciencedirect.com/science/article/pii/S0265964699000557.

[2] E.G. Stassinopoulos and J.P. Raymond. “The space radiation environment for electronics”. In: *Proceedings of the IEEE* 76.11 (1988), pp. 1423–1442. DOI: 10.1109/5.90113.

[3] John D Wrbanek and Susan Y Wrbanek. “Space radiation and impact on instrumentation technologies”. In: (2020).

[4] Raymond F. Jurgens. “High-Temperature Electronics Applications in Space Exploration”. In: *IEEE Transactions on Industrial Electronics* IE-29.2 (1982), pp. 107–111. DOI: 10.1109/TIE.1982.356645.

[5] Richard H Maurer et al. “Harsh environments: space radiation”. In: *Johns Hopkins APL technical digest* 28.1 (2008), p. 17.

[6] Ramazan Uzel and Alime Özyildirim. “A study on the local shielding protection of electronic components in space radiation environment”. In: *2017 8th International Conference on Recent Advances in Space Technologies (RAST)*. 2017, pp. 295–299. DOI: 10.1109/RAST.2017.8003007.

[7] Vinod Kumar Khanna. *Extreme-Temperature and Harsh-Environment Electronics (Second Edition)*. 2053-2563. IOP Publishing, 2023. ISBN: 978-0-7503-5072-3. DOI: 10.1088/978-0-7503-5072-3. URL: https://dx.doi.org/10.1088/978-0-7503-5072-3.

[8] Mina Rais-Zadeh et al. “Gallium Nitride as an Electromechanical Material”. In: *Journal of Microelectromechanical Systems* 23.6 (2014), pp. 1252–1271. DOI: 10.1109/JMEMS.2014.2352617.

[9] Volker Cimalla et al. “AlGaN/GaN based heterostructures for MEMS and NEMS applications”. In: *Solid State Phenomena* 159 (2010), pp. 27–38.

[10] Seyyed Masoud Kargar and Guangbo Hao. “An atlas of piezoelectric energy harvesters in oceanic applications”. In: *Sensors* 22.5 (2022), p. 1949.

[11] K. Uchino. “The development of piezoelectric materials and the new perspective”. en-US. In: *Advanced Piezoelectric Materials*. Dec. 2009, pp. 1–85. DOI: 10.1533/9781845699758.1. URL: http://dx.doi.org/10.1533/9781845699758.1.

[12] Xiao-hong Du, Uma Belegundu Uma Belegundu, and Kenji Uchino Kenji Uchino. “Crystal orientation dependence of piezoelectric properties in lead zirconate titanate: theoretical expectation for thin films”. In: *Japanese Journal of Applied Physics* 36.9R (1997), p. 5580.

[13] Xiao-hong Du et al. “Crystal orientation dependence of piezoelectric properties of single crystal barium titanate”. In: *Materials Letters* 40.3 (1999), pp. 109–113.

[14] MS Shur, AD Bykhovski, and Remis Gaska. “Pyroelectric and piezoelectric properties of GaN-based materials”. In: *MRS Online Proceedings Library (OPL)* 537 (1998).

[15] Chang-Beom Eom and Susan Trolier-McKinstry. “Thin-film piezoelectric MEMS”. In: *Mrs Bulletin* 37.11 (2012), pp. 1007–1017.

[16] Rui MR Pinto et al. “CMOS-Integrated aluminum nitride MEMS: A review”. In: *Journal of Microelectromechanical Systems* 31.4 (2022), pp. 500–523.

[17] AF Wright and JS Nelson. “Consistent structural properties for AlN, GaN, and InN”. In: *Physical Review B* 51.12 (1995), p. 7866.

[18] Wikimedia Commons. *Wurtzite polyhedra*. https://commons.wikimedia.org/wiki/File:Wurtzite_polyhedra.png. Accessed on: 2023-04-10. 2021.

[19] *Dynamic Periodic Table*. https://ptable.com. Accessed on: 2023-04-10. 2023.

[20] Charles Kittel. *Introduction to solid state physics*. John Wiley & sons, inc, 2005.

[21] U.K. Mishra, P. Parikh, and Yi-Feng Wu. "AlGaN/GaN HEMTs-an overview of device operation and applications". In: *Proceedings of the IEEE* 90.6 (2002), pp. 1022–1031. DOI: 10.1109/JPROC.2002.1021567.

[22] Detlef Klimm. "Electronic materials with a wide band gap: recent developments". In: *IUCrJ* 1.5 (2014), pp. 281–290.

[23] Matthew A. Hopcroft, William D. Nix, and Thomas W. Kenny. "What is the Young's Modulus of Silicon?" In: *Journal of Microelectromechanical Systems* 19.2 (2010), pp. 229–238. DOI: 10.1109/JMEMS.2009.2039697.

[24] Debdyuti Mandal and Sourav Banerjee. "Surface acoustic wave (SAW) sensors: Physics, materials, and applications". In: *Sensors* 22.3 (2022), p. 820.

[25] CK Campbell. "Obtaining the fundamental and harmonic radiation conductances of a reflective SAW interdigital transducer". In: *1998 IEEE Ultrasonics Symposium. Proceedings (Cat. No. 98CH36102)*. Vol. 1. IEEE. 1998, pp. 169–173.

[26] Xuesong Ye et al. "Studies of a high-sensitive surface acoustic wave sensor for passive wireless blood pressure measurement". In: *Sensors and Actuators A: Physical* 169.1 (2011), pp. 74–82.

[27] Wei-zhong Wang et al. "Design and fabrication of an surface acoustic wave resonator based on AlN/4H-SiC material for harsh environments". In: *J. Zhejiang Univ. Sci. A* 18 (2017), pp. 67–74.

[28] Colin Campbell. *Surface acoustic wave devices and their signal processing applications*. Elsevier, 2012.

[29] James J Campbell and William R Jones. "Propagation of piezoelectric surface waves on cubic and hexagonal crystals". In: *Journal of applied physics* 41.7 (1970), pp. 2796–2801.

[30] Gang Bu et al. "Electromechanical coupling coefficient for surface acoustic waves in single-crystal bulk aluminum nitride". In: *Applied physics letters* 84.23 (2004), pp. 4611–4613.

[31] Mina Rais-Zadeh et al. "Gallium nitride as an electromechanical material". In: *Journal of Microelectromechanical Systems* 23.6 (2014), pp. 1252–1271.

[32] Y Takagaki et al. "Guided propagation of surface acoustic waves in AlN and GaN films grown on 4 H–SiC (0001) substrates". In: *Physical Review B* 66.15 (2002), p. 155439.

[33] F Semond. "Epitaxial challenges of GaN on silicon". In: *Mrs Bulletin* 40.5 (2015), pp. 412–417.

[34] Xu-Qiang Shen et al. "Self-generated microcracks in an ultra-thin AlN/GaN superlattice interlayer and their influences on the GaN epilayer grown on Si (110) substrates by metal–organic chemical vapor deposition". In: *CrystEngComm* 17.27 (2015), pp. 5014–5018.

[35] Kai Cheng et al. "Flat GaN epitaxial layers grown on Si (111) by metalorganic vapor phase epitaxy using step-graded AlGaN intermediate layers". In: *Journal of Electronic Materials* 35 (2006), pp. 592–598.

[36] Chang-Ju Lee et al. "Selectively enhanced UV-a photoresponsivity of a GaN MSM UV photodetector with a step-graded AlxGa1- xN buffer layer". In: *Sensors* 17.7 (2017), p. 1684.

[37] Vikrant J Gokhale et al. "Q amplification in Gallium Nitride thickness mode filters using acoustoelectric effect". In: *Tech. Dig. Solid-State Sensors, Actuators, and Microsystems Workshop*. 2010.

[38] Abdul Talukdar, Muhammad Qazi, and Goutam Koley. "High frequency dynamic bending response of piezoresistive GaN microcantilevers". In: *Applied Physics Letters* 101.25 (2012).

[39] T. Palacios et al. "High frequency SAW devices on AlGaN: fabrication, characterization and integration with optoelectronics". In: *2002 IEEE Ultrasonics Symposium, 2002. Proceedings.* Vol. 1. 2002, 57–60 vol.1. DOI: 10.1109/ULTSYM.2002.1193352.

[40] King-Yuen Wong et al. "Planar two-dimensional electron gas (2DEG) IDT SAW filter on AlGaN/-GaN heterostructure". In: *2007 IEEE/MTT-S International Microwave Symposium*. IEEE. 2007, pp. 2043–2046.

[41] Y Takagaki et al. “Guided propagation of surface acoustic waves in AlN and GaN films grown on 4 H–SiC (0001) substrates”. In: *Physical Review B* 66.15 (2002), p. 155439.

[42] RC Woods and FA Boroumand. “Comments on” Epitaxially grown GaN thin-film SAW filter with high velocity and low insertion loss””. In: *IEEE Transactions on Electron Devices* 53.1 (2005), pp. 173–176.

[43] GD O’clock and MT Duffy. “Acoustic surface wave properties of epitaxially grown aluminum nitride and gallium nitride on sapphire”. In: *Applied physics letters* 23.2 (1973), pp. 55–56.

[44] R Rimeika et al. “Electromechanical Coupling Coefficient for Surface Acoustic Waves in GaN-on-Sapphire”. In: *physica status solidi (b)* 234.3 (2002), pp. 897–900.

[45] Sun-Ki Kim et al. “Investigation of characteristics of SAW filter using undoped GaN epitaxial layer grown by MOCVD on sapphire substrate”. In: *2001 IEEE Ultrasonics Symposium. Proceedings. An International Symposium (Cat. No. 01CH37263)*. Vol. 1. IEEE. 2001, pp. 257–260.

[46] Omar Elmazria et al. “High velocity SAW using aluminum nitride film on unpolished nucleation side of free-standing CVD diamond”. In: *IEEE transactions on ultrasonics, ferroelectrics, and frequency control* 50.6 (2003), pp. 710–715.

[47] J-M Liu et al. “Piezoelectric coefficient measurement of piezoelectric thin films: an overview”. In: *Materials Chemistry and Physics* 75.1-3 (2002), pp. 12–18.

[48] J Hernando et al. “Simulation and laser vibrometry characterization of piezoelectric AlN thin films”. In: *Journal of Applied Physics* 104.5 (2008).

[49] Qing Guo, GZ Cao, and IY Shen. “Measurements of piezoelectric coefficient d 33 of lead zirconate titanate thin films using a mini force hammer”. In: *Journal of Vibration and Acoustics* 135.1 (2013), p. 011003.

[50] Jirí Fialka and Petr Beneš. “Comparison of methods of piezoelectric coefficient measurement”. In: *2012 IEEE International Instrumentation and Measurement Technology Conference Proceedings*. IEEE. 2012, pp. 37–42.

[51] Virginie Thery et al. “Effective piezoelectric coefficient measurement of BaTiO3 thin films using the X-ray diffraction technique under electric field available in a standard laboratory”. In: *Applied Surface Science* 351 (2015), pp. 480–486.

[52] N Nakamura, H Ogi, and M Hirao. “Elastic, anelastic, and piezoelectric coefficients of GaN”. In: *Journal of Applied Physics* 111.1 (2012).

[53] MS Shur, AD Bykhovski, and Remis Gaska. “Pyroelectric and piezoelectric properties of GaN-based materials”. In: *MRS Online Proceedings Library (OPL)* 537 (1998), G1–6.

[54] Yiqiang Ni et al. “Effect of AlN/GaN superlattice buffer on the strain state in GaN-on-Si (111) system”. In: *Japanese Journal of Applied Physics* 54.1 (2014), p. 015505.

[55] Zheng Zhang, Dazhong Zhu, and Zhelong Huang. “A mass-loading effect LiNbO/sub 3/SAW sensor”. In: *2001 6th International Conference on Solid-State and Integrated Circuit Technology. Proceedings (Cat. No. 01EX443)*. Vol. 2. IEEE. 2001, pp. 781–784.

[56] XL He et al. “High sensitivity humidity sensors using flexible surface acoustic wave devices made on nanocrystalline ZnO/polyimide substrates”. In: *Journal of Materials Chemistry C* 1.39 (2013), pp. 6210–6215.

[57] Elmeri Österlund et al. “Mechanical properties and reliability of aluminum nitride thin films”. In: *Journal of Alloys and Compounds* 772 (2019), pp. 306–313.

[58] M Hirao, H Fukuoka, and K Hori. “Acoustoelastic effect of Rayleigh surface wave in isotropic material”. In: (1981).

[59] Ivan Lillamand et al. “Acoustoelastic effect in concrete material under uni-axial compressive loading”. In: *Ndt & E International* 43.8 (2010), pp. 655–660.

[60] Marsetio Noorprajuda et al. “AlN formation by an Al/GaN substitution reaction”. In: *Scientific Reports* 10.1 (2020), p. 13058.

[61] H Liu, ZK Wang, and TJ Wang. “Effect of initial stress on the propagation behavior of Love waves in a layered piezoelectric structure”. In: *International Journal of Solids and Structures* 38.1 (2001), pp. 37–51.

[62] Suk-Hun Lee et al. “Epitaxially grown GaN thin-film SAW filter with high velocity and low insertion loss”. In: *IEEE Transactions on Electron Devices* 48.3 (2001), pp. 524–529.

[63] GD O’clock and MT Duffy. “Acoustic surface wave properties of epitaxially grown aluminum nitride and gallium nitride on sapphire”. In: *Applied physics letters* 23.2 (1973), pp. 55–56.

[64] Gang Bu et al. “Electromechanical coupling coefficient for surface acoustic waves in single-crystal bulk aluminum nitride”. In: *Applied physics letters* 84.23 (2004), pp. 4611–4613.

[65] RC Woods and FA Boroumand. “Comments on” Epitaxially grown GaN thin-film SAW filter with high velocity and low insertion loss””. In: *IEEE Transactions on Electron Devices* 53.1 (2005), pp. 173–176.

[66] RC Woods and X Xu. “Electromechanical coupling factor of epitaxial gallium nitride doped with magnesium”. In: *Journal of Materials Science: Materials in Electronics* 18 (2007), pp. 267–270.

[67] Clinton S Hartmann, Delamar T Bell, and Ronald C Rosenfeld. “Impulse model design of acoustic surface-wave filters”. In: *IEEE Transactions on Microwave Theory and Techniques* 21.4 (1973), pp. 162–175.

[68] Omar Elmazria et al. “High velocity SAW using aluminum nitride film on unpolished nucleation side of free-standing CVD diamond”. In: *IEEE transactions on ultrasonics, ferroelectrics, and frequency control* 50.6 (2003), pp. 710–715.

[69] SR Ponamgi and Hang-Sheng Tuan. “Theoretical calculation of capacitance of an IDT over a piezoelectric layered structure”. In: *IEEE Transactions on Sonics and Ultrasonics* 21.2 (1974), pp. 125–127.

A

Appendix

A.1. Fabrication

A.1.1. GaN superlattice stack

The wafer has a Si substrate(625μm), a superlattice buffer layer(2.4μm), and a GaN layer(1.5μm). Other measurements of the wafers are shown in Fig.A.1.

■ Properties

Lot No.	Average XRC FWHM [arcsec]*1		Thickness*2				BOW
			Centor	Average	%3σ	Uniformity*3	
	(0002)	(10-12)	[um]	[um]	[%]	[%]	[μm]
E24-5-1	709	1659	4.0	4.2	4.5	2.8	-56.5

*1 X-ray rocking curve (XRC) measured using Bruker D8.

*2 Edge Exclusion 5mm

*3 Uniformity $= \frac{\text{Max}-\text{Min}}{\text{Max}+\text{Min}} \times 100$

Figure A.1: The measurement results of GaN SL wafer provided by DOWA

A.1.2. Flow chart

1. Dicing			
Step	**Devices**	**Parameters**	**Notes**
Cleaning	Wet bench	Aceton1min+IPA1min+water	
Photoresist	Spin bench	S1805 2min @95C hotplate	
Dicing	Disco Dicer	Coated with dicing sheet Size:20X20(AlN);16X16(GaN)	
DMSO cleaning	Wet bench	DMSO 30min @80C	
Cleaning	Wet bench	Aceton1min+IPA1min+water	leave samples in liquid before drying, so dry them immediately after taking them out of the liquid.
Inspection			

2. Clean wafer			
Step	**Devices**	**Parameters**	**Notes**
Inspection	microscope		
Clean 1	wet bench	Chemical: Acetone+ IPA + waterX2 Use ultrasound when using Acetone Time: 5min + 1min + 1min X2	
Inspection			

3. Spin-coating			
Step	**Devices**	**Parameters**	**Notes**
Adhesion layer	HMDS	Chemical: HDMS Recipe: 3 Temperature: 150C	Use a common wafer to carry Bake 10 mins before start
Inspection	microscope		
Photoresist	Spin bench	Chemical: ARP5350 Recipe: 4000rpm	
Soft bake	Hot plate	Recipe: 105C Time: 4min	

4. Lithography			
Step	**Devices**	**Parameters**	**Notes**
Exposure	Laser writer	Recipe: Dose80 defoc+2	
Develop	Develop bench	Chemical: AR300-35:water = 1:2 Time: 70s	
Inspection	Microscope		

5. Deposition			
Step	**Devices**	**Parameters**	**Notes**
Descum	Tepla 300	Recipe: GAS 2(200w 200ccm) Time: 60s	
Inspection	microscope		
Deposition	Temescal Fc2000	Chemical:10nm Ti/ 200nm Al Recipe: Ti-0.5A/s, Al-2A/s	

6. Lift off			
Step	**Devices**	**Parameters**	**Notes**
Stripe	Wet bench Ultrasound	Chemical: NMP or PRS3000 Recipe: 60C Time: Overnight Ultrasound	
Inspection	Lift off microscope		
Rinse	Wet bench	Chemical: Acetone + IPA X2 Recipe: 1min + 1min X 2	
Inspection	Microscope		

Figure A.2: Fabrication flowchart

A.1.3. Dicing

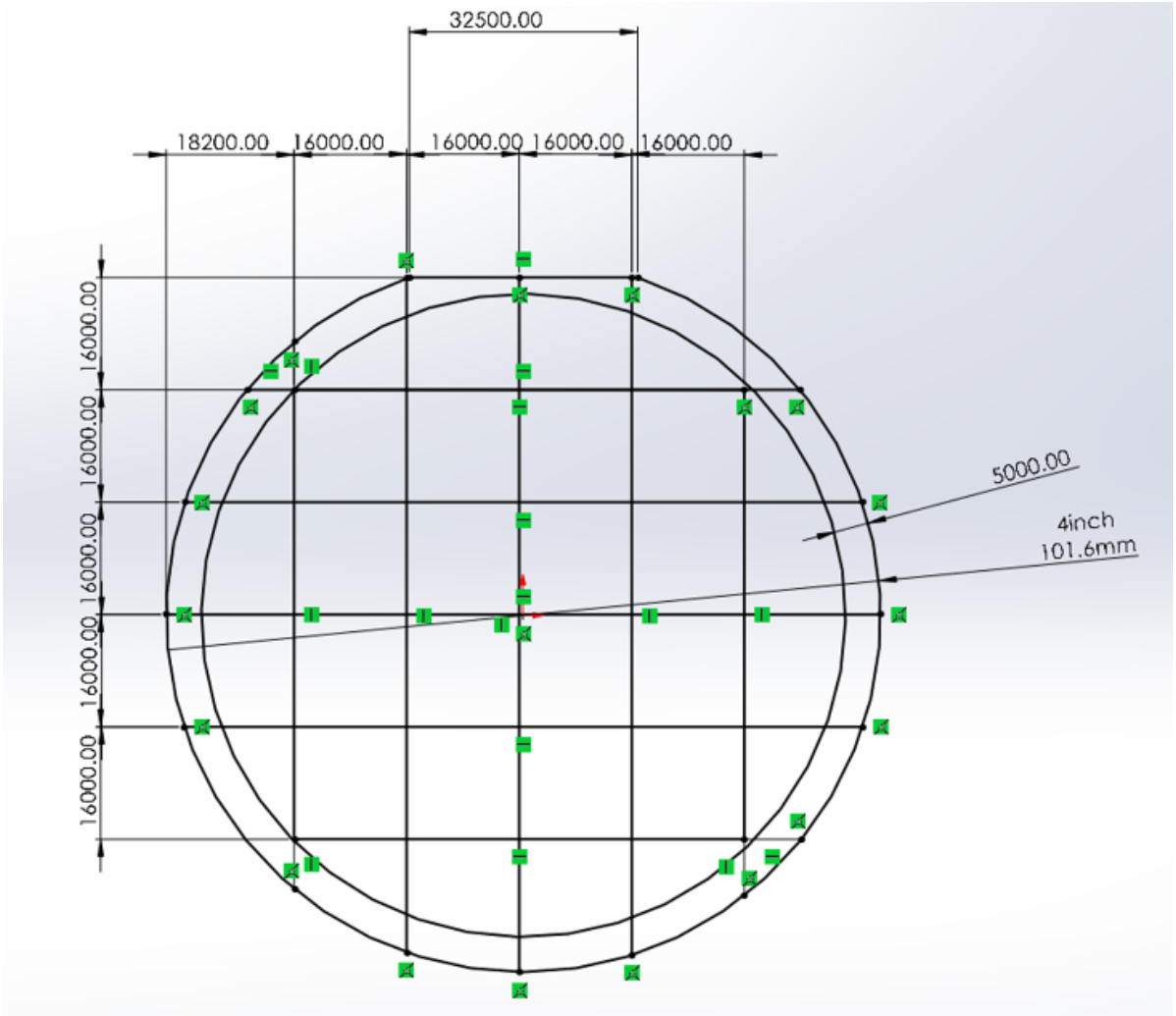

Figure A.3: Dicing map for 16x16 samples

A.1.4. Masks

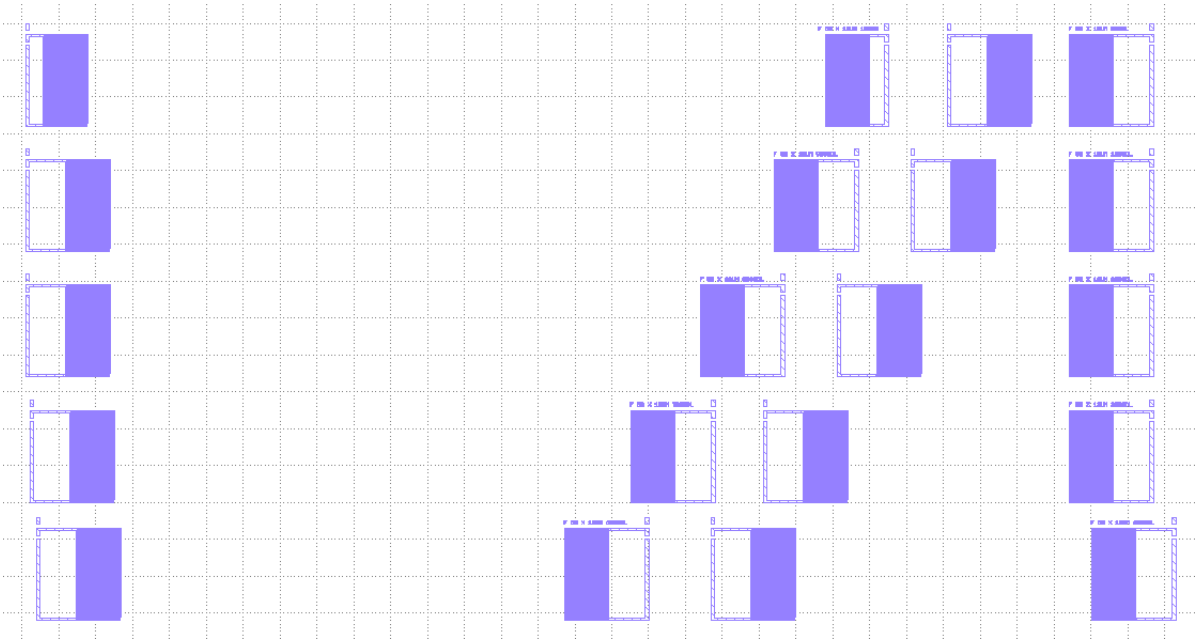

Figure A.4: Mask for delay line design

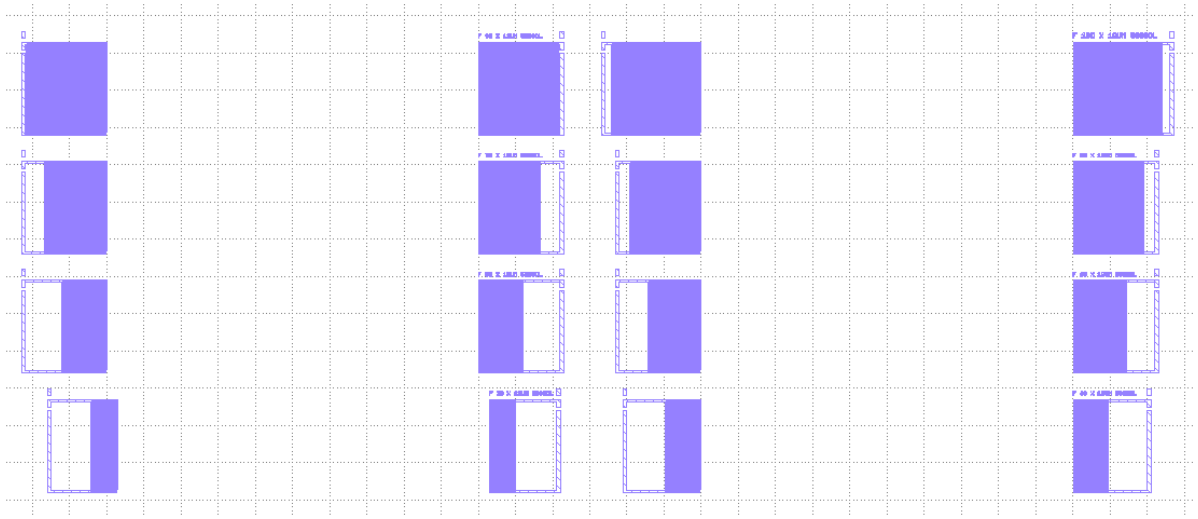

Figure A.5: Mask for IDT pairs design

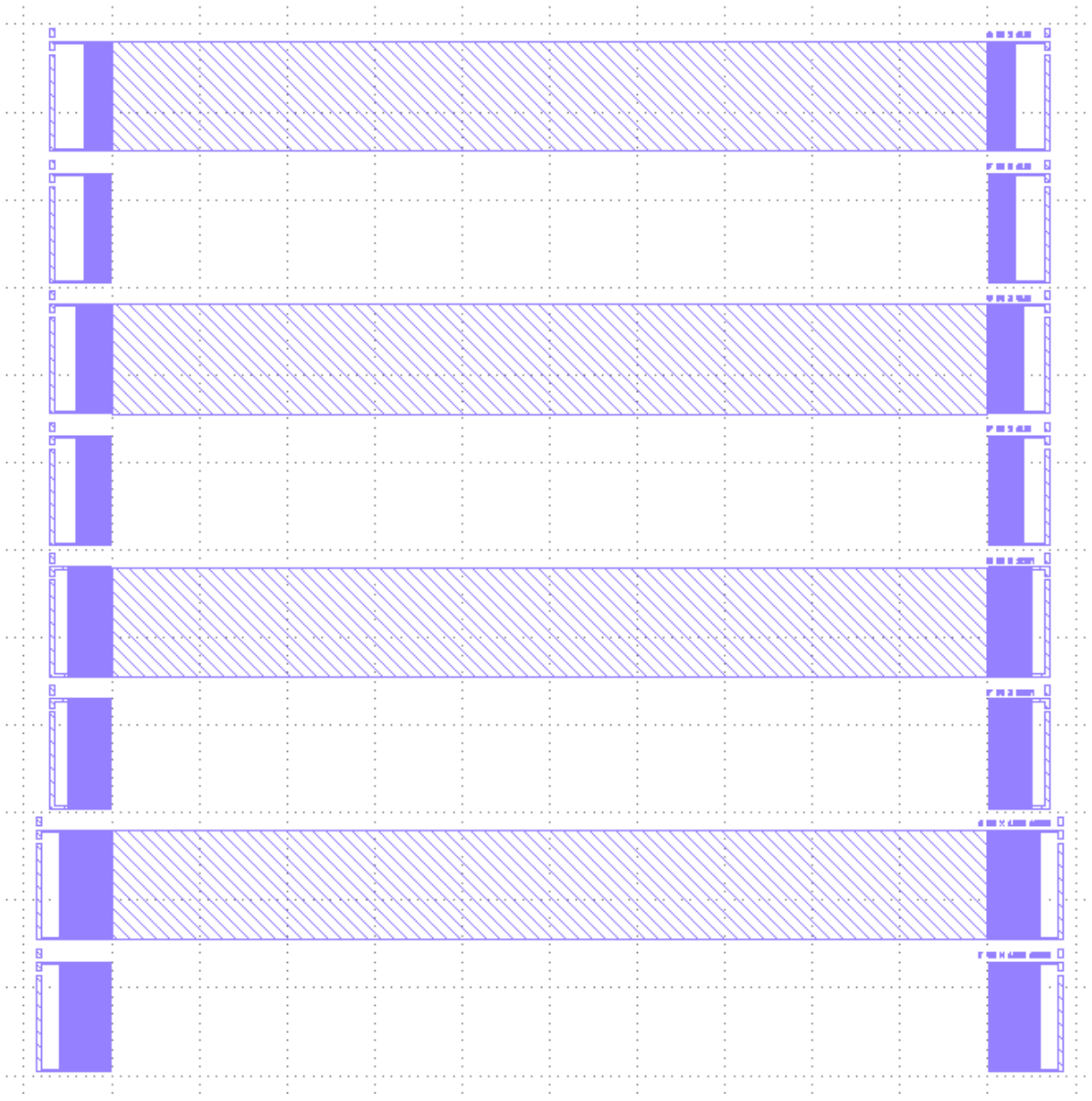

Figure A.6: Mask for wavelength design (6-12μm)

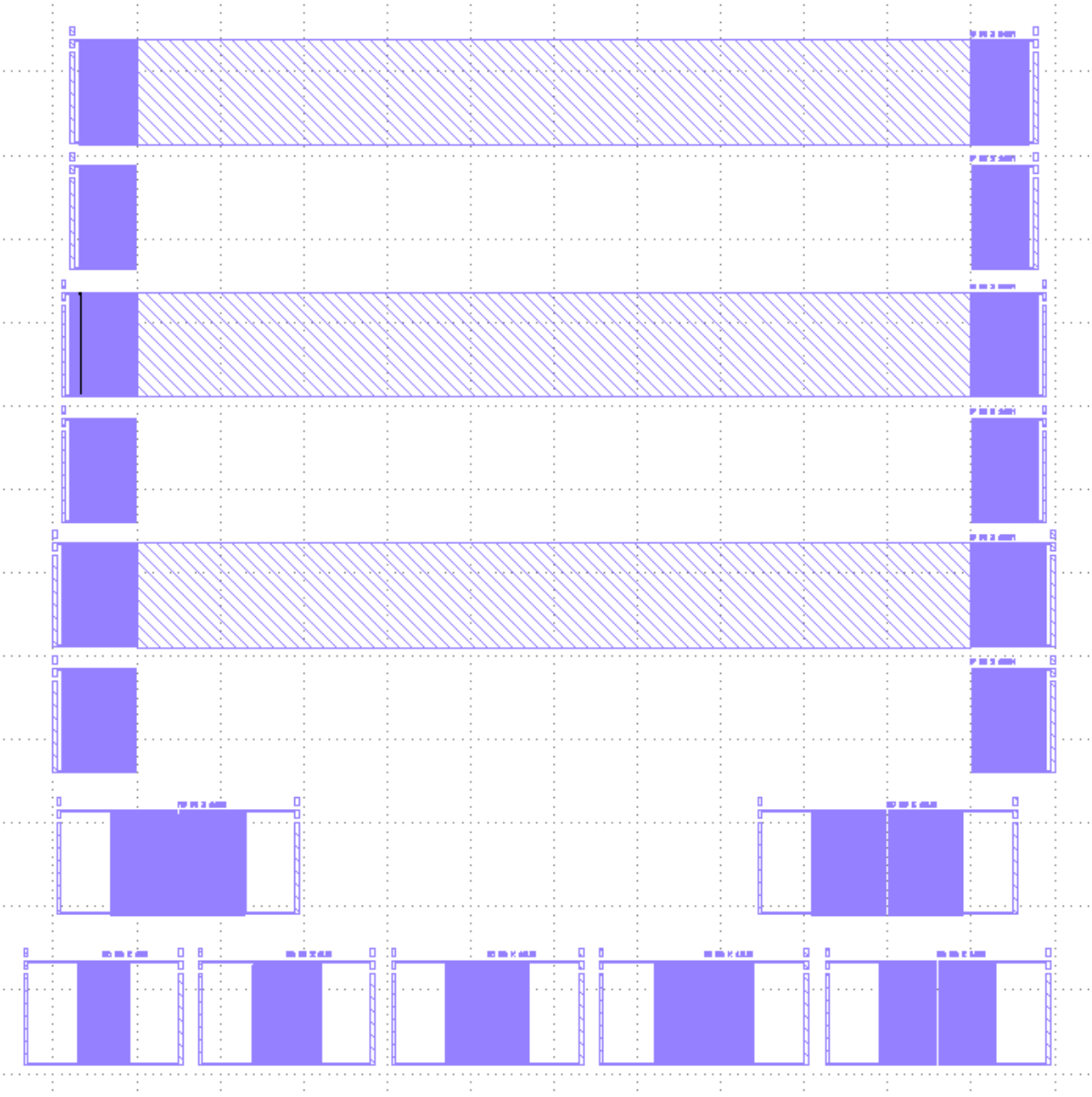

Figure A.7: Mask for wavelength design (14-18μm)

A.2. Measurement

A.2.1. Varying the number of IDT pairs

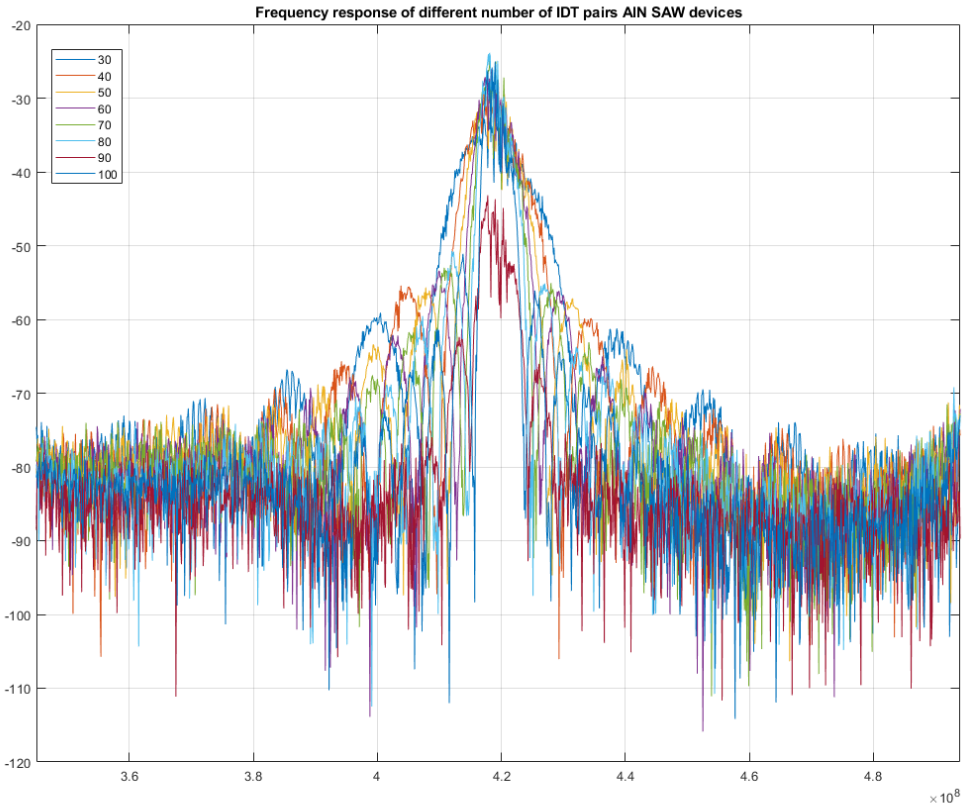

Figure A.8: Measurement results of different numbers of IDT pairs AlN SAW devices

A.2.2. Varying the Delay line length

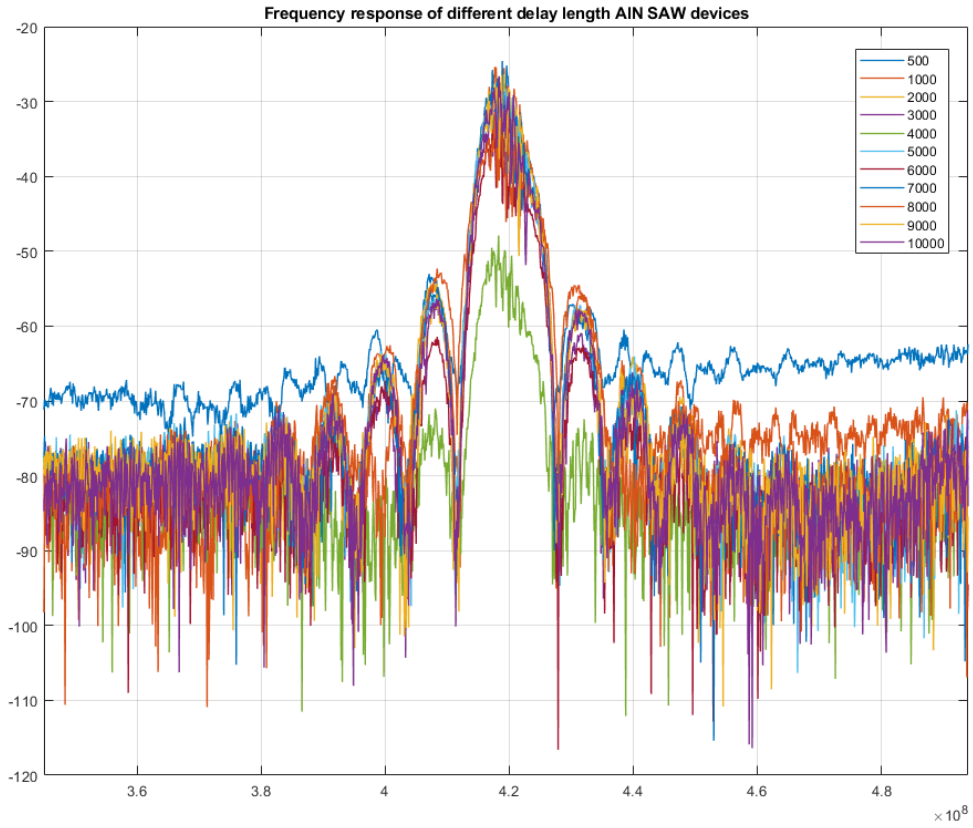

Figure A.9: Measurement results of different delay line length AlN SAW devices

A.2.3. Wavelength design results

AlN

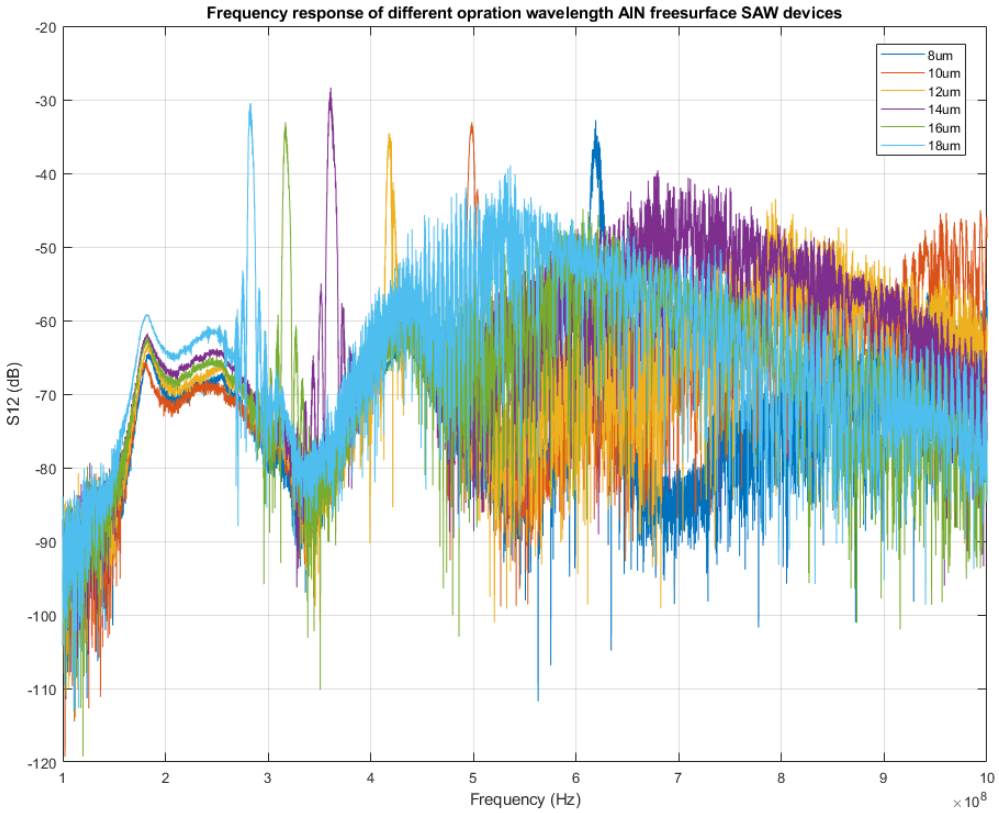

Figure A.10: All AlN free surface SAW devices measurement results

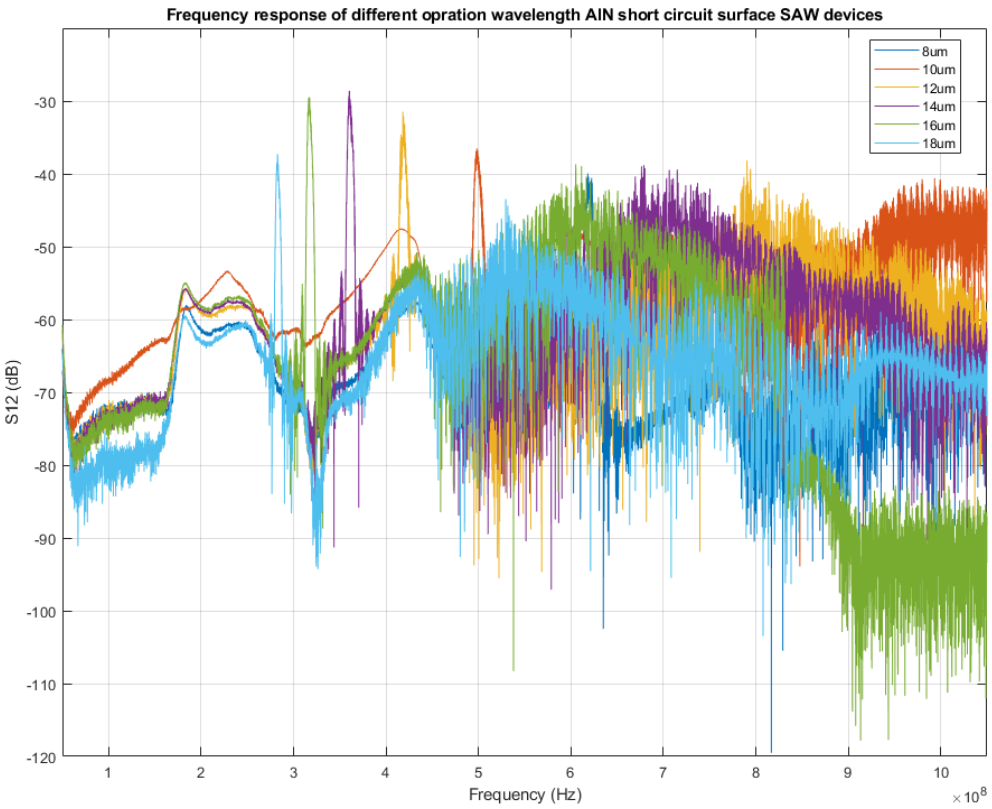

Figure A.11: All AlN short circuit surface SAW devices measurement results

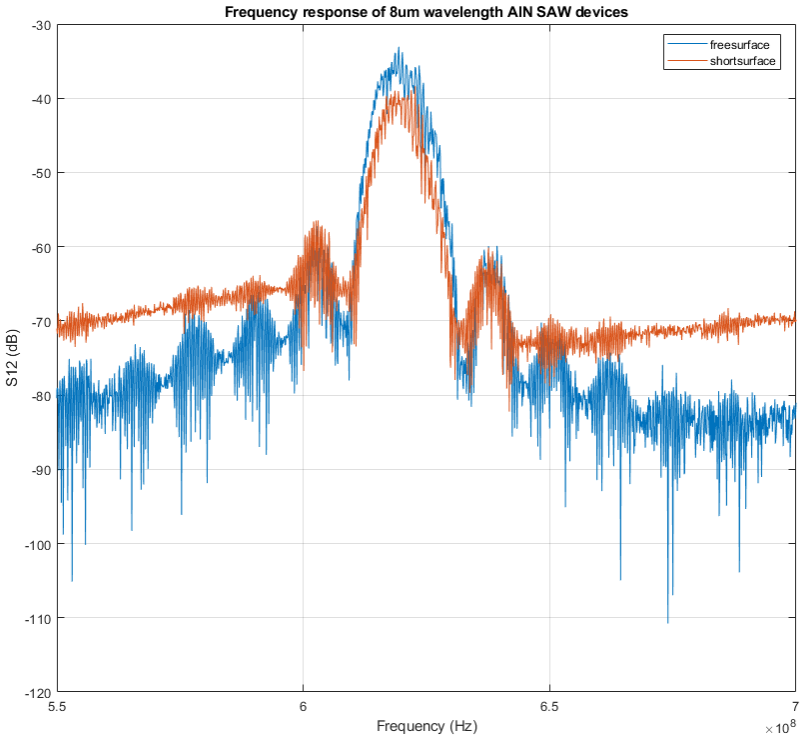

Figure A.12: AlN 8μm SAW devices measurement results

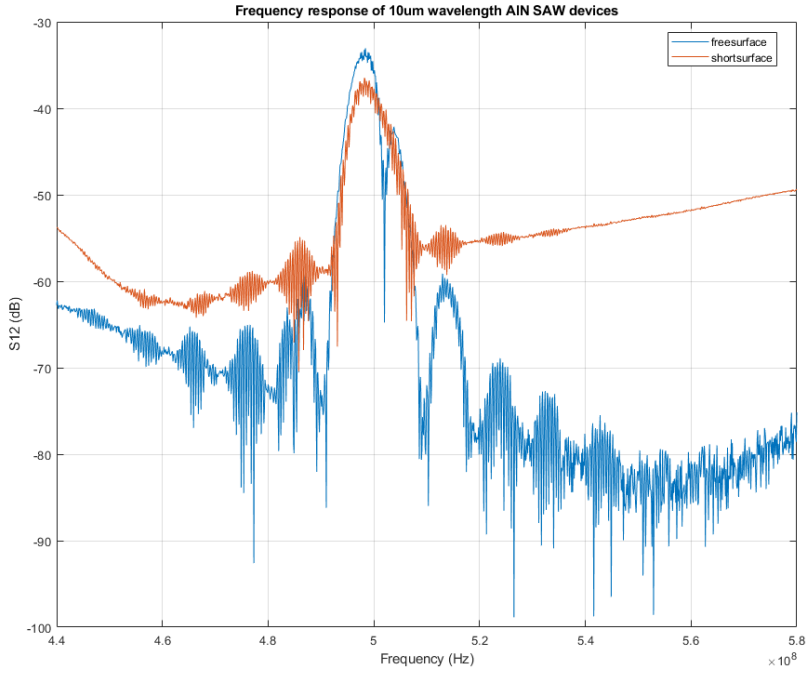

Figure A.13: AlN 10μm SAW devices measurement results

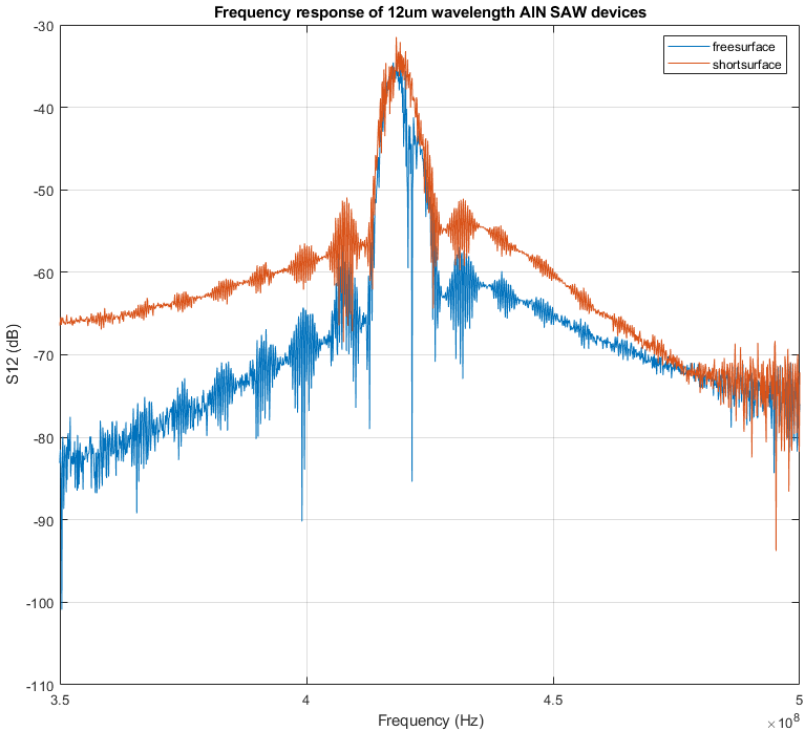

Figure A.14: AlN 12μm SAW devices measurement results

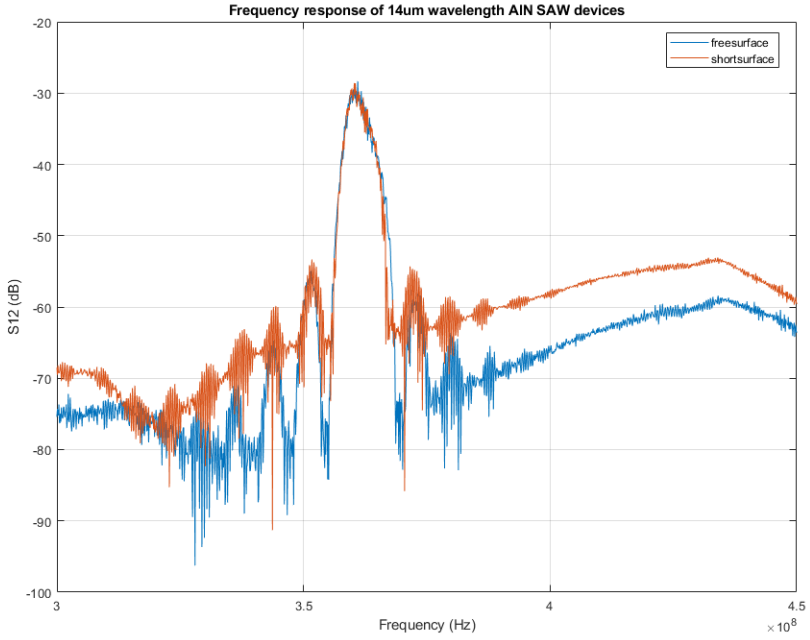

Figure A.15: AlN 14μm SAW devices measurement results

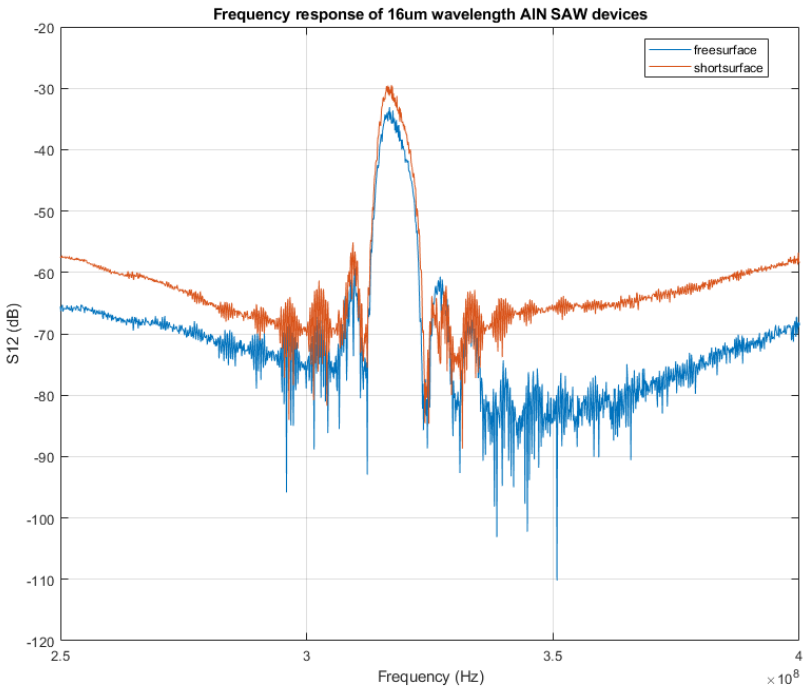

Figure A.16: AlN 16μm SAW devices measurement results

GaN

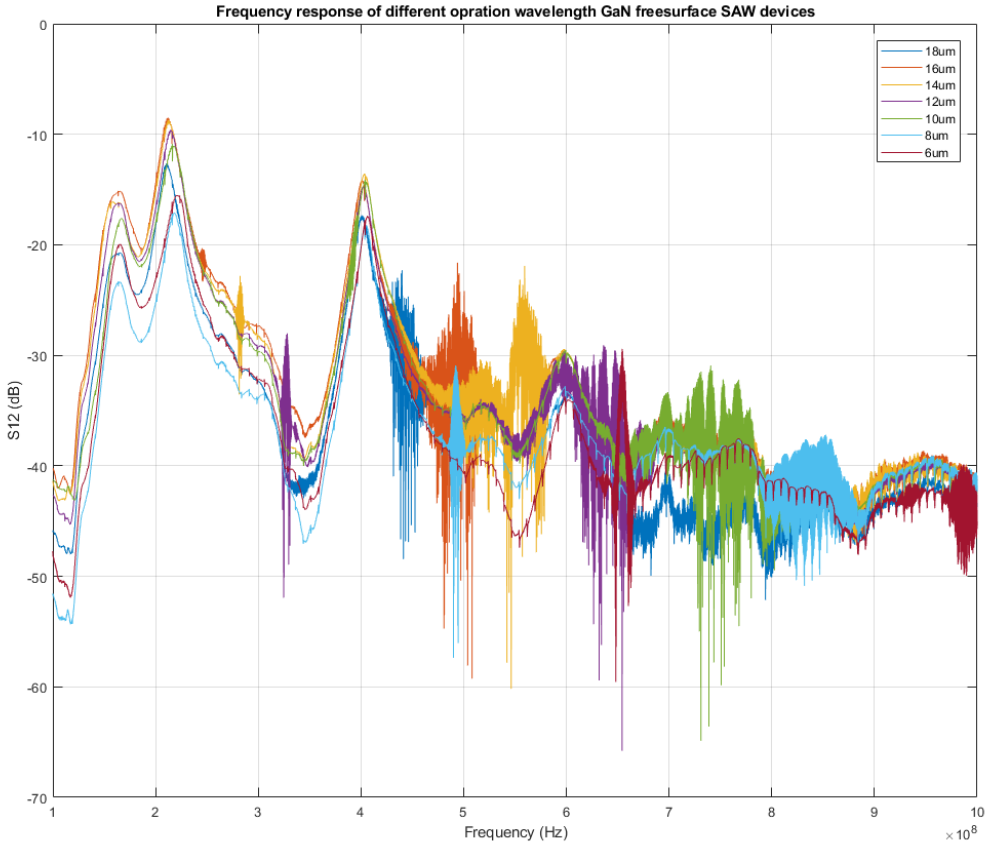

Figure A.17: All GaN free surface SAW devices measurement results

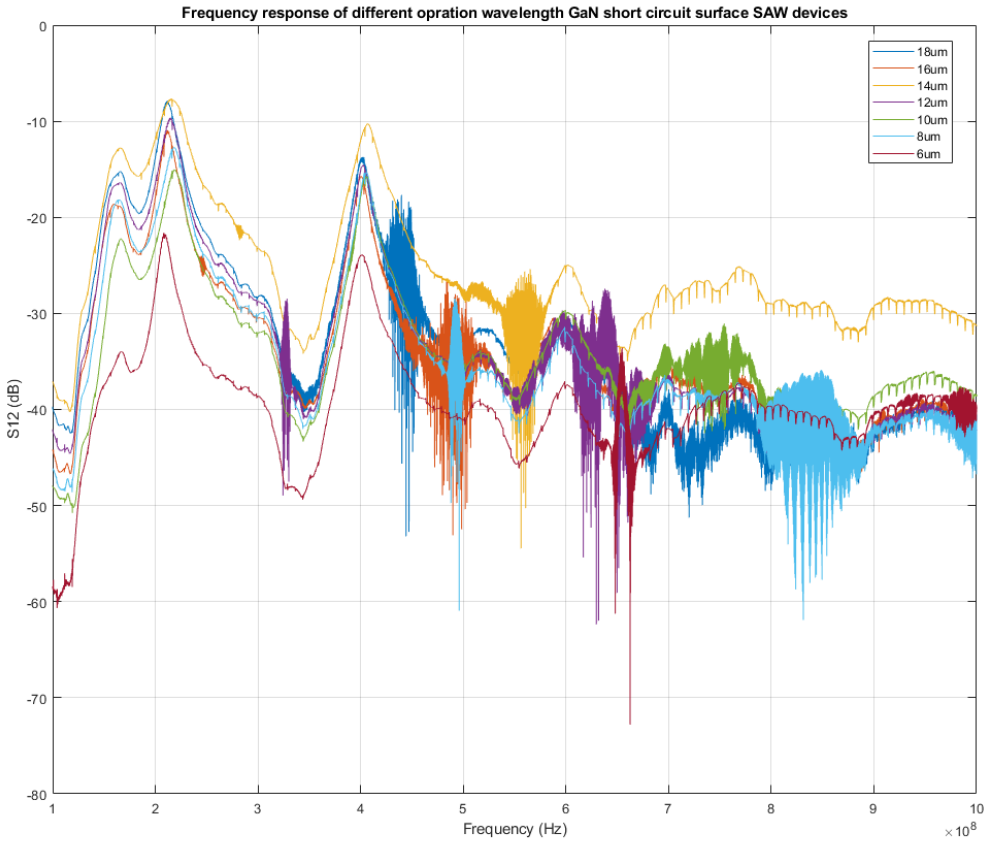

Figure A.18: All GaN short circuit surface SAW devices measurement results

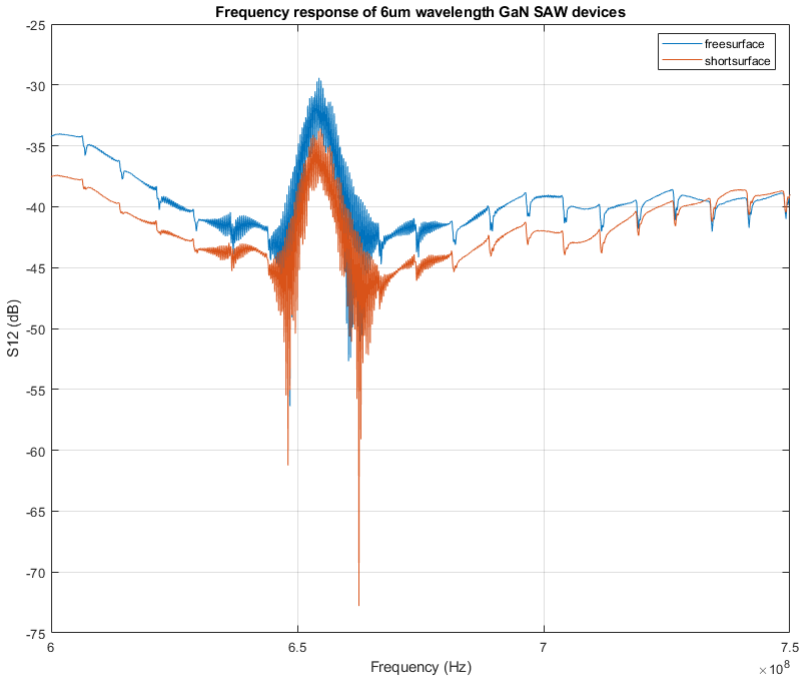

Figure A.19: GaN 6μm SAW devices measurement results

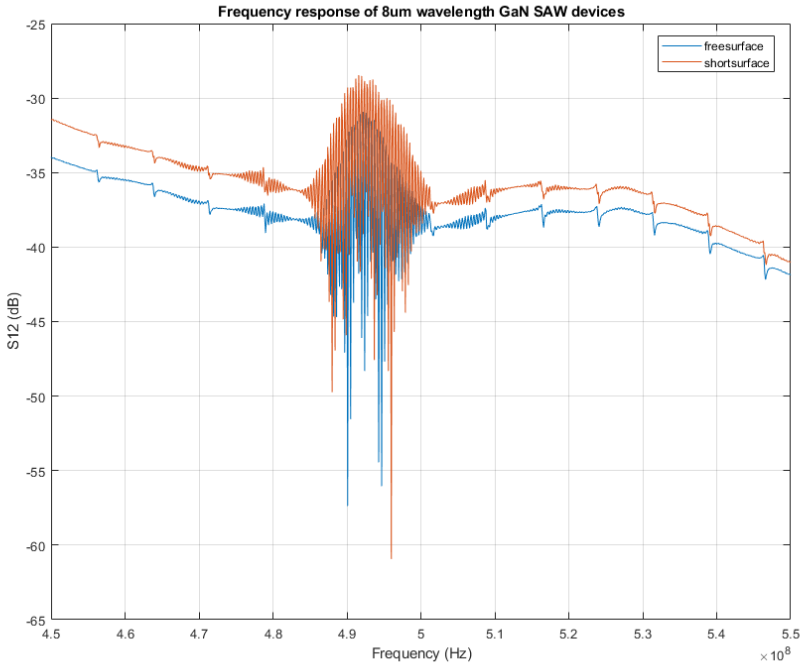

Figure A.20: GaN 8μm SAW devices measurement results

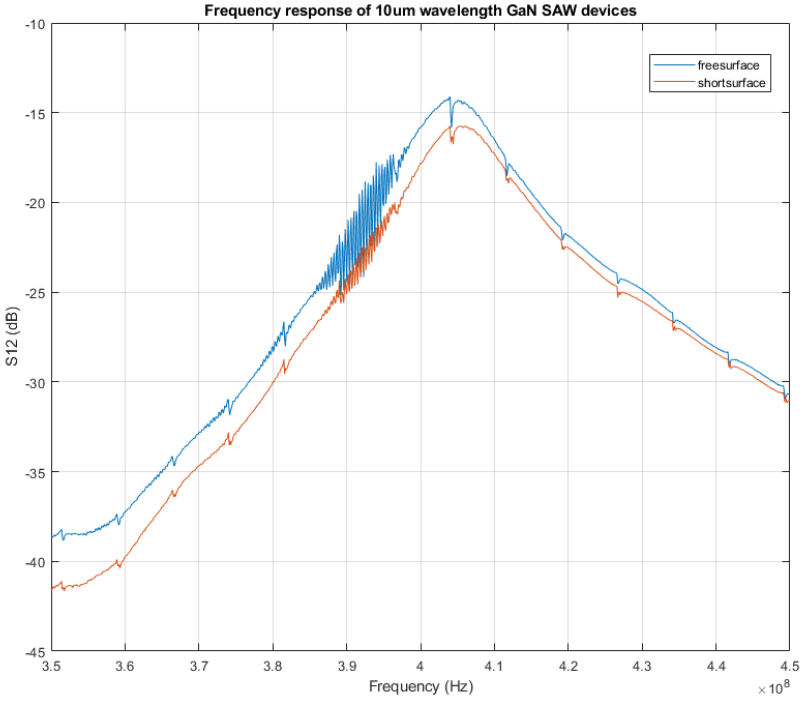

Figure A.21: GaN 10μm SAW devices measurement results

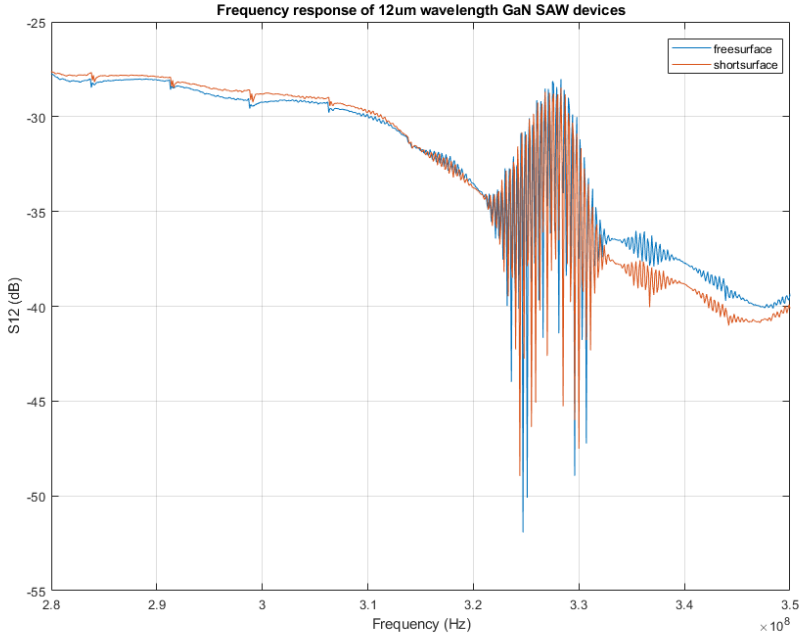

Figure A.22: GaN 12μm SAW devices measurement results

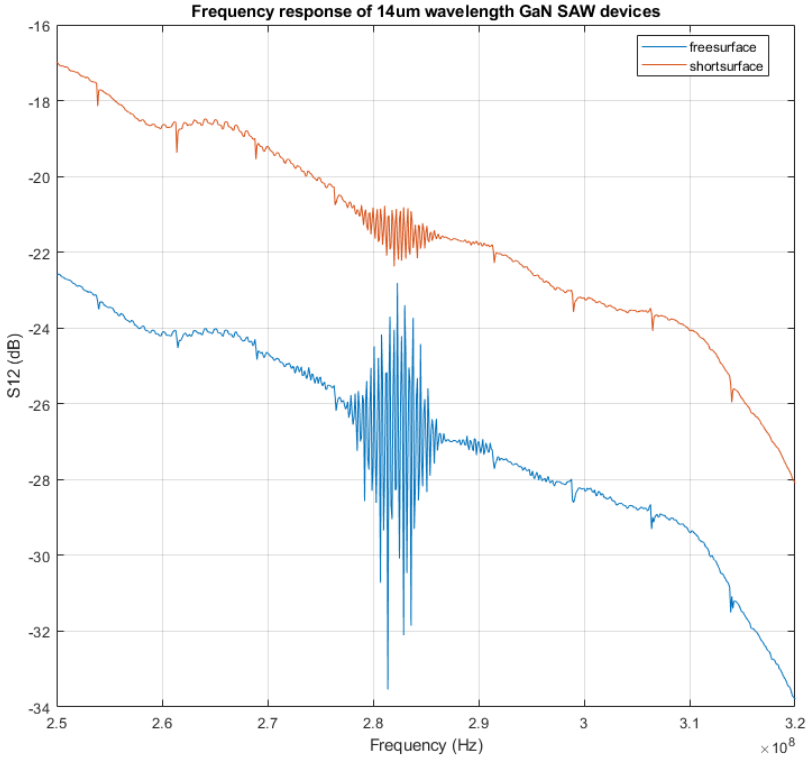

Figure A.23: GaN 14μm SAW devices measurement results

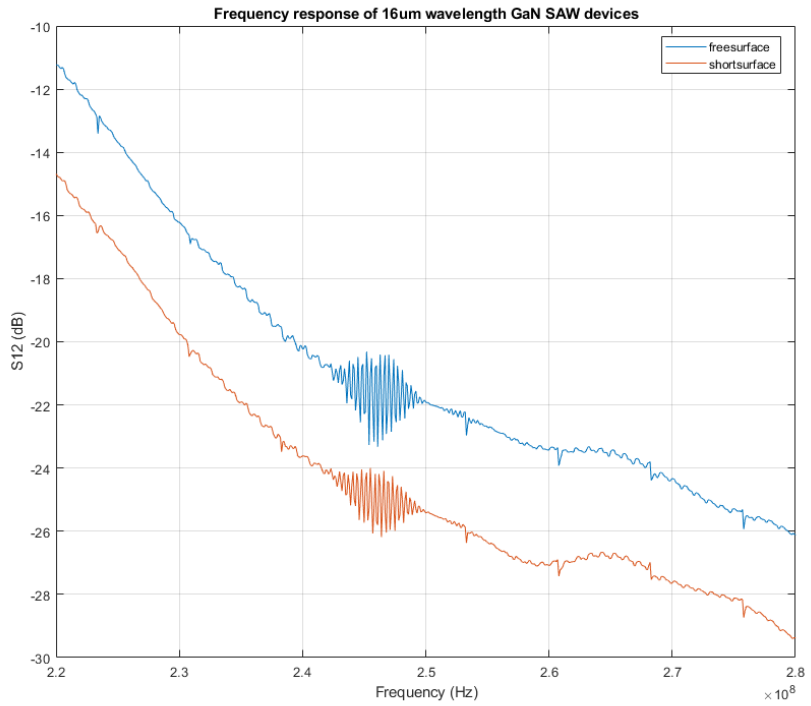

Figure A.24: GaN 16μm SAW devices measurement results

50nm electrodes AlN

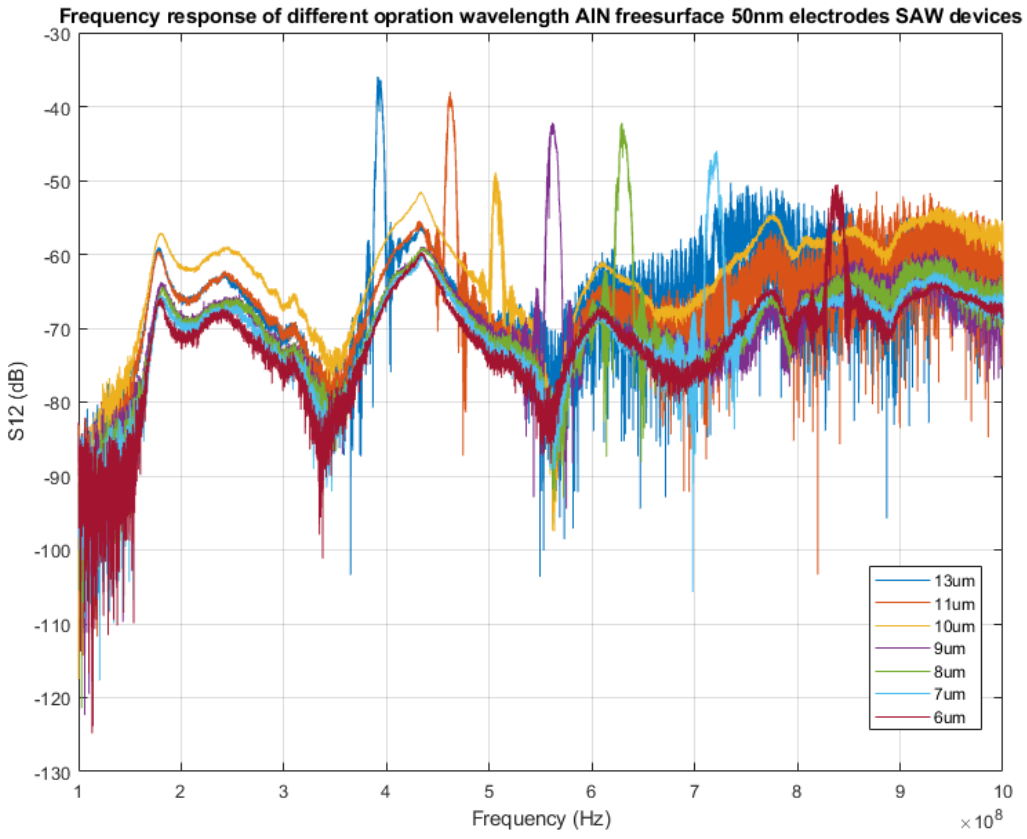

Figure A.25: All AlN free surface SAW devices with 50nm electrodes measurement results

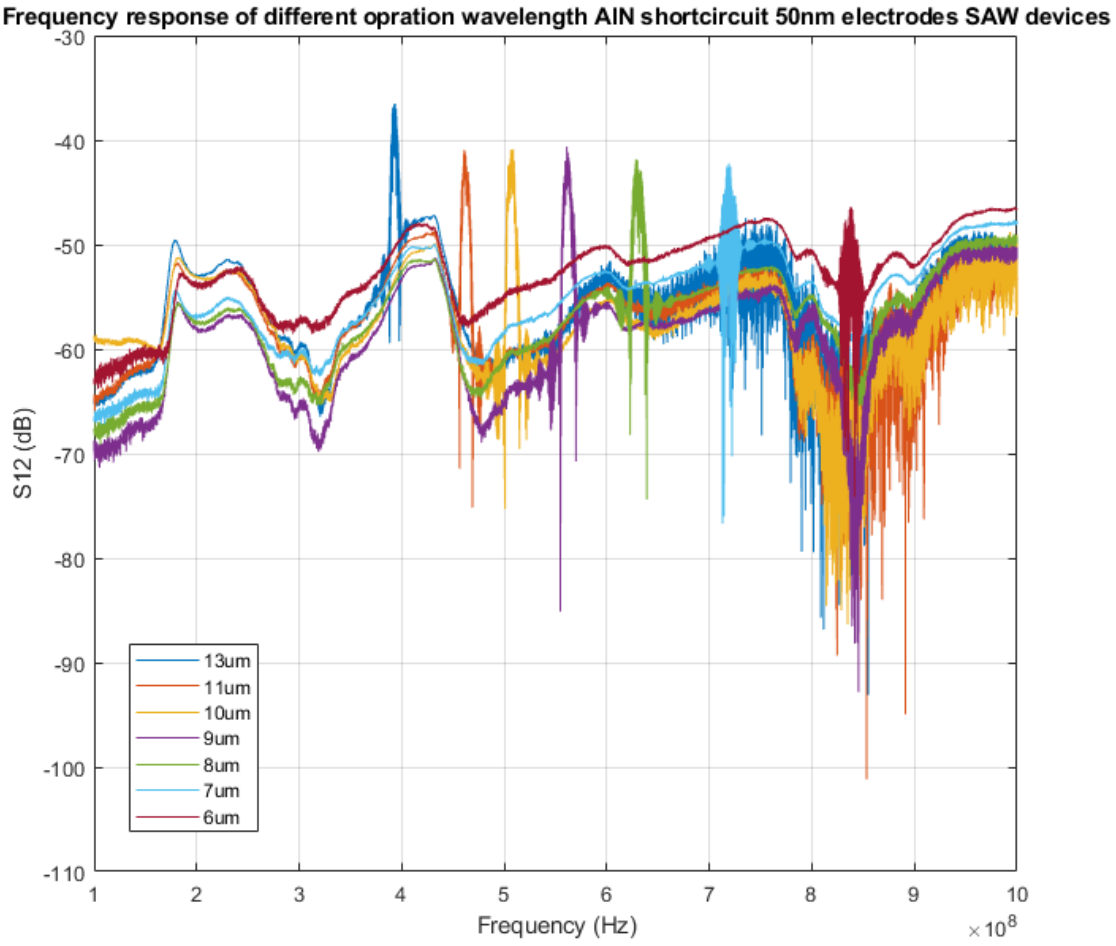

Figure A.26: All AlN short circuit surface SAW devices with 50nm electrodes measurement results